MULTIFRACTAL TECHNIQUES FOR ANALYSIS AND CLASSIFICATION OF EMPHYSEMA IMAGES

A thesis submitted in partial fulfilment of the requirements
for the degree of
Doctor of Philosophy in Computer Science
at the
University of Canterbury
by

Musibau Adekunle Ibrahim

May 2017

This thesis is dedicated to my late father (Mr. Ibrahim Olaitan), my wonderful wife (Mrs. Kemi Ibrahim) and our lovely children(Sam and Jo).

ABSTRACT

This thesis proposes, develops and evaluates different multifractal methods for detection, segmentation and classification of medical images. This is achieved by studying the structures of the image and extracting the statistical self-similarity measures characterized by the Holder exponent, and using them to develop texture features for segmentation and classification. The theoretical framework for fulfilling these goals is based on the efficient computation of fractal dimension, which has been explored and extended in this work.

This thesis investigates different ways of computing the fractal dimension of digital images and validates the accuracy of each method with fractal images with predefined fractal dimension. The box counting and the Higuchi methods are used for the estimation of fractal dimensions. A prototype system of the Higuchi fractal dimension of the computed tomography (CT) image is used to identify and detect some of the regions of the image with the presence of emphysema. The box counting method is also used for the development of the multifractal spectrum and applied to detect and identify the emphysema patterns.

We propose a multifractal based approach for the classification of emphysema patterns by calculating the local singularity coefficients of an image using four multifractal intensity measures. One of the primary statistical measures of self-similarity used in the processing of tissue images is the Holder exponent (α-value) that represents the power law, which the intensity distribution satisfies in the local pixel neighbourhoods. The fractal dimension corresponding to each α-value gives a multifractal spectrum f(α) that was used as a feature descriptor for classification. A feature selection technique is introduced and implemented to extract some of the important features that could increase the discriminating capability of the descriptors and generate the maximum classification accuracy of the emphysema patterns.

We propose to further improve the classification accuracy of emphysema CT patterns by combining the features extracted from the alpha-histograms and the multifractal descriptors to generate a new descriptor. The performances of the classifiers are measured by using the error matrix and the area under the receiver operating characteristic curve (AUC). The results at this stage demonstrated the proposed cascaded approach significantly improves the classification accuracy.

Another multifractal based approach using a direct determination approach is investigated to demonstrate how multifractal characteristic parameters could be used for the identification of emphysema patterns in HRCT images. This further analysis reveals the multi-scale structures and characteristic properties of the emphysema images through the generalized dimensions. The results obtained confirm that this approach can also be effectively used for detecting and identifying emphysema patterns in CT images.

Two new descriptors are proposed for accurate classification of emphysema patterns by hybrid concatenation of the local features extracted from the local binary patterns (LBP) and the global features obtained from the multifractal images. The proposed combined feature descriptors of the LBP and f(α) produced a very good performance with an overall classification accuracy of 98%. These performances outperform other state-of-the-art methods for emphysema pattern classification and demonstrate the discriminating power and robustness of the combined features for accurate classification of emphysema CT images. Overall, experimental results have shown that the multifractal could be effectively used for the classifications and detections of emphysema patterns in HRCT images.

ACKNOWLEDGEMENTS

I would like to express my sincere gratitude to my principal supervisor Dr. Ramakrishnan Mukundan for his guidance, encouragements and several helpful suggestions throughout this research work. He introduced me to this interesting research area, I am indeed very grateful. It is my pleasure to also thank my current co-supervisor Dr Richard Green, and Professor Tad Takaoka, my old co-supervisor for their supports during the course of this study.

Special thanks to everyone in the Department of Computer Science and Software Engineering for their supports during the period of this research. The department organized several useful seminars that were very helpful in my research work; and they all supported me when I was going through personal difficulties. In fact, I really acknowledge the efforts of all the staff members for supporting me throughout this course, without them, this thesis would not have been completed.

I am also grateful to Tieta for her great programming assistance when I was having problems with my thesis, and other colleagues in the department, and in Computer graphics and image processing research group; Alan and Roy for their useful discussions.

This study would not have been completed without the help from the PG office; there were so many helpful seminars organized by the Dean of postgraduate study (Professor Lucy Johnston), particularly the statistics seminars conducted by the consultants (Dr. Elena Moltchanova and Dr. Daniel Gerhard), I am so grateful to you all, you have really played a big part in this thesis.

During the course of this work, I was supported financially by the Tertiary Education Trust Fund scholarship through the Osun State University, Nigeria. I am so grateful to the staff members of this great institution for this help.

I would also like to thank my wife and the children (Kemi, Sam and Jo) and other family members (my mum and my elder brother) for their supports, encouragements and useful advices during this course.

Finally, I would like to thank God almighty for his protection and many prayers he has answered, and the strength that he has provided throughout the projects that I have worked on.

CONTENTS

LIST OF TABLES

LIST OF FIGURES

LIST OF ABBREVIATIONS AND ACRONYMS

ANOVA	Analysis of Variance
ARP	Average Retrieval Precision
ARR	Average Retrieval Rate
AUC	Area Under ROC Curve
AVM	Arteriovenous Malformations
BC	Box Counting
BMEI	Biomedical Engineering and Informatics
BT	Bagged Decision Tree
CAD	Computer Aided Diagnosis
CBIR	Content Based Image Retrieval
CLE	Centrilobular Emphysema
COPD	Chronic Obstructive Pulmonary Diseases
CPU	Central Processing Units
CT	Computed Tomography
DBCM	Differential Box Counting Method
EEG	Electroencephalogram
EER	Equal Error Rates
ERP	Event Related Potentials
fBm	Fractional Brownian motion
FD	Fractal Dimension
FNN	Fuzzy Neural Network
FS	Feature Selection
FSS	Feature Subset Selection
GBRBM	Gaussian Bernoulli Restricted Boltzman Machine
GE	General Electric
GFB	Gaussian Filter Bank
GLCM	Grey-level Co-occurrence Matrices
GLRLM	Grey-level Run Length Matrices
HRCT	High Resolution Computed Tomography
k-NN	*k*-Nearest Neighbour
LBP	Local Binary Patterns

LDA	Linear Discriminant Analysis
LMI	LBP+Multifractal Images
LPCA	Laplacian PCA
MLP	Multi-layer Perceptron
MR	Magnetic Resonance
MSE	Mean Square Error
NB	Naïve Bayes
NN	Neural Network
NP	Nuclear Pleomorphism
NT	Normal Tissue
Open MP	Open Multiprocessors
PCA	Principal Component Analysis
PFT	Pulmonary Function Tests
PSE	Paraseptal Emphysema
RF	Random Forest
RILBP	Rotation Invariant Local Binary Patterns
RILMI	Rotational Invariant LBP+ Multifractal Images
ROC	Receiver Operating Characteristics
ROI	Region of Interest
SFS	Sequential Forward Selection
SVM	Support Vector Machine
TF	Tubule Formation
US	Ultrasound

1 INTRODUCTION

This thesis aims to provide novel contributions to the field of biomedical image analysis by introducing multifractal based techniques for classifying emphysema patterns in High Resolution Computed Tomography (HRCT) images. This chapter provides the main motivations for research in this field, and outlines the goals and contributions of the thesis. It also gives a brief description of the organization of contents.

1.1 Thesis Overview

Multifractal analyses of images have recently found several applications in the field of biomedical image processing. This is because multifractal features could be employed as efficient texture features for the analysis, segmentation and classification of images. Some applications of the multifractal approach are the detection of micro-calcifications in mammograms, tissue classification, nodule detection in lung CT images and identification of regions of interest in MRI images. More information about these and other application areas are given later in the literature review section in Chapter 4. Multifractal analysis allows an image to be decomposed into a mutually disjoint set of images where the intensity distribution in each image follows nearly the same power law according to a chosen measure. This type of fractal decomposition gives us a range of values of fractal parameters such as the fractal dimension and the Holder exponent (Figure 1.1). These parameters are then selected as texture features for the classification task.

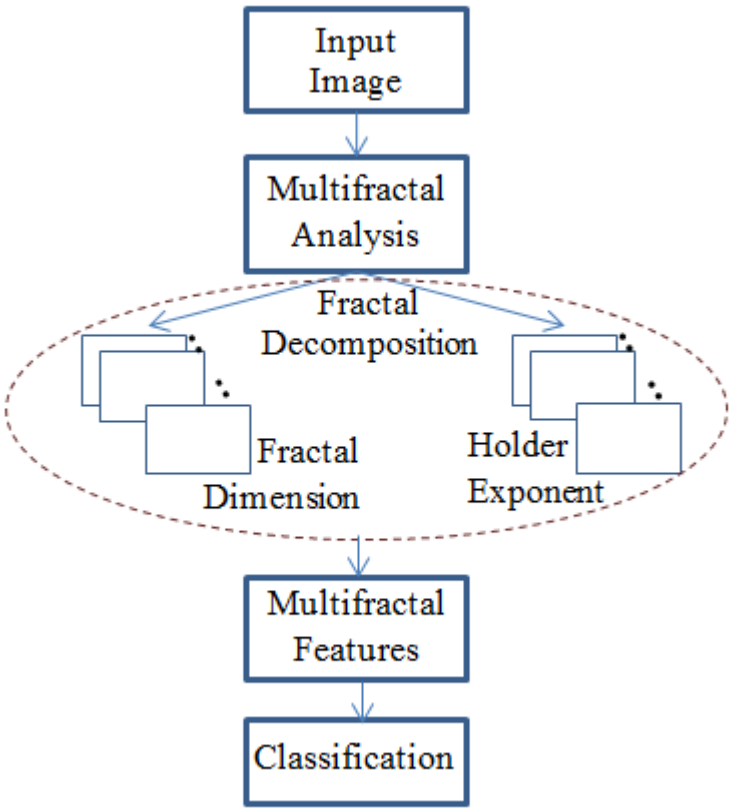

Figure 1-1: General overview of multifractal analysis.

The Holder exponents (or singularity exponents) represent the level of irregularities in the intensity values. The fractal dimension, on the other hand, measures the self-similar characteristics in the distribution and the amount of space filled by pixels with the same Holder exponent. These parameters measured across the images in the fractal decomposition can be used to build important feature sets called multifractal spectrum and the α-histogram. The mathematical and computational aspects of these feature sets are described in detail in Chapter 3. This thesis investigates the feature characteristics of these multifractal parameters in the analysis and classification of emphysema patters in HRCT images. Several types and combinations of fractal features have been studied in detail, and extensive experimental analysis carried out to analyze their effectiveness in algorithms for identifying regions of interest and classification. Novel algorithms for automatically classifying emphysema disease patterns have been proposed and their performance evaluated using images from an online emphysema image database.

.

1.2 Research Goals

The goal of this work is to perform a thorough study of theoretical aspects of fractal and multifractal analysis that could be applied in biomedical applications, specifically for classifying emphysema patterns in HRCT images. This study aims at identifying the features, computational tools and methods that are useful in the classification task.

Several methods of fractals and multifractals in the analysis of medical images have been suggested and evaluated in different ways. One of the most popular methods that have been used by many researchers in the past is the box counting method. In this project, we propose to develop a new method that would address the limitations of the existing methods in terms of efficiency, speed of image analysis and error corrections. The study also aims at improving the performance of earlier multifractal feature based approaches in terms of accuracy and computational time and develop novel methods by adopting proper feature selection methods and by combining features derived from the multifractal spectrum with other types of features such as the α-histograms and local binary patterns.

1.2.1 Research Questions

Some of the important research questions that are addressed in this thesis include the following:

- Can multifractal features be effectively used to identify the emphysema patterns in CT images? How do these feature perform in terms of intra-class similarity and inter-class variance?
- Can we combine the values of multifractal spectrum with the α-histogram to obtain a more robust feature set? How should the feature selection be performed?
- What are the main implementation aspects to be considered?
- How do the results vary with the changes in intensity measures?
- How do multifractal techniques compared with other types of feature descriptors?
- Can multifractal descriptors be combined with local binary patterns in the classification algorithm?
- What are the limitations of the multifractal approach?

1.3 Motivations

Many algorithms using multifractal features have been proposed in the literature in the field of biomedical image analysis, such as brain tissue classification, detection of micro-calcifications, edge detection and segmentation, and identification of regions of interest in MRI images. However, multifractal features have not been previously applied to the classification of emphysema disease patterns in HRCT images of the lung. This has been the primary motivation for our research work, and the thesis explores the possibility of using multifractal analysis in emphysema classification and proposes several novel classification algorithms in this field. Overall, the summary of the motivation of this thesis includes the following points:

- The intensity distribution of lung tissue images is highly irregular. We can classify pixels in such images using the statistical self-similarity measures evaluated using intensity variations in pixel neighbourhoods. We could therefore use multifractal methods as powerful tools in characterizing important features present in the images.
- Significant research work has already been done in emphysema classification in lung tissue images using local texture features, but not using multifractal descriptors.
- Multifractal methods offer different types of descriptors using variations in intensity measures.
- Different types of multifractal features can be combined to form efficient texture descriptors for classifying emphysema patterns.

1.4 Publications

The proposed multifractal based approach for the classification of emphysema patterns by calculating the local singularity coefficients using different intensity measures has been presented in detail in Chapter 4. The research confirms that multifractal spectrum could be effectively used for the classification of histo-pathological cases. The results were published at the 2014 International Conference on Future Bioengineering (ICFB).

Ibrahim, M., Mukundan, R., **Multifractal Techniques for Emphysema Classification in Lung Tissue Images**. In Proc. of the 3rd Intnl. Conf. on Future Bioengineering (ICFB-2014), pp. 115-119.

The following paper was presented at the New Zealand Computer Science Students Conference (NZCSRSC) in Auckland.

Ibrahim, M., Mukundan, R., **On Feature Selection Methods for Accurate Classification of Emphysema Images.** Oral presentation, New Zealand Computer Science Research Students Conference (NZCSRSC), University of Auckland, Auckland, 10th April, 2015.

This paper applied feature selection (FS) techniques for improving the classification accuracy of the emphysema CT images by selecting the important features that would greatly improve the prediction accuracy. Different classifiers were tested with the algorithms to evaluate the performance and for comparison purposes. The following Journal article was published at the Artificial Intelligence research journal:

Ibrahim, M., Mukundan, R., **Cascaded Techniques for Improving Emphysema Classification in CT Images**. Artificial Intelligence Research (CANADA, 2015), AIR vol. 4, no. 2, pp. 112-118, 2015.doi:10.5430/air.v4n2p112, http://www.sciedupress.com/journal/index.php/air/article/view/7052.

This journal article combined two descriptors; the alpha-histogram and multifractal descriptors for efficient classification of CT images. This research applied cascaded techniques to join the features obtained from both descriptors and the combined descriptor significantly increased the classification accuracy.

In the following publication, two descriptors were proposed to extract the textural structures of the emphysema CT images. The local binary patterns (LBP) and the rotational invariant LBP features are combined with the multifractal images to produce two descriptors. The newly generated descriptors demonstrate the discriminating power and robustness of the combined features for accurate classification of emphysema CT images. This research was published at BMEI in 2015.

Ibrahim, M., Mukundan, R., **Analysis of Scale Variations of Local Features for Accurate Classification of emphysema Images**. In Proc. of 8th Intnl. Congress on Biomedical Engineering and Informatics (BMEI, Shenyang, China, 2015). http://ieeexplore.ieee.org/xpl/mostRecentIssue.jsp?punumber=7394813.

The recent publication describes the application of Higuchi fractal dimension for identifying the regions or locations of the emphysema patterns. The paper uses some statistical techniques with the Higuchi fractal parameters for

efficient classifications of different lung tissue layers. This research was presented at the first African Conference on Biomedical Engineering and Sciences (AFROBIOMEDIC, 2016), Nicon Luxury Hotel, Abuja, Nigeria. The details of the conference paper presented are as follows:

Ibrahim M., Mukundan R., **Local Descriptors in CT Images for Efficient Pattern Classification.** Oral presentation, African Conference on Medical Physics, Biomedical Engineering and Sciences (AFROBIOMEDIC, Abuja, Nigeria, 2016).

1.5 Thesis Organization

The remaining part of this thesis is organized as follows: Chapter 2 provides an outline of the important concepts in fractal theory and their applications in the analysis of biomedical images. Specifically, the computational aspects of different types of fractal dimension are discussed in detail. Chapter 3 introduces multifractal measures and their applications in the computation of multifractal features. Different types of multifractal spectra are discussed in this chapter. Chapter 4 provides extensive literature review on multifractal methods, particularly in the field of biomedical image analysis, focussing on two major application areas, namely, classification and segmentation.

Chapter 5 discusses different methods of calculating fractal dimension and demonstrates how this important parameter could be used to identify the region of interest (ROI) in images. An original contribution was made in this chapter by implementing the Higuchi's dimension for the computation of fractal dimension in emphysema images. This tool was used to access the regions that contain the presence of emphysema, the class of the emphysema and the quantity of the emphysema present. In this chapter, other multifractal based techniques are implemented by generalizing Chhabra's approach, such that the generalized dimensions or Renyi spectrum of the emphysema images are generated for the detection and classification of emphysema patterns. In addition, the alpha and f(alpha) images are calculated using the Holder exponent, and applied for the classifications of the images.

This chapter describes the multifractal analysis of the emphysema images and how it was used for the classification of emphysema CT images by calculating the Holder exponent, and the multifractal spectrum of the digital images. An original contribution

was made in this chapter as the findings confirmed that multifractal is a very powerful descriptor for the classification of histo-pathological cases. However, the results require some improvements, some of the important implementation aspects of a multifractal based technique that could be used to improve the classification accuracy are also discussed in this chapter.

The details on the feature selection (FS) techniques for accurate classification of emphysema images are considered in Chapter 6. Part of the contribution made in this chapter is the application of a FS method for selecting the best features that would reduce the model complexity and thus increased the computational speed of the classification process.

Chapter 7 outlines the algorithms for the development of the alpha-histogram of the CT images, and the features obtained are jointly combined with the multifractal features in the form of hybrid concatenation for effective classification of images. The classification results in the form of confusion matrices are cascaded to further increase the classification accuracy. The results obtained in this chapter were published in an artificial research journal.

Other textural classification methods are proposed in Chapter 8 by implementing the local binary patterns (LBP) of the emphysema CT images. Efficient features are extracted from the LBP and the rotational invariant LBP features. Two new descriptors are generated by combining the local features from the LBP with the global features obtained from the multifractal images. The performances of the combined features are evaluated with different classifiers; in this case, the support vector machine (SVM) and the random forest (RF) are employed in the classification process. The experimental results show that the descriptors significantly improved the classification accuracy and outperformed earlier approaches, including the-state-of-the-art methods for emphysema image classification. Finally, limitations and conclusions of our findings are discussed in chapter 9, and the outlines of future research directions.

2 FRACTALS

The research work reported in this thesis uses several fundamental concepts in fractal theory. While fractals are commonly associated with self-similar objects, in image analysis applications, fractal measures represent certain types of irregularities in structures. The most fundamental measure that characterizes the scaling behaviour of a fractal structure is the fractal dimension. Several types of fractal dimensions and their computational aspects are discussed in this chapter.

2.1 Introduction

The notion of fractals is closely tied to several important geometrical concepts such as self-similarity, symmetry, periodicity and scale invariance. Some of the shapes that are commonly used as examples of fractals are the Koch curve, the Sierpinski triangle, the dragon curve and the Barnsley fern (Figure 2-1).The structural similarity at various levels of detail (or "scales") can be clearly observed in all the above shapes. Indeed, these shapes are generated using this very property. Given a shape at the base level, multiple copies are created, transformed and positioned according to a well-defined procedure to get the shape at the next level. The iterative process is repeated a number of times to get fractal shapes with the required level of complexity.

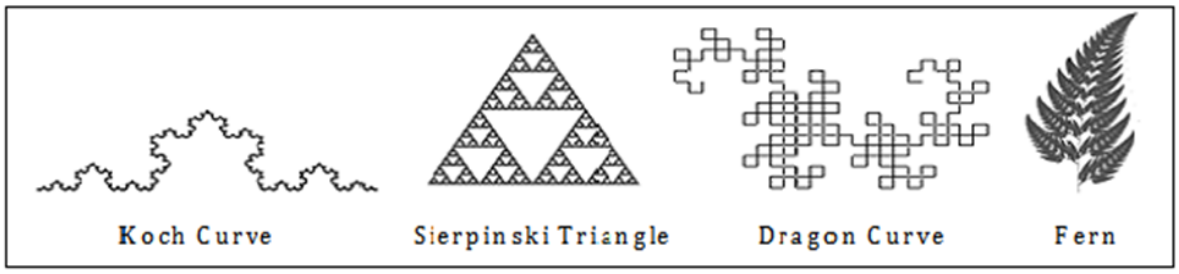

Figure 2-1: A few basic fractal shapes.

Two such iterative procedures are Lindermayer system (L-system) and the iterated function system (IFS). The first three fractals in Figure 2-1 was generated using L-systems, while the Fern was generated using an IFS. The L-system uses a grammar based string production rule that generates a fractal as a string of turtle commands. The IFS on the other hand uses a set of affine transformations to repeatedly transform a point. The collection of all points thus generated forms a fractal shape.

There are more complex methods for generating fractals. The Mandelbrot set is defined as the orbit of a point at the origin under the iteration of a non-linear map of second degree in the space of complex numbers. When the generating point is switched to the constant value of the quadratic map, we get a group of interesting fractal shapes called Julia sets. Both the Mandelbrot and the Julia sets are highly intricate and infinitely complex shapes (Figure 2-2).

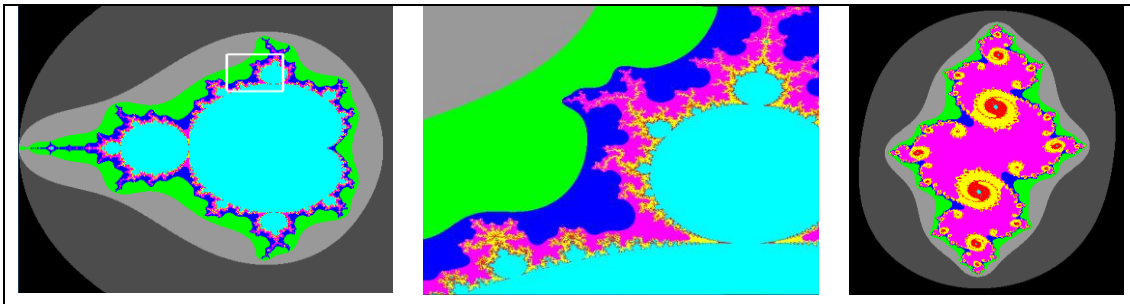

The Mandelbrot set and a zoomed-in segment

The Julia set

Figure 2-2: The Mandelbrot and the Julia sets

Inspired by the structural complexity and the aesthetic features of the Mandelbrot and Julia sets, several other popular fractal shapes were also developed using both complex and hyper-complex systems. These developments also saw the evolution of new areas

such as fractal art side by side the development of fractal theory in mathematics and physics.

All fractals we have seen so far in this section fall into the general category of deterministic fractals. Another important class of fractals is based on stochastic rules or the inclusion of random variations in the iterative systems described above. A classic example of a one-dimensional random fractal is the Brownian motion obtained by integrating Gaussian white noise. Random fractals are used to create models of several real-world objects and natural phenomena in computer graphics. Models of trees, terrains and clouds can be generated using random fractal processes, where the non-uniform appearance is created with the addition of random perturbations. A very well-known technique for generating random fractals is the mid-point displacement method. This method also finds applications in the diamond-square algorithm used for terrain programming.

2.2 Exact and Statistical Self-Similarity

The most important geometrical characteristic exhibited by fractals is self-similarity, which is the property of invariance under certain scale transformations. A fractal on a plane can be viewed as a bounded set S of two-dimensional points. The set $S$is self-similar if it is the union of N non-overlapping subsets, each of which is congruent to scaled versions of S (Mandelbrot, 1977). We say that two sets of points are congruent if by using a similarity transformation consisting of scaling, rotations, transformations and reflections; we can transform one set into an exact copy of the other. The fractals shown in Figure 2-1 have exact self-similarity property. However, all real-world examples modelled using random fractals have statistical self-similarity. Here, different parts of a fractal cannot be made exactly congruent to the whole set even after an arbitrary rotational transformation and displacement. In this context, statistical self-similarity refers to the fact that enlargements of small constituent segments of a fractal have the same statistical distribution as the whole set (Falconer, 2003).In other words, parts of a random fractal can be matched with the whole set only in a statistical sense. In a broader context, statistical self-similarity refers to the characteristic of having a nearly constant measurement (within an allowable threshold) of certain statistical parameters derived from sets at various scales.

2.3 Fractal Dimension

Fractal dimension plays a central role in the theory of fractals and also in almost all applications involving fractals. Fractal dimension has the ability to characterize the irregularity of shapes, which other dimensions such as the topological dimension may not be able to represent. The fractal dimension is used to estimate the size and roughness of fractal sets; it is a number associated with a fractal that tells how densely the fractal occupies the underlying space.

The computational methods used for the estimation of fractal dimension in this thesis are the box counting and the Higuchi methods. These and related methods are outlined in the following sections.

2.3.1 Euclidean and Topological Dimensions

One of the most commonly used dimensions is the Euclidean dimension D_E that considers the space occupied by an object. In this measurement, a structure is called one-dimensional if it is embedded on a straight line, two-dimensional if it is embedded on a plane and three-dimensional if it is embedded in space. A point has dimension 0. The topological dimension D_T of an object corresponds to the number of independent variables (or parameters) needed to describe it. Thus, a point is 0-dimensional, a curve is 1-dimensional, and spherical surfaces and planes have a topological dimension 2. The Euclidean and topological dimensions both assume only integer values.

2.3.2 Hausdorff Dimension

The notion of a fractal dimension is entirely based on the theory of Hausdoff dimension (also known as Hausdorff-Besicovitch dimension). Consider a curve C on a two-dimensional plane, which is covered using a set of discs D_j or radius r_j (j = 1..n) as shown in Figure 2-3. We impose the condition that $r_j \leq \delta$ for some $\delta > 0$, for all j. Such a set of discs is called a δ-cover of C.

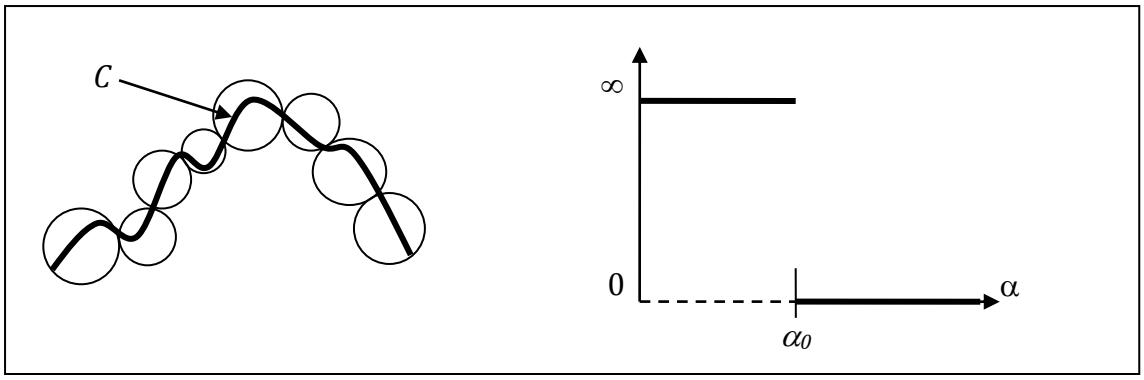

Figure 2-3: A δ-cover of a curve C, and a depiction of the Hausdorff dimension

The Hausdorff measure $H_\alpha(C)$ on the curve C is defined in terms of its δ-cover and a parameter (exponent) α as

$$H_\alpha(C) = \lim_{\delta \to 0} \left\{ \inf \left(\sum_j r_j^\alpha \right) \right\} \qquad (2\text{-}1)$$

The Hausdorff measure has the property that there exists a critical value α_0 such that

$H_\alpha(C) = \infty$, if $\alpha < \alpha_0$

$H_\alpha(C) = 0$, if $\alpha > \alpha_0$ (2-2)

The value of α_0 is called the Hausdorff dimension of the curve C.

Figure 2-3 shows the variation of $H_\alpha(C)$ as given in the above equation.

2.3.3 Box Counting Dimension

Box counting is the most widely used fractal dimension in computing applications. It became a highly popular technique because it can be very easily implemented. Box dimension is also sometimes referred to as the capacity dimension. The definition is based on the concepts relating to δ-cover presented in the previous section (2.3.2). For computing the box dimension, we subdivide a rectangular region containing a fractal curve into sub-regions (or "boxes") of size δ. The δ-cover is then given by the number of boxes that intersects or contains the fractal.

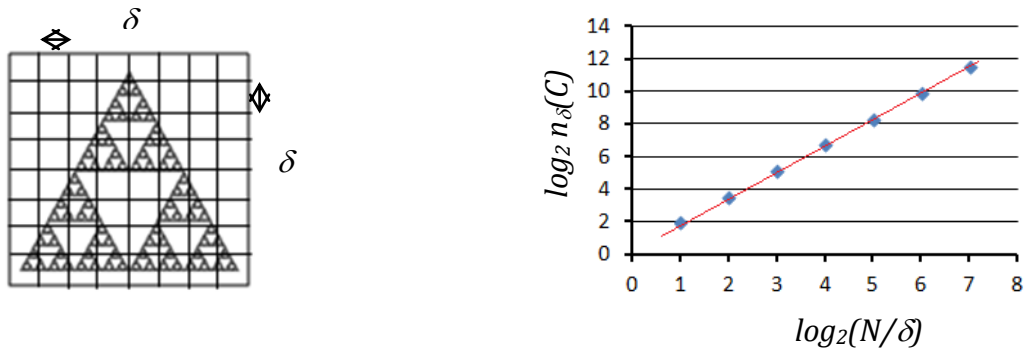

Figure 2-4: The regular subdivision and the linear regression used in box-counting algorithm.

If we denote the number of boxes of size δ that intersect a fractal curve C by $n_\delta(C)$, then the box-counting dimension of C is given by

$$D = \lim_{\delta \to 0} \left(\frac{\log_2 n_\delta(C)}{-\log_2 \delta} \right) \qquad (2\text{-}3)$$

The above method is usually implemented by iteratively halving the box size in each step, and counting the number of boxes that contain at least one point of the fractal. If N denotes the image size in each direction, the fractal dimension D is estimated as the slope of a linear regression line through the points on a log-log plot with $\log_2(N/\delta)$ along the x-axis and $\log_2(n_\delta(C))$ along the y-axis (Figure 2-4). The values obtained for a Sierpinski triangle with image size $N = 256$ are shown in Table 2-1.

δ	$n_\delta(C)$	$\log_2(N/\delta)$	$\log_2 n_\delta(C)$
128	4	1	2
64	12	2	3.58496
32	36	3	5.16993
16	108	4	6.75489
8	324	5	8.33985
4	979	6	9.93517
2	2952	7	11.5275

Table 2-1: Values generated by the box-counting algorithm for Sierpinski triangle.

2.3.4 Higuchi Dimension

The Higuchi's method is another efficient way of calculating the fractal dimension of a curve that has found several applications in the analysis of time series (Higuchi, 1988).

Higuchi's method is particularly suitable for a one-dimensional signal whose values at regular discrete intervals are available in the form $x(i)$, $i = 1, 2, ...N$. Several new data point series are constructed using an interval length δ, and starting value index m:

$$S_m(\delta) = \{ x(m),\ x(m+\delta),\ x(m+2\delta),\ \ldots x(m+ p\delta) \} \quad (2\text{-}4)$$

where

$$p = \left\lfloor \frac{N - m}{\delta} \right\rfloor \quad (2\text{-}5)$$

The length of the series in $Sm(\delta) = \{ x(\mathrm{m}),\ x(\mathrm{m}+\delta),\ \mathrm{x}(\mathrm{m}+2\delta),\ \ldots \mathrm{x}(\mathrm{m}+ \mathrm{p}\delta) \}$ (2-4) is calculated as a normalized sum of differences:

$$L_m(\delta) = \frac{N-1}{p\delta^2} \sum_{i=1}^{p} \left| x(m + i\delta) - x(m + (i-1)\delta) \right| \quad (2\text{-}6)$$

The mean length for each interval length δ is obtained as

$$L(\delta) = \frac{1}{\delta} \sum_{k=1}^{\delta} L_k(\delta) \quad (2\text{-}7)$$

As in the case of the box-counting dimension, the Higuchi dimension D_H is also computed as the slope of a linear regression line obtained using a log-log plot with $\log(\delta)$ along the x-axis, and $\log(L(\delta))$ along the y-axis.

An NxN image $I(i, j)$ must be converted to one-dimensional data before the above method can be applied. A common approach used for this is to add the values along each column to get a one-dimensional array of sums of pixel intensities:

$$x(i) = \sum_{j=1}^{N} I(i, j) \ , \ j=1, 2, ..N. \quad (2\text{-}8)$$

2.3.5 Generalized Renyi Dimension

The box-counting dimension outlined above can be extended to a generalized family of dimensions called Renyi dimensions. These dimensions use a probability measure function μ. In the context of the box-counting algorithm, μ_i represents the probability of finding a point of the fractal within a box with index i. The Renyi dimensions D_q are defined with respect to a non-negative parameter q as

$$D_q = \frac{1}{q-1} \lim_{\delta \to 0} \frac{\log_2 \left(\sum_{i=1}^{N} \mu_i^q \right)}{\log_2 \delta} \quad (2\text{-}9)$$

As a special case of the above, when q becomes 0, we get the box-counting dimension.

2.4 Analysis Using Higuchi's Method

In Section 2.3.4 above, we presented the Higuchi's method for computing the fractal dimension of an image. This method has become very popular due to its simplicity and speed of computation. The decomposition of a two-dimensional image into one-dimensional signals greatly helps in reducing the complexity of the algorithm. We used two fundamental fractal shapes, the Sierpinski triangle and the Sierpinski carpet (Figure 2-5) for our analysis of Higuchi's method.

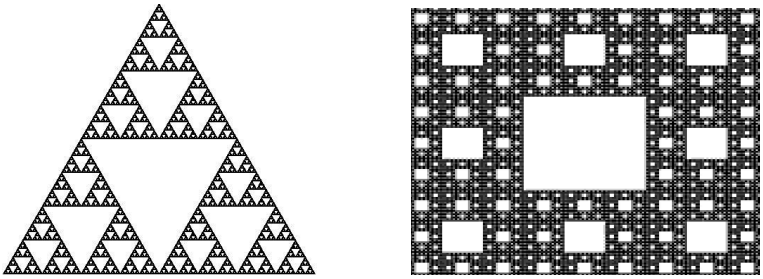

Figure 2-5: Images of the Sierpinski triangle and Sierpinski carpet used for the computation of Higuchi's dimension

The slopes of the linear regression of the log-log plots in Figure 2-6 gives the estimated fractal dimension of the Sierpinski carpet using the box counting method and the Higuchi's method.

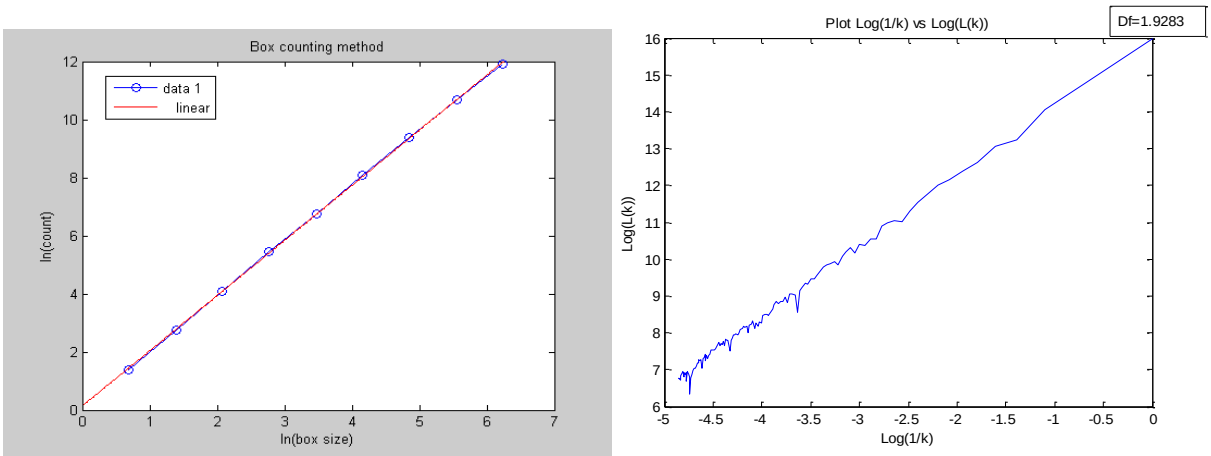

Figure 2-6: Double logarithm plots generated using the box counting method and Higuchi's method for the Sierpinski carpet image.

As can be seen in Table 2-2, the estimated fractal dimension using Higuchi's method results deviates more from the theoretical FD with a p-value of 0.7995 compared to the box counting method with a p-value of 0.1857. This difference is attributed to the horizontal and vertical projections of image values used in the Higuchi's method. However, the two algorithms seem to perform well in general, and can be used for efficient computation of digital images since the estimated FD values are sufficiently close to the theoretical values.

	Box counting	Higuchi 's Method	Theoretical FD
Sierpinski Carpet	1.9013	1.9283	1.8928
Sierpinski Triangle	1.5673	1.6519	1.5850

Table 2-2: Estimation of fractal dimensions of fractal images.

2.4.1 Parallel implementation of Higuchi's algorithm

In this research, the algorithms have been implemented in C++ with an open multi-processor (Open MP) support; this allows different portions of the computation to be executed concurrently by different processors. The parallelization is done over the loop using compiler directives, so the code runs in serial until the loop, then runs the loop in parallel, and finally reverts back to serial processing. The introduction of parallelism over the loops for both methods (box counting and Higuchi's method) achieved better results as the loops account for a large proportion of the execution time in the implementation. Open MP gives the instruction to the compiler that the iterations of a *for loop* may be executed in parallel. The Tables 2-3 and 2-4 give a comparison of computational time for both sequential and parallel implementations.

A major advantage of the Higuchi method against the box counting is the significantly less time required for the estimation of fractal dimension. This superiority is highlighted by the results given in Tables 2-3 and 2-4, where the CPU time required for the estimation of the fractal dimension of digital images for different sizes and dimensions are listed.

Computational Run Time in Seconds		
Windows length(N)	Higuchi Method	Box Counting
128	0.03	0.28
256	0.09	0.30
512	0.31	1.19
1024	1.20	7.77

Table 2-3: Computational run time without Open MP.

Computational Run Time in Seconds		
Windows length(N)	Higuchi Method	Box Counting
128	0.03	0.06
256	0.08	0.14
512	0.23	0.47
1024	0.85	1.94

Table 2-4: Computational run time with Open MP.

Specifically, both methods show that, as the size of the input image increases, the execution time for the computation also increases. Moreover, the two methods also consumed less time with the application of Open MP. The above experiments were conducted on a machine with Intel Pentium of 2.2GHz processor and 4GB of RAM.

2.4.2 Parameter Selection

In Higuchi's algorithm, selection of k_{max} is very important in the estimation of fractal dimension as this parameter determines the performance of the algorithm. Few studies in the past have attempted to address the issue of k_{max} selection: the authors in (Accardo, Affinito, Carrozzi, & Bouquet, 1997) selected $k_{max} = 6$ as the optimum value. Other studies have suggested that the selection of the k_{max} range should probably be subjected to further consideration if a large N is to be used, that is, the authors suggested increasing k_{max} for increasing N. In another study (Paramanathan & Uthayakumar, 2008), the authors provided an algorithmic estimation of k_{max}, inspired

by a divider method for *FD* estimation. In their approach, k_{max} of Higuchi's method was re-calculated for every *FD* estimation.

In our study, a wide range of k_{max} values was considered in the range 17-25. The image size *N=512* was used. Using each of those values, the *FDs* using Higuchi's algorithm were calculated for different Weierstrass sequences. In order to generate Weierstrass sequences; a deterministic Weierstrass cosine function (Tricot, 1995), sampled at *N* equidistant points was used:

$$W_H(x) = \sum_{i=0}^{M} \lambda^{iH} \cos\left(2\pi\lambda^i x\right), < H < 1, \qquad (2\text{-}10)$$

Where $\lambda > 1$ and fixed as $\lambda = 5, M = 26$, following (Esteller et al., 2001), and $x \varepsilon [0, 1], N = 512$ was used. The above defined function is Weierstrass's example of a continuous function that is nowhere differentiable and has a known theoretical *FD*. More specifically, parameter *H* is connected to the theoretical *FD* (FD_{th}) of the Weierstrass function by $FD_{th} = 2-H$. Using (2-10), Weierstrass sequences, each having a different theoretical *FD* value (i.e. *1.1,1.2,1.3,...,1.9*), were generated. In order to evaluate the performance of the algorithm for different k_{max} values, a mean square error (*MSE*) was estimated according to (2-11).

$$MSE = \frac{1}{n}\sum_{i=1}^{n}\left(FD_{th}(i) - FD_{e}(i)\right)^2 \qquad (2\text{-}11)$$

Where FD_{th} is the theoretical *FD* value for the images, FD_e is the estimated fractal dimension and n is the number of weierstrass sequences (of different theoretical *FD* values) used for the *MSE* estimation. Figure 2-7shows the *MSE* against k_{max} (Higuchi steps); it reflects the performance of the algorithm with respect to *k*-values. As can be seen in the figure, when *k* ranges from 17 to 25, the *MSE* value is almost zero and this means the expected fractal dimension and the estimated fractal dimension at these points are almost the same. These values of k_{max} were considered in *FD* estimation using Higuchi's algorithm when applied to fractal images.

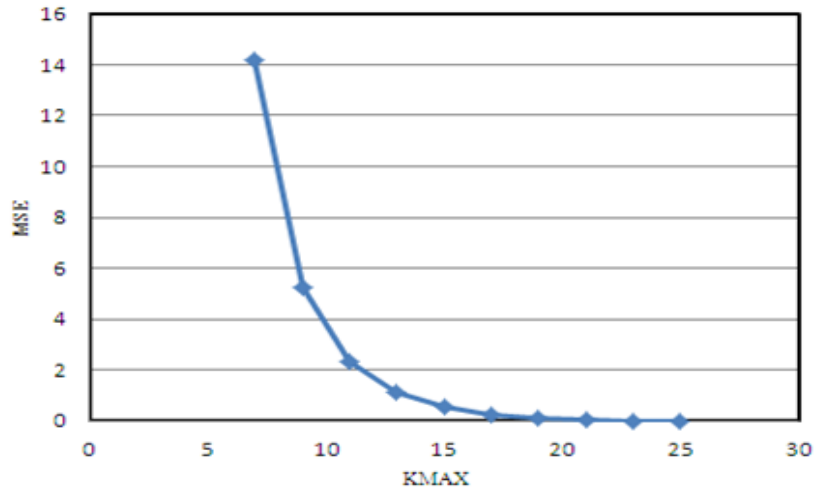

Figure 2-7: MSE for Higuchi's FD estimations for increasing KMAX values.

The values of *k* less than *7* led to a poor performance, which resulted in very High *MSE* values. However, as the value of *k* increases from 7, the value of *MSE* decreases.

Chapter Summary

The algorithms presented in this thesis rely on several concepts from the theory of fractals. This chapter has outlined some of the important properties of fractals such as self-similarity and measures associated with them. The most widely used measure is the fractal dimension. This chapter has discussed the essential concepts behind Hausdorff measures, box-counting dimension, Higuchi dimension and the generalized Renyi dimensions. The Renyi dimensions bear a close relationship with the multifractal spectrum of the measure μ. The next chapter gives an overview of concepts related to multifractal measures and the multifractal spectrum.

3 MULTIFRACTAL MEASURES

Multifractal measures provide a generalization of fractal measures presented in the previous chapter. Using these measures, complex texture characteristics can be associated with a range of scaling exponents yielding a singularity spectrum. This chapter gives an introduction to multifractal descriptors and their implementation aspects, important intensity based multifractal measures, and a computational pipeline for obtaining multifractal descriptors.

3.1 Introduction

The fractal systems described in the previous chapter fall into the category of mono-fractals whose characteristics are represented by a single exponent called the fractal dimension. We can generalize this concept into a wider and more complex multifractal system characterized by a continuous spectrum of exponents (called the singularity spectrum or multifractal spectrum). Thus, a multifractal system can be thought of as a combination of several fractal systems collectively exhibiting a variation of fractal dimensions at different scaling exponents. However, it should be noted here that we do not use multifractal analysis to characterize or identify multiple self-similar structures in an image. Since a fractal property can be considered as a statistical representation of roughness of the object, a more general multifractal descriptor encodes the statistical distribution of irregularities in an image, and we use them as just texture feature descriptors for image analysis applications. To provide some insight into the types of

multifractal descriptors we will be working with, an example of a tissue image and a multifractal spectrum computed from the image are shown in Figure 3-1.

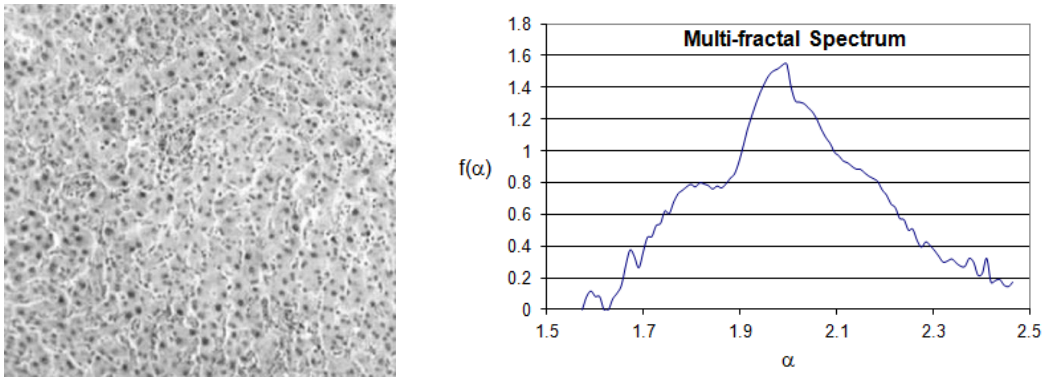

Figure 3-1: A tissue image and its multifractal spectrum.

In the previous chapter, we saw definitions of fractal dimensions using power laws based on δ-covers and probability measure functions. These measures represent the variations of regions occupied by a fractal shape with respect to some metric. We extend these ideas below to intensity measures, which are particularly useful for representing texture features. We again emphasize here the fact that the methods discussed in this thesis use multifractal analysis for characterizing texture features in an image, and not for identifying any type of self-similar properties or structures within the images.

3.2 Intensity Measures

An intensity measure $\mu_P(r)$ in the neighborhood of a pixel P can be defined as a function f of intensities within a square window W of size r, which is centered at P. Formally, we define this measure as

$$\mu_P(r) = f(I_Q), \quad Q \in W. \tag{3-1}$$

We require that the measure $\mu_P(r)$ satisfies the following properties:

$\mu_P(r) > 0$, for all P and $r > 0$.

$\mu_P(r) = 0$, if and only if $r = 0$.

$$\mu_P(r) \geq \mu_P(s), \text{ if } r > s, \text{ and all } P. \tag{3-2}$$

We use the non-decreasing property in the variation of $\mu_P(r)$ with respect to r to establish a power-law relationship similar to that used in the computation of the fractal dimensions. The four intensity measures given below satisfy the properties in Eq. $\mu_P(r)$

$\geq \mu_P(s)$, if r>s, and all P. (3-2).The values of the intensity measures are evaluated over concentric square windows centered at each pixel P Figure 3-2, with window size varying in steps of 2 pixels (r = 3, 5, 7, ...).

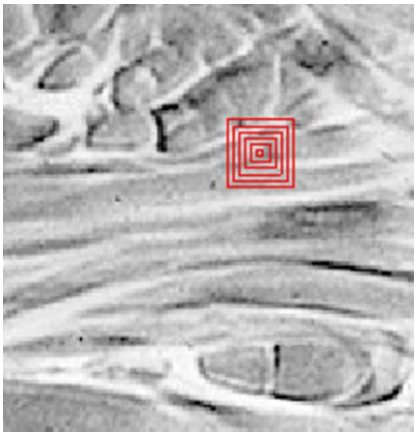

Figure 3-2: Windows around a pixel for evaluating intensity measures.

3.2.1 Sum Measure

The sum measure represents the sum of intensity values within the current window centered at P:

$$\mu_P^{(\text{sum})}(r) = \Sigma I_Q, \quad Q \in W. \tag{3-3}$$

The sum measure typically follows a quadratic curve when the width of the window is gradually increased. For the special case where the intensity value within the neighbourhood of P is constant, the value of $\mu_P^{(\text{sum})}(r)$ increases with r^2.

3.2.2 Iso Measure

The Iso measure represents the degree of similarity of the neighbouring pixels with P in terms of their intensity values.

$$\mu_P^{(\text{iso})}(r) = \#\{ Q \in W: \ I_Q = I_P\} \tag{3-4}$$

where # denotes the size of the set. The measure generally has much less rate of increase compared to the sum measure, but in the special case where the intensity value within the neighborhood of P is constant, the value of $\mu_P^{(\text{iso})}(r)$ also increases with r^2, similar to the sum measure.

3.2.3 Maximum Measure

The maximum measure gives the maximum intensity value found within the window W centered at P:

$$\mu_P^{(\max)}(r) = \max \{I_Q:\ Q \in W\} \qquad (3\text{-}5)$$

An important characteristic of the max measure to be considered is that if a pixel with value 255 (maximum gray level) is found within a window, subsequent increases in the width of the window will not produce any further change in the measure's value. Similarly, if the intensity in the neighbourhood of P is constant, the measure will produce a constant output.

3.2.4 Minimum Measure

The minimum measure (indirectly) represents the minimum intensity value within the window W centered at P - the minimum value is transformed to give a non-decreasing measure as required in $\mu_P(r) \geq \mu_P(s)$, if r>s, and all P. (3-2)

$$\mu_P^{(\min)}(r) = 255 - \min\{I_Q:\ Q \in W\} \qquad (3\text{-}6)$$

The characteristics of this measure are similar to that of the maximum measure. If the window contains a pixel with intensity value 0, subsequent increases in the width of the window will not produce any change in the measure.

The variations of the above four measures within windows around the pixel in Figure 3-2 are shown in four separate graphs in Figure 3-3. The x-axis in the graph represents half of the width of the windows, varying from 1 to 9. The width r of the window is $2x+1$. The first graph shows the values of $\mu_P^{(\text{sum})}(r)$ (Eq. 3-3). The second graph shows the values of $\mu_P^{(\text{iso})}(r)$ (Eq. 3-4) and so on. Being a plot of ISO values, the second graph gives the number of pixels that have the same intensity values as the pixel at the centre of the window.

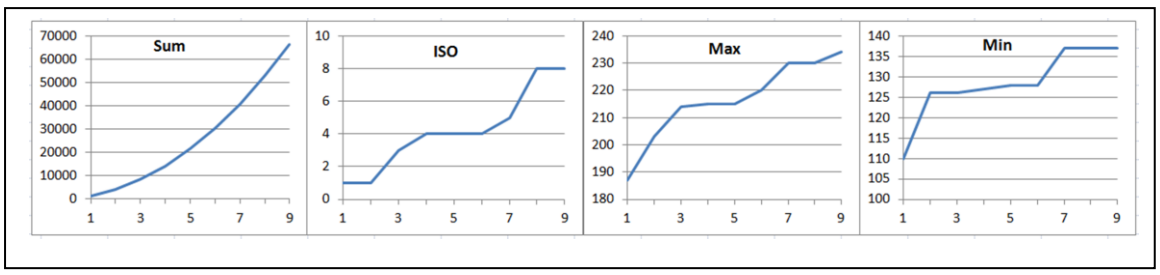

Figure 3-3: An example showing the variations of intensity measures in the neighborhood of a pixel.

3.3 The Holder Exponent and the Alpha Histogram

Using the values of the intensity measures $\mu_P(r)$ described in the previous section, we can explore how they scale with $r$and establish the power laws satisfied by them.

$$\mu_P(r) = C\, r^{\alpha_P}, \quad \alpha > 0. \tag{3-7}$$

where C is a constant of proportionality and α_P represents the Holder exponent for the power law of the measure under consideration at the point P.

As in the case of fractal dimension, the value ofα_P is calculated as the slope of the linear regression line of the log-log plot where $\log(r)$ is plotted on the x-axis and $\log(\mu)$ along y-axis. The linear regression lines and the corresponding values of α_P for the graphs in Figure 3-3 are shown in Figure 3-4.

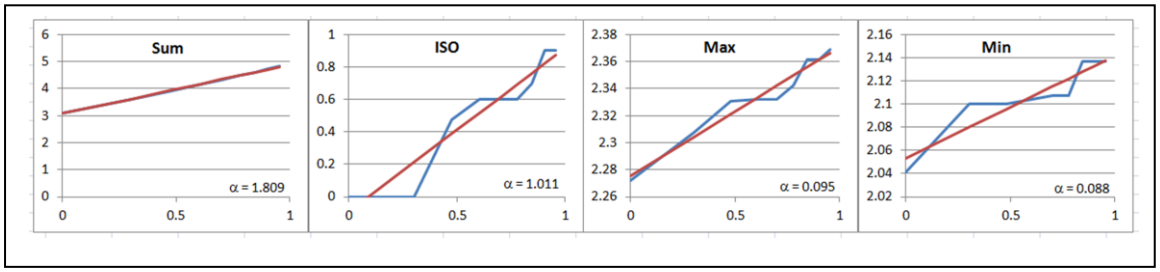

Figure 3-4: Graphs showing the computation of linear regression lines from log-log plots of measure values.

Since for every P, we get a value α_P of the Holder exponent for the chosen measure, we can form a rectangular array of values α_P having the same size as the original image. This two-dimensional array is called the α-image.

The range of α values $[\alpha_{\min}, \alpha_{\max}]$ computed from an image is further subdivided into a set of n discrete intervals $[\alpha_i, \alpha_{i+1}]$, $i = 0,1,\ldots n-1$, where

$$\alpha_i = \alpha_{\min} + \left(\frac{\alpha_{\max} - \alpha_{\min}}{n} \right) i \tag{3-8}$$

The number of pixels havingα_P values in each of these subintervals is counted, and this computational process yields the α-histogram of the α-image. Further, the subdivision produces different sections of the α-image. The pixel belonging to a subinterval is called an α-slice. The α-slices give a mutually disjoint partitioning of the α-image. Since each α-slice contains pixels belonging to a narrow range of αvalues; we can view an α-slice as the set of pixels that have similar intensity variations (with the same Holder exponent) within their neighborhoods. If we treat α_P as a local feature representing intensity

variations within the neigborhood of P, the α-histogram provides the relative strengths of each of these features, and is in itself an important feature descriptor.

As an example, the α values for the image in Figure 3-2 fall within the range [1.51, 2.1]. If we subdivide this range into seven subintervals, we get the α-slices shown in Figure 3-5. The corresponding α-histogram is also given in the figure. We used only seven subintervals for the convenience of showing the decomposition of the α-image in terms of α-slices in a figure. Generally we use a large (typically 100) subdivisions of the range of α values.

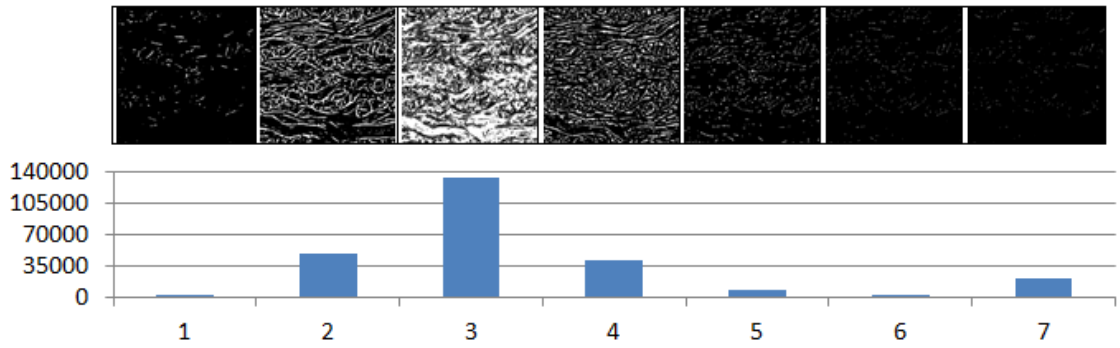

Figure 3-5: α-slices of the tissue image in Figure 3-2 and the corresponding α-histogram.

3.4 The Multifractal Spectrum

As mentioned in the previous section, the subdivision of the α range of an input image gives a decomposition of the image in terms of a set of α-slices. If we compute the fractal dimension of each of the α-slices, we get another powerful feature descriptor called the multifractal spectrum. The multifractal spectrum gives the variation of the fractal dimension with the Holder exponent α for a given intensity measure. It has been used as robust feature descriptors in image analysis applications including tissue image classification (Mukundan & Hemsley, 2010).

An example of a multifractal spectrum was given at the beginning of this chapter in Figure 3-1. This spectrum was generated by subdividing the range of α values into 100 subintervals, with each of the 100 α-slices generating one fractal dimension. Fractal dimensions with magnitude less than 0.4 are generally considered insignificant and not used as part of any feature vector. Similarly, values of α_{min} and α_{max} are also chosen to

eliminate the points at both ends of the fractal spectrum where high frequency oscillations are usually found.

The multifractal spectra computed for the tissue image in Figure 3-2 corresponding to the four intensity measures presented earlier in Section 3.2, are given below in Figure 3-6.

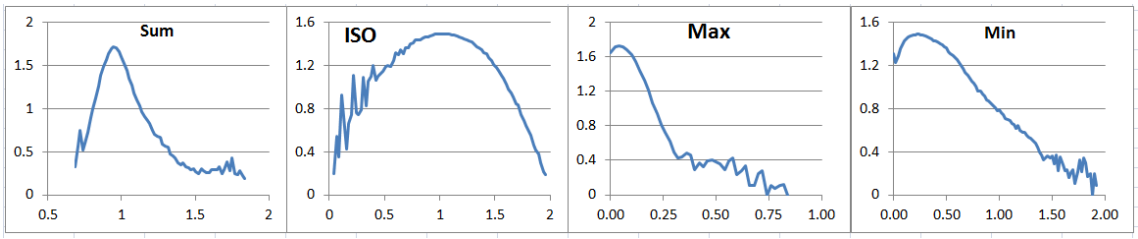

Figure 3-6: The multifractal spectra corresponding to four different intensity measures, computed for the input image in Figure 3-2.

3.5 The Renyi Spectrum

In Section 2.3.5, we outlined the equations for the generalized Renyi Dimension (Eq. 2-9) based on a probability measure. Chhabra (Chhabra & Jensen, 1989) proposed a one-parameter family of normalized measures $\mu(q)$ using the probability $P_i(\delta)$ of a pixel i to be in a box of size δ for a given grid partitioning of the image:

$$\mu_i(q,\delta) = \frac{(P_i(\delta))^q}{\sum_j (P_j(\delta))^q} \tag{3-9}$$

According to Chhabra (Chhabra & Jensen, 1989), the α-values (singularity strengths) can be computed as the average of the above measure weighted by $\log(P_i(\delta))/\log\delta$:

$$\alpha(q) = \lim_{\delta \to 0} \frac{\sum_i \mu_i(q,\delta) \log (P_i(\delta))}{\log \delta} \tag{3-10}$$

The Hausdorff dimension $f(q)$ of the above measure is defined as

$$f(q) = \lim_{\delta \to 0} \frac{\sum_i \mu_i(q,\delta) \log (\mu_i(q,\delta))}{\log \delta} \tag{3-11}$$

The one-parameter variation of $f(q)$ plotted against $\alpha(q)$ gives the generalized Renyi Spectrum of the input image.

3.6 The Computational Pipeline

In this section, we give an overview of the computational stages in the multifractal analysis of images. Even though these stages have already been described in the previous sections, the purpose of this section is to give an integrated view of the whole pipeline, showing the sequence of processes that should be implemented. In Figure 3-7, we provide a diagram of this processing pipeline consisting of three layers: the input layer, the computational layer and the output layer.

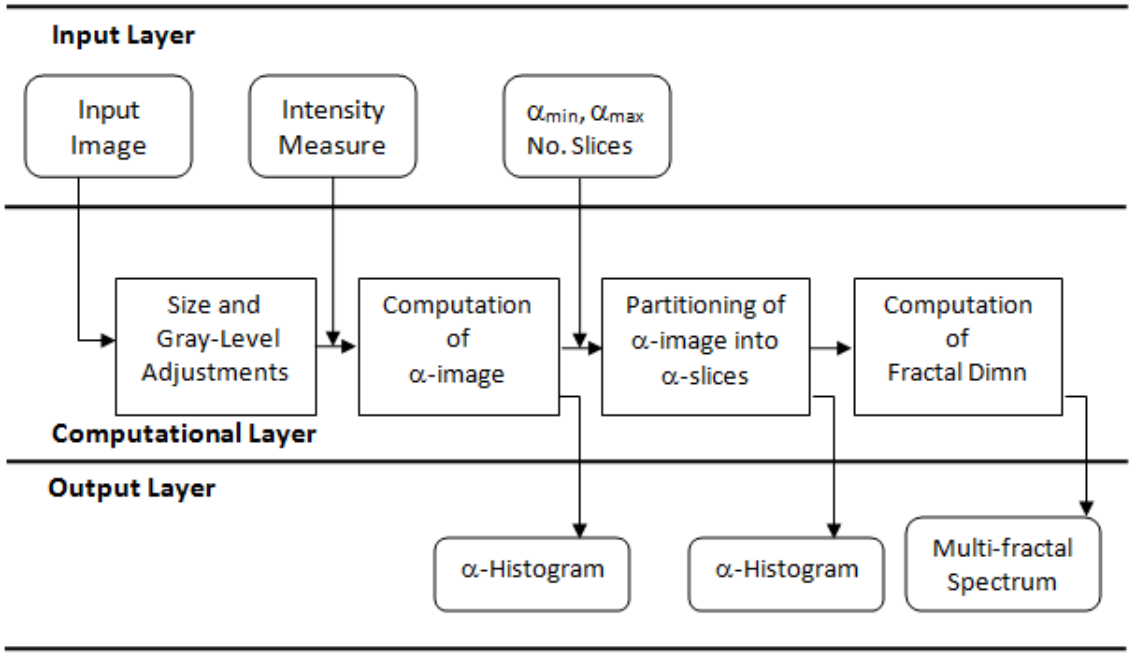

Figure 3-7: The main steps in the computation of multifractal spectrum of an input image.

Note that the output layer includes two types of α-histograms. The first α-histogram is obtained directly from the α-image, where each α value is transformed into the range [0-255] and represented as a gray-level. The second α-histogram is obtained by discretizing the α-range [α_{min}, α_{max}] into *n* number of subintervals, and counting the number of pixels having α values in each subinterval.

3.7 Chapter Summary

This chapter has presented the key concepts related to multifractal analysis of images. Four different types of intensity measures were introduced. Each of these measures provides the variation of an intensity parameter (such as the sum, max intensity value

etc.) within concentric windows around a pixel. We then relate this variation with increase in the width of the windows to obtain the power law, which a measure satisfies. The Holder exponent of the power law is denoted asα, and used to obtain an α-image. The α-image is further partitioned into a set of α-slices and their fractal dimension computed to obtain the multifractal spectra. Both the α-histogram and the multifractal spectra are used as feature descriptors in the methods presented in this thesis. We also use the generalized Renyi Spectrum in our work. The next chapter provides a literature review of multifractal analysis methods used in medical image processing applications.

4 LITERATURE REVIEW

This chapter provides the context for the research work reported in this thesis through a review of literature in the field of fractal based medical image processing. The review presented in this chapter shows the rationale of using fractal analysis algorithms and their significance in applications such as classification. Section 4.1 reviews prior work on general fractal analysis methods in medical signal and image processing and discusses important developments in the field leading to segmentation and classification. Section 4.2 reviews prior work and algorithms using multifractal measures and descriptors for biomedical image analysis. Section 4.3 gives a literature review of algorithms using the Renyi spectrum. Section 4.4 provides a review of feature selection methods used in classification.

4.1 Fractal Analysis in Medical Image Processing

A fairly comprehensive review of fractal based algorithms used in medical signal analysis was given by Lopes and Betrouni (Lopes & Betrouni, 2009). This paper highlights the importance of methods based on fractal geometry in characterising features in medical images. The paper starts with a formal introduction to fractals and discusses several methods for computing fractal dimensions. It also provides an excellent overview of multifractal analysis and methods for computing the multifractal spectrum, including a method for computing local Holder exponents from wavelet coefficients. The main contribution of the paper is a detailed review of

applications in the field of medical signal and image processing using fractal descriptors. Several methods for image and texture segmentation using image modalities such as Magnetic Resonance, Computed Tomography and Ultrasound have been reviewed. The paper concludes that fractal analysis is useful to quantify the distribution of local singularities and can be effectively used in many medical image segmentation problems. The concepts of the fractal and chaos theory were studied and algorithm for estimating the fractal dimension and its applications in biological sciences were discussed in detail in (Kenkel & Walker, 1996). Different methods of computing the fractal dimension in the time domain were analyzed and compared in (Esteller, Vachtsevanos, Echauz, & Litt, 2001), the analysis was performed over electroencephalogram data. However, the experiments conducted in this paper were mostly on biomedical signals, the study demonstrated that an accurate computation of fractal dimension (FD) and careful selection of algorithms are required for specific applications. The results reported in this study also indicate the advantages and disadvantages of each method for the FD computation. It was reported that the FD values were significantly higher in the hemisphere with arteriovenous malformations (AVM) compared to the hemisphere without AVM (Reishofer, Koschutnig, Enzinger, Ebner, & Ahammer, 2012).

FDs have been previously used to locate and identify regions of interest in various digital images (Jing, Zhang, & Yue, 2003; Kiselev, Hahn, & Auer, 2003)(Iftekharuddin, Jia, & Marsh, 2003). The complexities of the images within different locations can be varied with different measures of fractal dimensions; the regions or sections with the emphysema in the CT images, for instance, are expected to be more complex than the other regions without, and would have higher values of fractal dimensions. This thesis delves into this area by developing and analysing methods that use fractal dimension for detecting the locations of emphysema patterns in HRCT images.

4.1.1 Medical Signal Analysis Using Higuchi Dimension

Higuchi fractal dimension has found several applications in medical signal analysis due to its simple one-dimensional structure that allows fast computation. In the paper by Gómez(Gómez, Mediavilla, Hornero, Abásolo, & Fernández, 2009), it has been reported that the Higuchi fractal dimension of the signals from the patients with Alzheimer disease was found to have lower values compared to a group of elderly control subjects.

Their proposed method of analysis using magneto encephalogram (MEG) signals showed an accuracy of 88% in detecting Alzheimer's disease. In (Paramanathan & Uthayakumar, 2008), the Higuchi fractal dimension of the waveform was calculated and the criteria for determining the minimum and maximum values of the interval was established in order to improve the computational accuracy and speed. Their proposed method is particularly useful for analysing waveform signals such as MEG signals and ECG signals. Most previous work and experimental analysis on the Higuchi fractal dimension were used for medical signal processing as Higuchi's method uses one-dimensional signals.

The paper by Castiglioni (Castiglioni, Rienzo, Parati, & Faini, 2011) described how the structure of the blood pressure monitoring system could be determined by measuring the Higuchi fractal dimension of the mean arterial pressure and heart rate at both day and night times. The FD changes between day and night do not give substantial changes in standard deviation of arterial pressure and heart rate. Automatic detection of seizure applied to EEG data from different patients was achieved by using three different descriptors: the Katz's, Higuchi's and K-NN algorithms. It was observed that K-NN outperformed other algorithms in terms of seizure detection and robustness (Polychronaki et al., 2010).

4.1.2 Image Segmentation

Applications of fractals as texture features in medical images were comprehensively reviewed and analysed by an early paper by Yang (Kuklinski, 1994). In this paper, medical applications involving textural image segmentation and image restoration using fractal constraints were considered. The paper also proposed a discrete band-limited extrapolation algorithm for estimating the fractal dimension of a candidate segment. Subsequent to this paper, Ida and Sambonsugi (Ida & Sambonsugi, 1998) applied fractal coding for image segmentation and contour detection. The authors showed that the method was able to segment regions that have finely clustered pixel patterns. Their method could be used in medical images that are compressed by fractal coding. Immediately following the publication of this paper, another paper (Yang, Yin & Luo, 1999) also proposed a clustering algorithm for image segmentation using fractal dimensions as feature parameters.

Several new algorithms have since been developed for fractal based texture analysis, image segmentation and identification of regions of interest. In (Esgiar, Naquib, Sharif, Bennett & Murray, 2002), the authors proposed a method for fractal analysis of correlation and entropy features for the segmentation of colonic cancer images. Around the same time, Iftekharuddin (2003) developed a fractal based algorithm for detecting tumors in brain MR images. Lee (Lee, Chen, Chen, & Hsieh, 2005) developed an unsupervised segmentation algorithm for ultrasonic liver images based on the multi-resolution fractal feature vector.

4.1.3 Image Classification

One of the early developments in the field of medical image classification using fractal features is a classification algorithm using feature vectors derived from normalized fractal Brownian motion and an edge enhancement algorithm developed by Chen (Chen, Daponte & Fox, 1989). Matsubara(Matsubara et al., 1997)developed an automated-detection and analysis system by classifying digital mammograms into four different categories: Fatty, glandular and fatty, dense and high dense for mass candidates' detection. The accuracy of classification into benign and malignant masses using fractal dimension was found to be very high. Another approach for mammogram image classification was proposed (Don, Chung, Revathy, Choi, & Min, 2012). Their method uses a multilayer feed forward neural network for training and classification. They also presented results using fractal features such as fractal dimension, fractal signature and *K*-means clustering.

The use of digital image analysis tools was adopted to demonstrate how cerebral microvascular changes could be useful for the detection of stroke(Patton et al., 2005). This study suggested that retinal microvascular changes due to sicknesses like hypertension or diabetes could be detected and represented using quantitative measures. One of the limitations in this research work is that it is not clear the quantity of information that would be necessary to analyse the future risk of the diseases. A method for the detection and classification of brain tumour was developed by using the capacity dimension and correlation dimension. The results presented demonstrated that the correlation dimension possesses more discriminating power than the capacity

dimension in terms of differentiating between benign and malignant lesions (Martín-Landrove, Pereira, Caldeira, Itriago, & Juliac, 2007).

(Zaia, Eleonori, Maponi, Rossi, & Murri, 2006) applied the fractal properties to differentiate among three types of trabecular bone structure, that is, healthy young, healthy perimenopause, and osteoporotic patients from vertebra MR images. The gliding box algorithm was used for the estimation of lacunarity and the important parameters derived are used for the classification Zaia (2006).

The combination of different features to construct new powerful descriptor has been proving to yield excellent results. The texture classification using fractal and multifractal geometry can be classified based on fractal or multifractal features, or by combining features with other texture features. This thesis aims at improving the existing results by developing different multifractal based approaches for segmentations and classification of medical images. The purpose of the new methods is to solve the existing segmentation and classification problems of biomedical images. It is thus important to estimate the number of textures present in the image. In most cases, this estimation is difficult or even impossible to perform. In some cases, fractal analysis does not perform correct image segmentation. Indeed, some images are complex to study because they present irregularities and more regular zones at all scales, without following a clear law. In order to recover information from such singular images, multifractal formalism suggests studying the way in which the image's singularities are distributed, that is, the singularity spectrum, and equivalent to the entropy.

Thus, a number of studies have focused on texture segmentation using multifractal analysis (Yong Xia, Feng, & Rongchun Zhao, 2006), with application on MR and US images. Lopes et al. (2008) used the fractal dimension and the multifractal analysis for the detection of epileptic. This is achieved by formulating a 3D local singularity spectrum. The results showed that this approach could be effectively used for this application as one of the multifractal measures totally agree with the expert diagnostic.

In (Zhao & Matti, 2007a), the authors applied the textures with the volume binary patterns for dynamic texture descriptors by combining the motion and appearance. The constructed local descriptors were used for the analysis of different facial images. Though it is very nice that the extraction of features from a larger neighboring points is

possible, which also helped in the excellent classification results obtained. But since the features are local, it would be great to combine with the global features and test the performances with some images. A novel method to generate rotation-invariant features from the local non invariant patterns was investigated; the good thing about this approach is that it can be used for both static and dynamic textures. Moreover, different combinations of histogram descriptors obtained from the LBP features and the Fourier transformation of LBP histograms were concatenated such that the sign and magnitude components of the LBP were used in order to improve the discriminative capability (Zhao & Ahonen, 2010). In this case (L. Liu, Zhao, Long, Kuang, & Fieguth, 2012), the intensity based features extracted from the patches by calculating the differences between the centre pixel and the neighboring ones. Other descriptors obtained as a result of the histogram concatenation are the difference based descriptors and intensity based descriptors. The results demonstrated that the constructed features are powerful discriminating descriptors for both gray-scale and rotation invariant texture classification. The problem with this approach is the high dimensional features of the multi-resolution, which is prone to large time consumption. The solution here could be to provide or design a method for reducing the feature dimension by applying an appropriate feature selection approach. We also understand that it is possible to combine different LBP patterns using different computation in order to boost the textural classification performances. This idea has been used by researchers(Nanni, Brahnam, & Lumini, 2011), but the introduction of global information combined with the local descriptor could perform better. This paper used different variants of LPB to represent images. This is done by calculating the Fourier transformation of the features obtained from the uniform patterns. The results of the experiments significantly improved the classifier performance. The computation of the LBP in this paper(Ahonen, 2009) is quite different since the invariants histogram features are constructed globally. This is done such that the invariant calculation cannot be generated over every pixel, which keeps the computational complexity reasonable. However, the LBP has been very successful in the recent years in terms of accurate detections, segmentations, and texture classifications of medical images. One of the problems with the LBP is that it lacks global information and prone to noise. Furthermore, the different structural patterns of an image may have the same LBP code representation (Shrivastava & Tyagi,

2013). In this case, it could be very difficult to effectively differentiate between different medical images having the same LBP representation. This thesis would therefore be looking at combining the features from the LBP, which give the local behavior of the intensity distributions of the image, to the global features that could be extracted from the multifractal images. The proposed descriptors would be implemented and used in the textural classification of emphysema patterns of the HRCT images in this thesis.

Texture analysis has been widely applied in different areas of image processing and computer vision. These applications include image retrieval, object identification, medical image analysis and image segmentation. Local binary pattern (LBP) is a simple but effective way of characterizing the local intensity distribution of an image. Multi-resolution LBP or combinations of different LBPs descriptors and variants have demonstrated to be more effective in texture image analysis than ordinary LBP. However, since the LBP uses only the local characteristics of the image, this sometime limits the accuracy and the overall performances, especially when dealing with a high dimensional feature space (Kwak, Xu, & Wood, 2015).

Local histogram computation of digital images is a very powerful discriminating tool as it gives useful information that could be used in texture classification, retrieval and segmentation problems (Dan, Chen, Yang, & Wu, 2014)(Z Guo, Zhang, & Zhang, 2010)(L. Liu, 2012). The LBP descriptors could be implemented in the form of a rotation - invariant feature of the intensity values or without rotation (Ahonen, 2009; Zhenhua Guo, Li, You, Zhang, & Liu, 2012; T Ojala, 2002). It has been proven to be a very powerful tool in the field of texture image classification and retrieval. Verma and Zisserman (Varma & Zisserman, 2009) developed a model for scale invariant texture classification where the histogram of texton based dictionary is used as a descriptor. Some research work using fractal analysis for texture classification(Y. Xu, Yang, Ling, & Ji, 2010), have also been reported to be successful. In (Heikkilä, Pietikäinen, & Heikkilä, 2004), the author compares a center symmetric pair of pixels to construct LBP labels.

Additionally, the author in (Z Guo, 2010) combines the features from the normal LBP operator with the patterns from the local intensity differences and center pixel gray level. The effectiveness of the multifractal spectrum to classify the structure of different bread types in digital images were recently investigated (Baravalle, Delrieux, & Gómez,

2015). The authors used different fractal features of the image for the classification of bread crumb types with high accuracy.

A new texture descriptor was developed by combining the information from the spatial domain with the frequency domains (Xu, 2010), this is achieved by robustly encoding the multi-scale information of the textures; the proposed texture descriptor is very robust to scale and rotation changes. Furthermore, in (Zhao & Ahonen, 2010), different rotation invariant features are extracted from histograms of local non invariant patterns to construct a new descriptor, which is an effective descriptor for dynamic recognition. But despite these great successes that have been achieved by the LBP-based approaches in the texture classification, face recognition and analysis, it poses some challenges since it only gives the local properties of the object. Reference (Nanni, 2011) proposed two different fusion approaches by combining different LBP variants with the same radius and number of neighbourhoods as descriptors. The patterns are extracted in different forms using the Fourier transform to generate different descriptors to train a set of SVM. The research showed that the combination of LBP and its variant always outperform the individual descriptors, a good example is demonstrated by (Zhenhua Guo, 2012; T Ojala, 2002) where a joint histogram of LBP and its variant outperformed each individual descriptor (Timo Ojala, Pietikäinen, & Mäenpää, 2000). Reference (Kwak, 2015) proposed a data mining approach to extract the patterns from the computation of local binary codes and variants of LBP with multiple radii. The author uses the combination of the FS techniques to select the best set of features with the high discriminative ability on the training images.

The research also indicates that each of the LBP variants has its advantages and disadvantages; combining complementary variants may further improve their capability, but the challenge is the selection of the proper LBP features and how they are combined Kwak (2015). Since the traditional LBP has these shortcomings such as, lacking of global information and sensitivity to noise(Shrivastava & Tyagi, 2013), this study therefore proposed the development of a new descriptor by combining the local information from the LBP-based approach with the global features from the multifractal features in order to reduce some of the limitations of ordinary LBP.

Most of the previous work that uses the emphysema database(Sorensen, Shaker, & de Bruijne, 2010) were based on classification of emphysema patterns, but the quantity

and locations of the patterns in an image is another very important challenge that should be investigated (Mendoza et al., 2012; Nava, Marcos, Escalante-ram, Crist, & Perrinet, 2013; Sørensen, Shaker, & Bruijne, 2010). Much work has been done on the region of interest identification by using the general or classical approaches (Jayasuriya, Liew, & Law, 2013; Soares et al., 2014) .

4.2 Multifractal Analysis in Medical Image Processing

Multifractal features have been successfully used as a global descriptor for efficient classification in biomedical images. A method for identifying the region of interest in a mammogram image was developed by (Stojić, Reljin, & Reljin, 2006) . In (Soares, Janela, Pereira, Seabra, & Freire, 2014), a model for multifractal analysis has been proposed to assist the radiologist in diagnosing the breast cancer. In this case, the regions containing the cancer nodule were identified and the developed system presents very good classification accuracy in distinguishing the nodules locations between the regions with cancer and the regions without. Again, this paper extracts the self-similarity properties of the images to characterize the nodule properties. The results of the multifractal analysis were very impressive in terms of nodule detection. The author in (Vehel & Mignot, 1994) applied the multifractal characterizations of the images for edge detection. This is achieved by using the smoothing process, which is tantamount to the inverse of a classical approach. The good thing about this process is that the information is neither lost nor introduced. The results of the segmentation are very excellent. One of the limitations in this case is that the computational complexity is very high. The problem with this approach is that the segmentation method that was introduced may not be able to detect patterns of diseases like emphysema since it is not visible like micro-calcification or other visible nodules. This research therefore proposes to focus on identifying the patterns within the images using the Holder exponent and multifractal spectrum for solving this problem. The introduction of the Holder exponent would help us to evaluate the performances of the local descriptor in the analysis of the emphysema patterns.

In (Khider et al., 2013), the authors used the multifractal spectrum to detect osteoporosis in the trabecular bone texture by calculating the fractal dimension of the predominant fractal set. Their results showed that it is possible to use the fractal

dimension to distinguish between the ROI with osteoporotic and regions without. Yong and Hang (Ding, Dai, & Zhang, 2014) used the multifractal spectrum for automatic detection of the regions with tiny micro-calcifications. This is done by using the deviations between the normal tissues and the micro-calcifications. The results demonstrate that this approach is statistically superior to the earlier approaches. Identifying the ROI in the HRCT images could be achieved using the multifractal analysis by searching for the location in the image that best represent the class of the emphysema by using the appropriate spectrum. The paper by (Sorensen, Shaker, & de Bruijne, 2010) used the texture properties of the images to quantify the emphysema patterns. The LBP and joint histogram were used for the identification of regions of interest. The results showed good classification accuracy of 95.2%.

A wavelet-based multifractal descriptor was constructed by (Ramírez-cobo & Vidakovic, 2013) to analyze the mammography images. The primary focus in this paper is to detect micro-calcifications, differences in background between the cancer and non-cancer regions were used for this process. One of the drawbacks in this case is that it is sometimes possible for mammogram images of the normal and cancer regions to have the same background.

Cancer grading is an important field in computer aided diagnosis systems. This paper proposed feature descriptor by using fractal properties with four multifractal measures. The method developed was used to distinguish histopathological image textures and classify tumors and non-tumor areas (Atupelage, Nagahashi, Yamaguchi, Abe, & Hashiguchi, 2013).

The work done by Guillemet considered multifractal algorithm based on multifractal formalism for measurements (Vehel & Mignot, 1994b) implemented by Chhabra's method (Chhabra & Jensen, 1989). The authors used the measurement formulated to extract the region of micro-calcifications. Rangaraj(Rangayyan & Nguyen, 2005) proposed grid method for the computation of FD in the breast micro-calcification detection. The paper written by Hemsley and Mukundan (Hemsley & Mukundan, 2009) developed a two-pass algorithms as in Figure4-1 for the computation of multifractal spectrum. They used the calculated multifractal spectra for the classification of different tissue organs in the human body. It was discovered that multifractal spectra could be

used to derive global descriptors of the image shape with an acceptable inter-class variance.

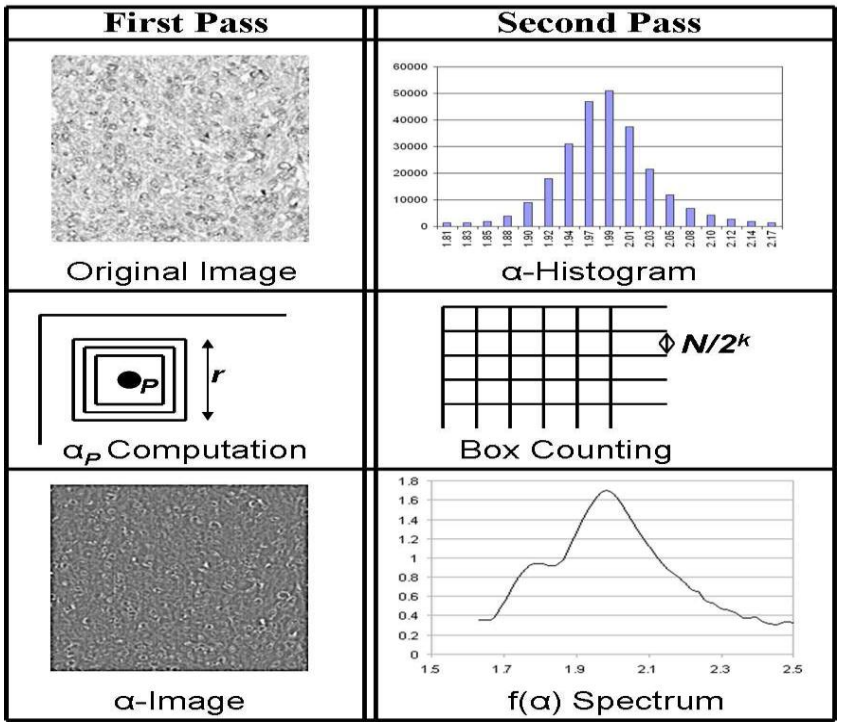

Figure 4-1: Two-pass algorithm for the computation of the multifractal spectrum of an image (Hemsley & Mukundan, 2009).

(Vasiljevic et al., 2012) applied multifractal analysis on microscopic images for the classification of metastatic bone diseases. The multifractal characteristic parameters calculated were used for differentiating three cases of bone diseases. The work demonstrated the effectiveness of multifractal analysis of medical images. Mukundan and Hemsley (Mukundan & Hemsley, 2010) introduced the multifractal formalism for the classification and retrieval of tissue images by using the geometrical characteristics of the multifractal spectra. The authors developed multifractal based feature descriptors derived from the calculated alpha-histogram and the multifractal spectrum in their work. Also, the paper written by Chiang and Mukundan (Tay, Mukundan, & Racoceanu, 2011) has explored the relationship between different multifractal measures of cell structures in tissues and the corresponding pleomorphic scores assigned by the pathologists. It was also concluded in the paper that multifractal could be a useful tool in the processing of tissue images by identifying the irregularities in cell

structures for estimating the Nuclear Pleomorphism (NP), and Tubule Formation (TF) grading scores.

In the literature, it has been noted that the key parameter in the analysis of biomedical images in most cases is the fractal dimension. The fractal geometry features of the image involve the estimation of fractal dimension and the multifractal spectrum. The computation of the multifractal spectrum is directly depending on the fractal dimension. In most applications, the final results of the segmentation and classification problems would totally depend on how accurate is the estimation of fractal dimension. Due to the complexities of most biomedical images, the effectiveness of the characterization of features is limited and could lead to high erroneous values. Higher errors in the calculated FD could directly affect the performance of the multifractal spectrum in terms of detections, identification and classification of images. In order to address this drawback, different methods of calculating the fractal dimension are proposed in this thesis to determine the most suitable methods for a specific problem.

A robust implementation for accurate computation of FD is therefore necessary to reduce the limitations of most studies as highlighted in the previous studies. Furthermore, in the existing algorithms, MR and US are the most common images investigated in the fractal and multifractal analysis. This thesis aims at investigating several experiments on the HRCT emphysema images. The fractal dimension showed interesting results in some images like MR and US but cannot provide a precise method of segmentation since it is calculated on the windows of the image. In addition, the FD cannot be used to capture all the useful information within the images as it only extracts the local properties and mostly, the global information are lacking. These limitations can be addressed by the implementation of different multifractal based methods such that the FD values of various locations within the images are combined to develop a multifractal descriptor whose features could be used for pattern classifications.

4.3 Medical Image Analysis Using Renyi Spectrum

The concept of the generalized Renyi Spectrum was earlier introduced in Section 3.5. Multifractal analysis based on Chhabra's approach is another powerful tool used in the analysis and classification of biomedical images such as the emphysema CT images. It can also be used as an analysis tool in the biomedical field, from one dimensional signal

(Electrophysiological signals) to 2D (medical imaging) and 3D (volume reconstruction from tomographic data). Multifractal based technique using direct determination of the singularity spectrum $f(\alpha)$was first introduced by (Chhabra & Jensen, 1989) in 1989. This is one of the simplest and the fastest ways of computing the singularity spectrum, $f(\alpha)$ and this makes it superior to other recently proposed approaches.

In paper (Yuxin Liu & Li, 1997), three new approaches of multifractal image analysis are presented. Two new measures are proposed based on thresholding with Renyi's Entropy for multifractal analysis. Holder exponent representation of the image is derived for image analysis and finally multifractal dimension distributions are presented for further analysis, but the research showed that the computational complexity of the fractal dimension is very high. Direct computation of the singularity spectrum of experimental data might be very difficult, but Chhabra's approach simplified the whole process, particularly data sets from low-dimensional systems (Chen, Sun, Chen, Wu, & Wang, 2004)(Vehel, 1996)(Perrier, Tarquis, & Dathe, 2006).

The $f(\alpha)$ provides a mathematically precise and naturally intuitive description of the multifractal measure with singularity strength α, whose Hausdorff dimension is $f(\alpha)$(Chhabra & Jensen, 1989). The main advantage of this method is that it is very simple and mathematically precise. Several methods have been used for the direct computation of the singularity spectrum (Mandelbrot, 2006)(Dubuisson & Dubes, 1994)(Broniatowski & Mignot, 2001)(Block, von Bloh, & Schellnhuber, 1990)(Lee et al., 2005) for segmentation and classification of images. Generalized dimensions $D(q)$ can be obtained with the method of moments for any image and the box size range.

In (Posadas, Giménez, Quiroz, & Protz, 2003), multifractal technique was used to quantify properties of soil spore by calculating geometric properties of individual pores from thin sections. The results showed that the multifractal $f(\alpha)$ spectra separated three soil groups based on the size and shape of pores. This paper (Lam & Li, 2010) used the fractal dimension and multifractal spectra to analyse the surface properties of the images. The study applied the gray scale threshold values with the fractal dimension of the image to describe and characterize the image.

Also in (Strauss, Teuber, Steidl, & Corona-strauss, 2013), the authors used 2-D diffusion filtering methods to denoise event related potentials (ERP) images. But in this paper, the nonlocal means method was proposed for ERP denoising in order to exploit the self-

similarity properties. It was concluded that the performance of the presented approach could be improved by using an application specific parameter adjustment.

4.4 Feature Selection

Feature selection (FS) algorithms can be broadly divided into two categories: The filter and Wrapper based approaches. A good example of the filter approach is the Relief and FOCUS algorithms, the Relief algorithm ranks each feature in the data set by assigning weights while the FOCUS is always searching for the minimal set of features that may be useful in classification (Q. Liu, Shi, Zhu, & Xiao, 2014)(D. Wang, 2015)(Han, 2011). Correlation FS as discussed in (Han, 2011) can be used to evaluate the predictive power of each feature and the degree of redundancy between them by selecting those subsets of features with low level of inter-correlation. The NB algorithm would be perfect for the data sets obtained as it is known to work well with high dimensional data (Domingos, 1997).

Diagnoses and treatment of most medical images can be very difficult due to the ever increasing volume of clinical cases processed by the radiologist. The manual collections of data are therefore subject to high error rates, imprecision and uncertainty (Kohavi & John, 2011; Papadopoulos et al., 2005). In the experiment conducted by (Domingos, 1997), the authors discovered NB to be superior to other classifiers even on data sets with many feature dependencies. Many studies in the literature have successfully applied NB for solving different medical problems (Blum & Langley, 1997; Yun-fu Liu, Guo, & Lee, 2011; L.-M. Wang, Li, Cao, & Yuan, 2006); the results showed that the NB outperformed other algorithms. NB had also shown excellent results even with small data sets as proved by (Demšar & Demšar, 2006)(Supriyanto, Yusof, & Nurhadiono, 2013) and it can also be used to circumvent the problems of over fitting during classification.

FS is the process of identifying and eliminating the irrelevant and redundant features from the data set in order to reduce the dimensionality of the data and allow the learning algorithms to operate faster as the model complexity reduces. This can sometimes increase the classification accuracy and facilitate easy interpretation of the models. One of the approaches to dimensionality reductions is to transform a high dimensional feature space into a lower dimensional space (H. Zhang, 2009)(Mikolajczyk

& Schmid, 2005) as this reduces the model complexities. In (Zhao & Matti, 2007a), the LDA is combined with the PCA to obtain high discriminative patterns from a high dimensional feature space derived from the descriptors.

The authors later applied Laplacian PCA (LPCA) to maximize the weighted local scatter instead of the global scatter of data as in the original PCA (Zhao & Matti, 2007a). The results achieved significantly improved the classification accuracy. In this research, in order to select the most highly discriminating features from the LBP-based feature vectors and the multifractal features, we propose to calculate the column area under the curve (AUC) of all the features extracted and find the maximum mean AUC values for the best four columns in each data set. The four columns with the highest average AUC values would be selected as a four dimensional feature vector space for each data set during the classification process.

SVMs have demonstrated highly competitive performance in many real-world applications, such as bioinformatics, face recognition and image processing (Fu & Wang, 2003; Mitra, Wang, & Banerjee, 2006; L. Wang, 2005;Marsland,2014). In (L. Wang, 2005), SVM outperformed most of the previously proposed methods in the diagnosis of cancer microarray data. Lining and Lipo (L. Zhang, Wang, & Lin, 2011) designed a biased maximum margin analysis and semi-supervised biased maximum margin analysis combined with the SVM to improve the performance of the traditional SVM as a relevance feedback for content based image retrieval (CBIR). In (L. Zhang, Member, Wang, Member, & Lin, 2012), a novel algorithm for subspace learning technique was developed using SVM to exploit the user historical feedback log data for a CBIR. Some of these classifiers might be tested with the datasets during the classification process in this thesis.

4.4.1 The Naïve Bayes Approach

The NB determines the class of a particular vector in the data by calculating its posterior probability. The posterior probability can be calculated using the Bayes theorem (Mangai, Nayak, & Kumar, 2013)(Bhuvaneswari & Kalaiselvi, 2012). For instance, the probability of class c given feature vector V can be mathematically represented as $P(c/V)$, If V is a feature vector: $f_1, f_2, f_3, \ldots, f_{n|f|,}$ represented by the set of classes $C = c_1, c_2, \ldots, c_{n|c|}$. The posterior probability of the likelihood and the prior probabilities

according to Bayes theorem are given as $P(c_i|V) = (P(V/c_i)\ X\ P(c_i))/P(V)$, where $P(\mathrm{V}/\ c_i)$is the likelihood and is the probability of the occurrence of vector V given classc_i. $P(c_i)$is called the prior probability and is the probability of class c_i. The likelihood $P(V/c_i) = p(V_1/C\ )x\ p(V_2/C)\ x\ \dots x\ p(V_n/C)$, after calculating the probabilities for each class, the classifier would select the class with the highest probability (Harry Zhang & Su, 2008)(Q. Liu, 2014; L.-M. Wang, 2006). Previous studies have shown that the performance of the classifier algorithms could be improved by using the FS (J. W. Xu & Suzuki, 2014). Section 6.4 discusses the FS approach in details and its experimental implementations.

4.4.2 The Bagged Decision Tree

Bagging is a type of ensemble learning to bag a weak classifier such as a decision tree on a data set to generate many bootstrap replicas of the data set. It is produced by reducing the variance of an unbiased base learner such as a decision tree. The process of training involves random selection of features as this technique increases the predictive power of the features by reducing the correlation between trees in the ensemble (Kallergi, 2005; L.M. Wang, 2006). Bootstrap aggregation as introduced by (Papadopoulos, 2005), is specifically based on constructing several training sets from the original set by resampling with replacement (bootstrapping) (Ruiz & Nasuto, 2005). The classifier algorithm constructed by the BT can be used to create a classification model in a form of decision trees for predicting the class labels of the unknown data represented in a form of a matrix. This matrix contains predictors or feature vectors that could be used in constructing an ensemble of classification trees that are used for predictions. The prediction error of the bagged ensemble is calculated by estimating predictions for each tree on its 'out-of-bag' observations, these predictions are averaged over the entire ensemble for each observation and finally the predicted 'out-of-bag' response are compared with the true label class corresponding to this observation.

4.5 Cascaded Features

In the previous work by (Premebida, Ludwig, Silva, & Nunes, 2010), two subsets of features were cascaded, one with laser-based features and the other with image-based features Comparisons with a set of single classifiers. The results presented by these

authors showed that the cascaded features performed better in terms of the classification accuracy. This paper (Demir, Bovolo, & Bruzzone, 2013) presented a sequential cascaded classification technique for exploiting the images between the target and the source domains for effective classification of the target domain.

One of the limitations that the proposed method is designed to eliminate is that; the system only generates a reliable classification to a pair of images from the time series and ignores the possible information present in the other images of the same time series. A 5-level cascaded H-Bridges Inverter based on back propagation (BP), Neural Network (NN) is proposed in (Wei & Cong, 2012), the PCA is used by NN to construct a new descriptor called PCA-NN. For comparison purposes, a BP Neural Network with PCA is used for another constructor known as PCA-BP. The PCA-BP is more accurate, but the PCA-NN drastically reduced the dimension of the training datasets and also the time computational complexity. Yunwei et al. presented an effective approach for the classification of radar emitter signals by using a cascaded feature extraction and a hierarchical decision technique.

An automatically simulation results demonstrate the effectiveness of the proposed approach for signal classification (Pu, Jin, Zhu, & Hu, 2006). (Doyle, Feldman, Tomaszewski, Shih, & Madabhushi, 2011) presented a cascaded multi-class pairwise classifier to identify the class of regions of interest (ROIs) of prostate tissues. The cascaded multi-class algorithm identifies each feature vector as one of the tissue classes. The main drawback here is that the classification performance as measured by the AUC is low for some tissue types that are difficult to discriminate.

The feature extraction performed using the combination of different classifiers and the performances of the proposed algorithms were tested with the AUC and equal error rates (EER). The feature level vision and match score level vision techniques were used for cascading the information from the classifiers. The results demonstrate a significant improved performance of the proposed approach (Tankasala & Doynov, 2015). In (Bahreini, Homayoun, & Gity, 2010), Fuzzy neural network (FNN) and a three-layer feed-forward multi-layer perceptron (MLP) were used for the classification of breast cancers. The results showed that FNN classifier has a better diagnostic performance than MLP classifier because FNN classifier has a greater accuracy and AUC than the MLP classifier. This approach could be implemented in the future in order to improve the

classification accuracy of the emphysema patterns by combining features of different histograms or descriptors.

4.6 Prior Research Using Emphysema Database

The work reported in this thesis used images from an online CT Emphysema Database (Sorensen, Shaker& de Bruijne, 2010) for experimental analysis and validation. More information about the images in this database are given later in Section 5.3.1. This section provides an overview of prior research work done using this database including the types of algorithms used for classifying emphysema patterns and measurements of performance obtained in each case.

One of the primary research works using this dataset is reported in(Sorensen, Nielsen & Lo, 2012)where the authors used Local Binary Patterns (LBP) as texture features and achieved 95.2% accuracy on a set of 168 image patches (each of size 61x61 pixels) in the dataset. The classification scheme used was *k*-nearest neighbour (*k*-NN). The regions of interest were characterized by feature histograms (such as LBP histogram), and the distance measure is computed as a dissimilarity between feature histograms. The authors also compared the performance of their algorithm using features such as Gaussian Filter Bank (GFB), GLCM and GLRLM. This work is an extension of a previous research reported by (Sørensen, Shaker & de Bruijne, 2008). In (Dharmagunawardhana& Mahmoodi, 2014), the authors presented model based statistical and structural texture features based on isotropic Gaussian Markov Random Fields to classify between normal lung tissues (NT), centrilobular emphysema (CLE) and paraceptal emphysema (PSE), with 77.4% accuracy. They used regions of interest of size 31x31 pixels extracted from the image patches available in the database. By adding intensity based features, they could improve the accuracy up to 95%.

An emphysema classification framework based on complex Gabor filters and LBP features and *k*-NN classifier is presented in (Nava, Escalante-Ramírez, Cristóbal, & Estépar, 2014). The authors also used Fisher kernel approach for dimensionality reduction. In their experimental evaluation of the algorithm, they achieved a precision rate of about 93.7%. Another method using Fisher kernels derived from Gaussian Bernoulli Restricted Boltzman Machine (GBRBM) and factored 3-way Restricted Boltzman Machine is presented in (Azim, & Niranjan, 2014). Their experimental

analysis using the emphysema database yielded a performance accuracy of approximately 86.9% in classifying emphysema patterns. The studies used 31x31 dimensional patches extracted from the centre of each 61x61 patch in the database.

Dubey & Singh (2016) introduced a novel feature descriptor called Local Bit-Plane Decoded Pattern and used it for biomedical image indexing and retrieval. Their experimental performance analysis using the 168 patches from the emphysema database showed an average retrieval precision (ARP) of approx. 75% and average retrieval rate (ARR) of 88%.A similar image retrieval system using local gray scale invariant features was proposed by Porto & d'Ornellas (2015) where they achieved an ARP of approx. 90% and an ARR of approx. 52%. However, in this study, they used only 37 HRCT slices containing the lower part of the lung.

Pei (2015) used a convolutional neural network (CNN) to classify emphysema images with automatically extracted features, and achieved a recognition rate of 92.54%. In addition to the images from the emphysema database, the author used 4560 CT scans from another database and extracted 25000 ROI patches of size 51x51 pixels. This dataset was then split into two sets containing 22000 patches for training and 3000 patches for cross-validation. A similar CNN based classification model is also reported by Karabulut & Ibrikci (2015), with an accuracy of 84.25%. In their experimental analysis, only 168 patches from the emphysema database were used, out of which 138 patches were used for training and 30 for cross-validation.

Some of the recent research work reported in the field use co-occurrence statistics for the extraction of rotation invariant texture features. This includes structural co-occurrence measures (Ramalhoa, Ferreiraa, Filhoa, & de Medeiros, 2016) that used 168 patches in the database, and local peak valley co-occurrence patterns (Agarwal, Mishra, Maurya, Chaudhary,& Murala, 2017) which used 50 HRCT slices.

As can be seen from the description above, most of the research work that was based on the emphysema database used 168 patches or ROIs extracted from the patches for a 3-class (NT, CLE, PSE) classification problem, and achieved accuracies ranging from 82% to 96% depending on the type of the algorithms and feature vectors used. So far, only our research work reported in this thesis as well as referenced in (Sorensen, Shaker & de Bruijne, 2010) have used multifractal descriptors for classification of emphysema patterns. The primary motivation for our work, as previously described, has been that

multifractal features are powerful descriptors of image texture and have similarities to other descriptors such as the LBP.

4.7 Analysis of Previous Work Using Fractal Measures

This thesis proposes to work on the efficient computation of the FD for effective analysis and classification of emphysema patterns in HRCT images since the accurate FD estimation could yield better results as previously stated. In addition, the second important area that would be investigated in this research is the Holder exponent. The Holder exponent of the local distribution of the intensity measure has been previously implemented and applied for the development of multifractal spectrum in CT images ((Hemsley & Mukundan, 2009; Irini, 2000; Mukundan & Hemsley, 2010; Reljin & Reljin, 2002; Stojić, 2006) but not directly used in the classification of images.

The major difference between the previous approaches and the proposed method is that the previous work applied a global descriptor (multifractal spectrum) for identifying different areas in biomedical images (Hemsley& Mukundan, 2009; Stojić, 2006), but this thesis also proposes to apply the Holder exponent (local descriptor) of the CT images for detecting the emphysema patterns using the local intensity properties. The computation of a multifractal descriptor depends on the calculated Holder exponent, which has been successfully used as a global descriptor for efficient classification in biomedical images. The introduction of the Holder exponent in the analysis of ROI could yield better results. Moreover, most of the applications of fractals and multifractals in the previous research were majorly on global characterization of biomedical images, it would be very necessary to investigate the performances of the local descriptor in the analysis of the emphysema patterns using the Holder exponent computation. Furthermore, different multifractal descriptors would be investigated using other efficient methods for the classification of images in the thesis.

It has also been observed in the literature that the Higuchi fractal dimension has been a very good measure for the characterization of signals; it was also noted that it has been majorly applied on signals. In fact, nobody has ever used the Higuchi fractal dimension for the analysis of medical images; this thesis therefore proposes to apply the Higuchi fractal dimension on biomedical images in order to evaluate its performances in terms of pattern identifications, quantifications, classifications and analysis. It was also noted

in the literature that a single value obtained from the calculated FD irrespective of the method used for the computation might not be enough to provide features for patterns recognition and analysis. The multifractal analyses would be thoroughly investigated in this thesis and used in the analysis of different applications. These analyses could involve extending Higuchi fractal dimension in the form of multifractal analysis for efficient classifications of emphysema patterns in CT images.

Another observation in the literature is that the multifractal analysis, which could be used to circumvent most of the drawbacks highlighted in the fractal analysis, has been used by few authors. Additionally, it has been majorly applied for segmentations of nodules; this thesis also proposes to develop different multifractal based techniques for the analysis and classifications of emphysema patterns, which could not be solved by ordinary segmentation approach. Furthermore, fractal dimensions and multifractal analyses are known to be global descriptors for signal and image processing, and they are both depending on the calculated singularity coefficient (Holder exponent) (Hemsley & Mukundan, 2009; Mukundan & Hemsley, 2010) of the pixel intensity.

(Takahashi, Kosaka, Murata, & Omori, 2009) applied a multifractal analysis for measuring the abnormalities of brain in MRI. The technique developed used the structural characteristics of the image obtained from the calculated multifractal dimension with some useful parameters to distinguish between normal and the abnormal parts of the brain. The results indicated that the multifractal dimension of the abnormal regions is significantly different from the normal regions. It was discovered in this paper that the accuracy of the results is totally depending on how accurate the multifractal dimension is. How can we improve the performance of the multifractal dimension in the analysis of other biomedical images?

This thesis proposes to investigate the applications of the Holder exponent in identifying the ROI across the digital images using the intensity distributions. The performances of the global and local features of the biomedical images would be thoroughly analysed in this thesis. Additionally, the concatenation of the local and global features could be used to develop new descriptors in order to improve the existing results. The next chapter will focus on the design and implementations of different multifractal methods that could be used to circumvent some of the limitations in the

existing literature. We use an emphysema image database to perform the experimental evaluation of our methods.

5 MULTIFRACTAL ANALYSIS OF EMPHYSEMA IMAGES

This chapter gives an introduction to the materials and methods used for emphysema classification using an HRCT image database. An overview of the disease patterns seen in HRCT images is given first, and then we discuss multifractal methods for extracting relevant features from the images for classification. This chapter presents the results of experimental analysis using several types of features such as the alpha-histogram, multifractal spectrum, Renyi spectrum, and Higuchi dimension.

5.1 Emphysema Disease Patterns

Emphysema is a disease that usually affects the lung tissue in human system, the most common symptom of emphysema is shortness of breath. Other symptoms can be cough, which is majorly caused by the production of mucus and wheezing. It develops gradually in human body and may sometimes go unnoticed. The patient with emphysema diseases struggles to exhale air completely, when they exhale, the lips block the flow of air, increasing pressure in the collapsed airways ("Emphysema imaging web portal," 2016).

The doctor can determine how the lungs work mechanically by carrying out some tests. This can be done by breathing into a tube that is connected to a monitoring device for recording the necessary information. Some of the necessary information could involve how much air the lungs can hold, how quickly the lungs measure can expel air, and how

much air stays in the lungs after exhaling for increased demand during exercise or other daily activities ("WebMDemphysema imaging web portal," 2016).

There are some medications that can be used to control this disease, which cause the passages to open more fully and allow free air exchange. The most common medication is albuterol; it is used for the patients with mild cases of emphysema while others like steroid medications can be used to reduce inflammation in the body. Pulmonary rehabilitation is probably the most effective therapy for patients with emphysema. Proper breathing methods, physical exercise and education about the disease can improve the quality of life and reduces hospitalizations ("WebMD emphysema imaging web portal," 2016).

Emphysema is the most common type of chronic obstructive pulmonary disease (COPD); it causes an inflammatory response in the lung. Diagnosing a COPD poses a challenging problem due to the irregularities in the lung image shapes and complex spatial variations. COPD is a chronic disease that makes it hard for the patient to breathe as the airways and alveoli do not get as much air as required. This disease is majorly caused by smoking, but air pollution, chemical fumes and/or dust may also contribute to the development of COPD. Research shows that COPD is the fourth major cause of death in the USA ("Emphysema imaging web portal," 2006). Over 12 million Americans have been diagnosed with COPD and health experts believe there could be another 12 million Americans who suffer from this disease but have not been diagnosed. Emphysema is one of the main components of COPD; it is characterized by loss of lung tissue and may eventually lead to gradual destruction of the lung. Detection and classification of emphysema are therefore very important as this may lead to improved understanding and improved computer aided diagnosis (CAD).

Diagnosing emphysema usually requires pulmonary function tests (PFTs), combined with a history of symptoms. The main tool through which the tests are performed is the spirometer. However, PFTs are not capable of detecting COPD at early stages (Sorensen, Nielsen, & Lo, 2012) (Dharmagunawardhana & Mahmoodi, 2014). In (Sorensen, 2012), the authors use an automatic approach for texture analysis of COPD. In their method, a *k*-NN classifier was employed for the quantitative analysis and computation of individual ROI probabilities. The result of the proposed approach was significantly

better in terms of discriminating between subjects with and without COPD than other measures of COPD in the literature.

The destruction of the lung parenchyma is commonly referred to as pulmonary emphysema, defined as the abnormal permanent enlargement of the air space accompanied by destruction of the alveolar walls.

5.2 Emphysema Patterns in HRCT Images

High Resolution Computed Tomography (HRCT) is a very effective scanning method that is more sensitive than chest radiography in measuring the type, extent and distribution of emphysema. Some patients with early emphysema, particularly those with early disease might still have the symptoms and this is the stage where HRCT is most useful.

Emphysema in HRCT is characterized by the presence of areas of abnormally low attenuation, which can be easily contrasted with surrounding normal lung parenchyma (Sørensen, Shaker, & Bruijne, 2010),(Chabat, Yang,& Hansell, 2003). Emphysema can be classified into three different classes: (i) centrilobular emphysema (CLE), defined as multiple small low-attenuation areas, (ii) paraseptal emphysema (PSE), defined as multiple low-attenuation areas in a single layer along the pleura often surrounded by interlobular septa that is visible as thin white walls, and (iii) and panlobular emphysema (PLE), defined as a low-attenuation lung with fewer and smaller pulmonary vessels(Chabat et al., 2003).

Examples of CLE and PSE, as well as normal tissue (NT) as seen in HRCT scans, are shown in Figure 5-1.

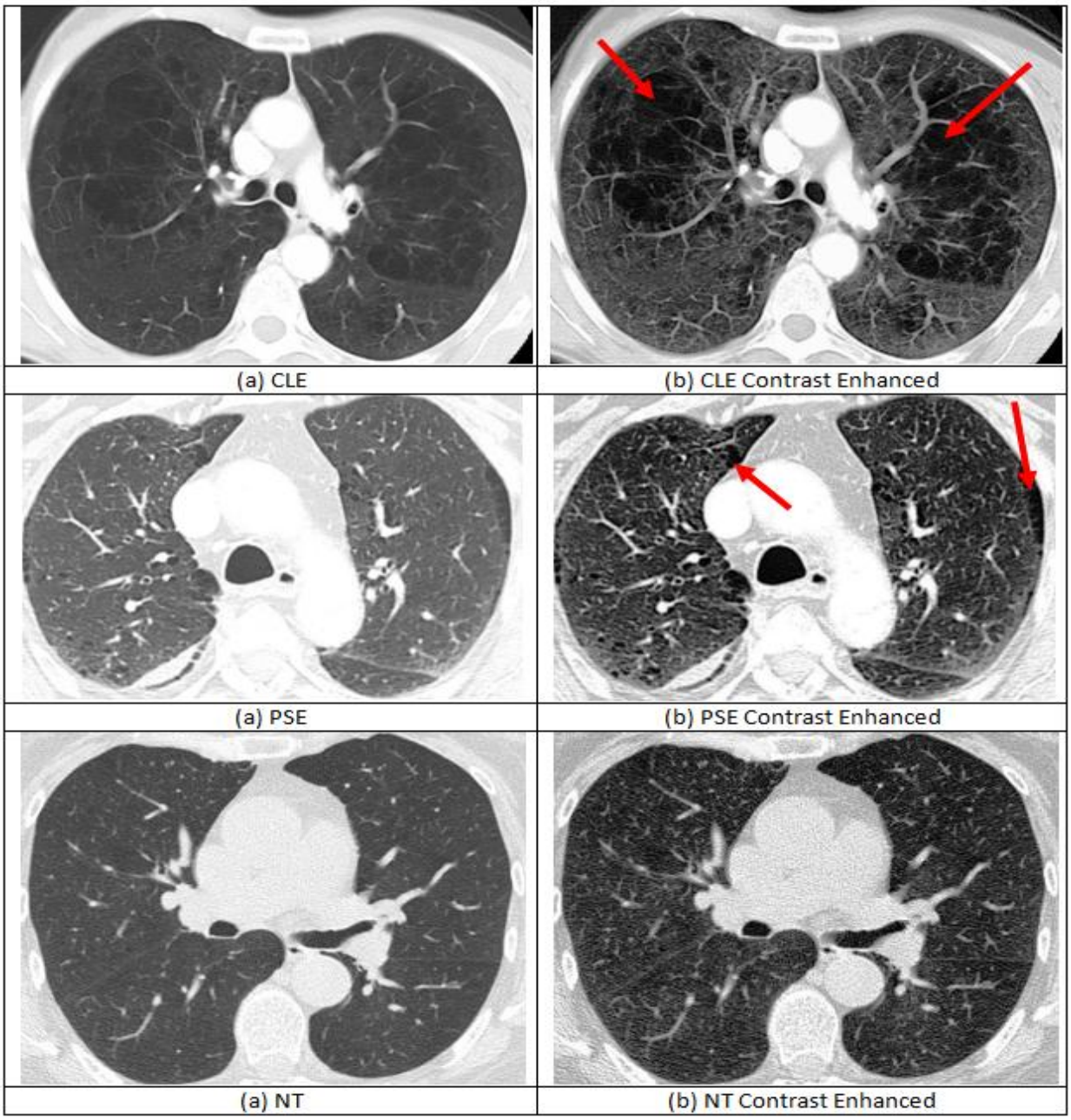

Figure 5-1: HRCT images showing emphysema disease patterns. The images in the first column were obtained from (Radiopaedia, 2016). Histogram equalization is used to enhance the contrast, and emphysema regions are indicated with a red arrow in the second column.

The first column of the figure shows original HRCT images taken from Radiopaedia (Radiopaedia, 2016), and the second column shows contrast enhanced versions obtained using histogram equalization (using Adobe Photoshop) for clearly showing the

disease patterns. We have not considered panlobular emphysema (PLE) in our study as PLE is often an advanced stage of a CLE (Stern, Swensen & Kanne, 2010).

Previous studies have shown several ways by which the CT imaging could be used for early detection of emphysema in patients with COPD (Stern, Swensen & Kanne, 2010).HRCT of early centrilobular emphysema (CLE) shows uniformly distributed tiny areas of low attenuation while in panlobular emphysema; HRCT shows either panlobular low attenuation or ill-defined diffuse low attenuation of the lung. Paraseptal emphysema (PSE) is characterized by subpleural well-defined spaces (Masashi et al., 2008).

The paper by Masashi (Masashi et al., 2008) comprehensively described emphysema diseases, different classification of emphysema and their properties. It is also demonstrated that features from HRCT images could form important quantitative measures for identifying different classes of emphysema and the assessment of their severity.

5.3 Materials and Methods

In this section, we present a detailed description of the datasets used in our research work and the multifractal features used for classification of the emphysema disease patterns.

5.3.1 Emphysema Image Database

The database used for this research comprises 115 HRCT slices (each of size 512x512 pixels) as well as 168 square patches (each of size 61x61 pixels) extracted from the slices (Sorensen, Shaker, & de Bruijne, 2010). The data came from a study group comprising 39 subjects (9 non-smokers, 10 smokers, and 20 smokers with COPD). The CT scanning was performed using General Electric equipment with four detector rows with an in-plane resolution of 0.78x0.78 mm, slice thickness of 1.25 mm. The slices were constructed using a high spatial resolution bone algorithm (Sorensen, Shaker, & de Bruijne, 2010). For each of the 39 subjects, HRCT slices corresponding to the upper, middle and lower parts of the lung were provided. A slice was reported missing in two cases, and therefore only 115 slices were made available in the database. For each slice, a value denoting the leading pattern (1=NT, 2=CLE, 3=PSE, 4=PLE) was provided in a

separate excel file. The values were obtained through subjective assessments by an experienced chest radiologist and a CT pulmonologist (Sorensen, Shaker, & de Bruijne, 2010). The 168 non-overlapping 61×61 pixel patches were extracted from slices belonging to three classes: NT (59 patches), CLE (50 patches), and PSE (59 patches). The emphysema pattern present in each patch (1=NT, 2=CLE, 3=PSE) was also provided in a separate excel file.

A review of prior research reported using the emphysema database was given in Section 4.6. Almost all research work used the 168 patches or smaller sections (regions of interest, typically of size 31x31 pixels) extracted from the patches to classify them into three classes, NT, CLS and PSE.

5.3.2 Generation of Test Datasets

As previously discussed, the emphysema database contains 168 patches of size 61x61 pixels that have been pre-labelled by a radiologist and CT pulmonologist would be used as the ground truth ROI. We extracted more patches from the full HRCT images of size 512x512 pixels (which also have the leading pattern annotated by the pathologist) and used them as the test dataset.

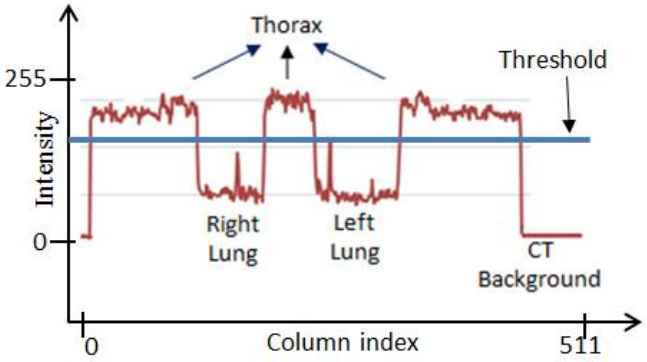

(a) Intensity variations in a typical HRCT image

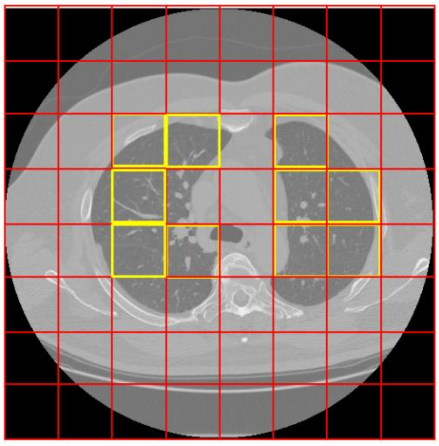

(b) Subdivision of an HRCT slice into 64x64 patches

Figure 5-2: Intensity regions and subdivision of HRCT images.

We subdivided the HRCT slices into a non-overlapping grid of patches of size 64x64 pixels as shown in Figure 5-2(b). The patches that contain at least 40% pixels belonging to the lung region are then selected. The intensity values along a row of an HRCT image

is shown in Figure 5-2(a). The values within the lung region are distinctly different from the thorax region, and can be used to identify patches containing at least part of the lungs located around the centre of an HRCT slice. On an average, two patches were extracted from slices corresponding to the upper part of the lung, nine from the middle part and seven from the lower parts, resulting in a total of 650 patches. Out of these patches, only very few have the leading emphysema pattern identified by the pulmonologist. 120 patches containing almost 80% low attenuation regions defining emphysema patterns as shown in Figure 5-1 are manually selected and used as the test set. The 168 patches given in the database is also split into a training set of 138 patches and a test set of 30 patches. For our classification experiments, we selected 90 patches from the training set (containing 30 patches belonging to each class) and 54 patches from the test set (containing 18 randomly selected patches from each class).

5.3.3 Features Based on Multiracial Spectrum

An overview of the multifractal based approach for the classification of emphysema is presented in Figure 5-3. The process involves several algorithmic stages, first of which is the calculation of the Holder exponent (α-values) at each pixel using a pre-selected intensity measure defined in pixel neighbourhoods. The α-values describe the variation in the local density of the image with respect to the chosen measure. The collection of all α-values for a given image is referred to as the α-image as described in the previous chapter. The range of α-values is subdivided into a number of small intervals, effectively decomposing the α-image into several disjoint image slices (details of the computation can also be found in chapter 3). Each α-image slice represents the collection of pixels in the input image having similar intensity variation (obeying similar power-law relationship in the intensity measure) across the pixel neighbourhoods. The traditional box counting method is used for the calculation of the fractal dimension $f(\alpha)$ of the α-images, providing the multifractal spectrum (Kenneth, 2013).

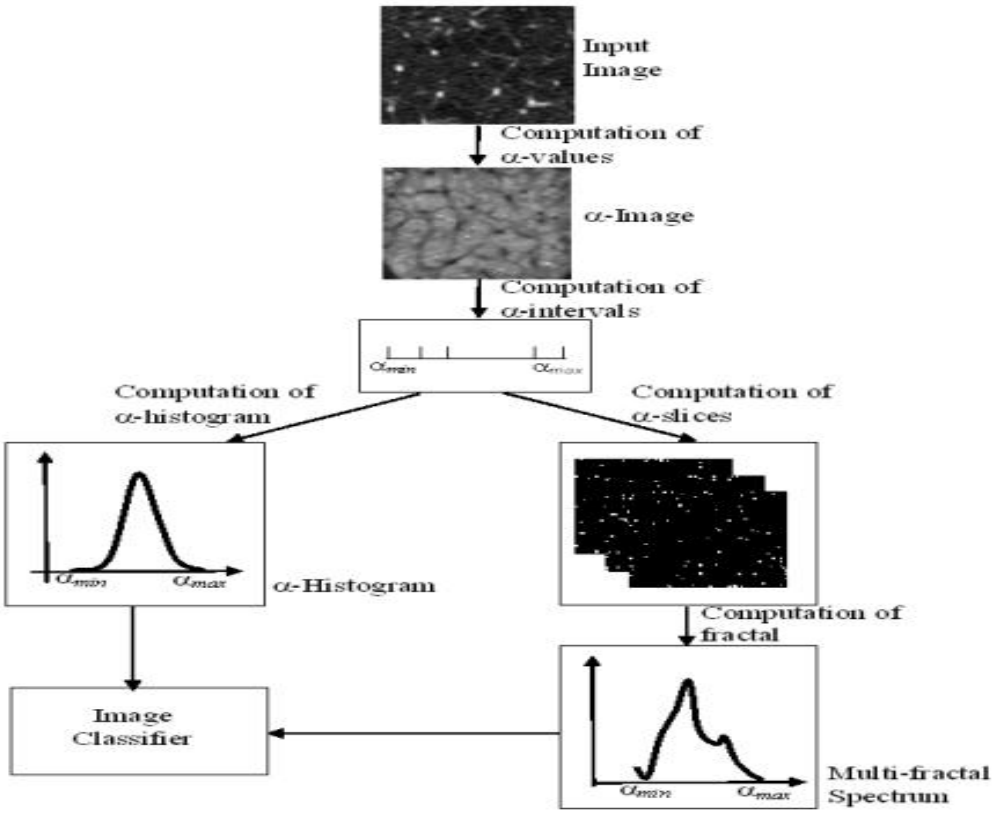

Figure 5-3: Flow diagram showing the computation of multifractal descriptors for an image classifier.

The multifractal feature descriptors used for classification can be calculated as follows. After finding the α values using any of the multifractal measure described in Chapter 3, an α-image can be created, that is, a matrix of the same dimension $M \times N$ as the original image but filled with values of $\alpha(m,n)$, with a one-to-one correspondence to image pixels $I(m, n)$. We further sub-divide the calculated *α-values* into n discrete intervals $\alpha_1,\alpha_2,\alpha_3,\ldots,\alpha_n$. Each interval α_k is defined as follows:

$$\alpha_k = \alpha_{min} + (k-1)\Delta\alpha_k, \qquad k = 1,2,\ldots,n. \tag{5-1}$$

$$\Delta\alpha_k = \frac{(\alpha max - \alpha min)}{n} \tag{5-2}$$

For experimental analysis, we used the value n = 100.Using *α-values*, important texture features that could be used in classification can be extracted as detailed below. Each α-slice can be characterized by its fractal dimension $f(\alpha_k)$. This fractal dimension is

computed using the well-known box counting algorithm (Kenneth, 2013).The following images and histogram values are readily obtained:

α-image:

$$I_p^{(\alpha)} = \left\lfloor \frac{\alpha_p - \alpha_{\min}}{\alpha_{\max} - \alpha_{\min}} \right\rfloor 255 \qquad (5\text{-}3)$$

α-histogram:

$h_k = \#\{\, p \mid \alpha_p \in [\alpha_k, \alpha_{k+1})\}$, $k = 1,2,\ldots,n-1$. (5-4)

α-slices:

$A_k = \{p \mid \alpha_p \in [\alpha_k, \alpha_{k+1})\}$, $k = 1,2,\ldots,n-1$. (5-5)

An α-slice A_k is a binary image of the only foreground pixels (with maximum intensity value), which satisfy the condition in (5-5). It therefore represents the collection of pixels in the original image where the values of the chosen intensity measure show the same power law variation.

If the actual value of αcomputed at a pixel lies within the sub-range k, i.e., if $\alpha_k \leq \alpha < (\alpha_k + \Delta\alpha_k)$, it is replaced by α_k, and that pixel is added to the corresponding α-image. A sample image obtained from (Radiopaedia, 2016), and five of its α-images are shown in Figure 5-4.

For our classification experiments, the Holder exponent (α-values) would provide the local descriptor, which describe the local behaviour of the intensity distributions of the images while the α-histogram and the multifractal spectrum would provide global feature descriptors.

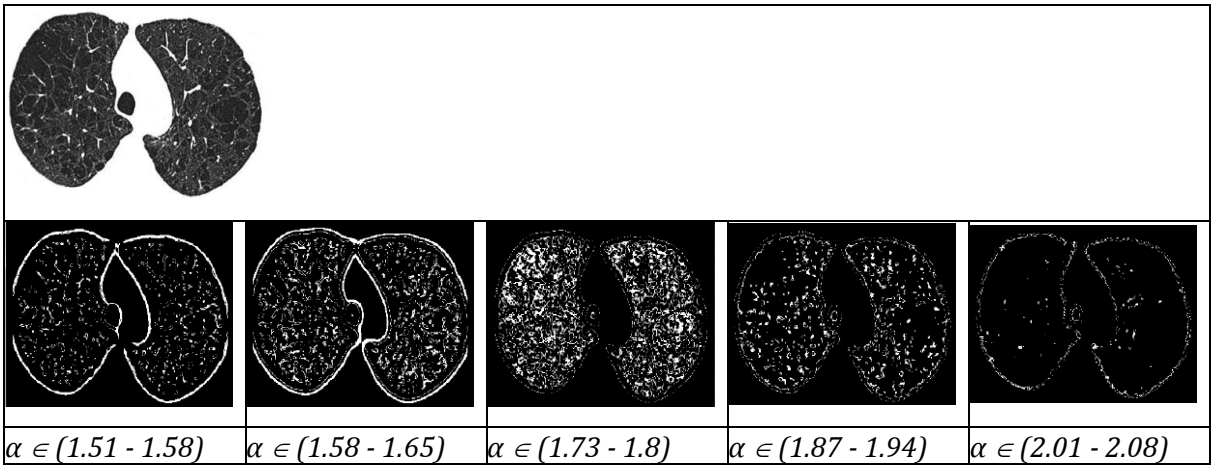

$\alpha \in (1.51 - 1.58)$	$\alpha \in (1.58 - 1.65)$	$\alpha \in (1.73 - 1.8)$	$\alpha \in (1.87 - 1.94)$	$\alpha \in (2.01 - 2.08)$

Figure 5-4:An HRCT image containing CLE (Radiopaedia, 2016) and some of its α-images.

Each α-image is covered by a regular grid of boxes with integer box sizes ε. The boxes containing at least one value of α_k are counted, giving the number $N_\varepsilon(\alpha_k)$. Boxes of different sizes are recursively taken into account and corresponding fractal dimensions are calculated for each α-image. Finally, multifractal spectrum $f(\alpha)$ is estimated as the linear regression of $ln(N_\varepsilon(\alpha_k)$and $-ln(\varepsilon)$.This process is very similar to that described earlier in Chapter 3 and illustrated in Figure 3-5. The multifractal spectra obtained using the sum intensity measure for the three classes NT, CLE, PSE are shown in Figure 5-5.

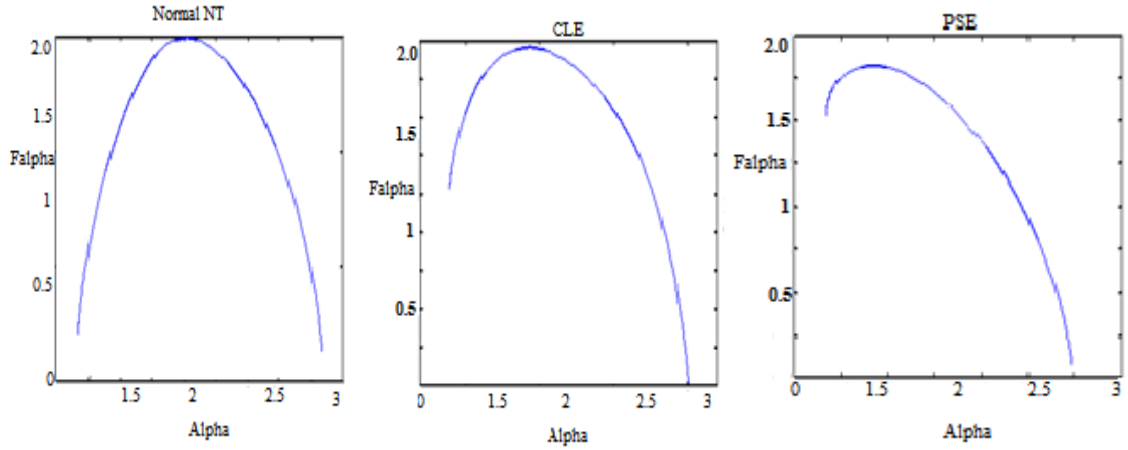

Figure 5-5: Multifractal spectra of the three classes of emphysema images.

There are some noticeable variations in the physical appearances of the spectra presented above. The singularity spectrum is usually displayed in the form of a parabolic shaped graph that attains its maximum at α_0, with $f(\alpha_0) = D_0$, where D_0 represents the box counting dimension of the input image. Additionally, the width of the spectrum $\alpha_{max} - \alpha_{min}$ for each class is different. Another feature of the spectra is the near symmetry with respect to the vertical line that goes through the maximum spectrum value (α_0, D_0). The values of the vertical difference can be expressed as $|f(\alpha_{\max}) - f(\alpha_{\min})|$.

5.3.4 Features Based on Renyi Spectrum

In addition to the usual multifractal spectrum computed using intensity measures, we can also use the generalized Renyi Spectrum computed using normalized probability measure presented in Section 3.5 to improve our classification accuracy. In this section, we also address some of the following research questions: Can Renyi spectra or

generalized dimension spectra have the multifractal properties features that could be used for the identification of emphysema patterns? How do the Renyi spectra and the singularity spectra vary with the emphysema patterns? How does the singularity spectrum computed using direct determination approaches relate to the multifractal spectrum that uses the intensity measures?

The results in Figure 5-6 show that Renyi spectra can also be used for the classification of the images due to a large inter-class variation of the spectra generated.

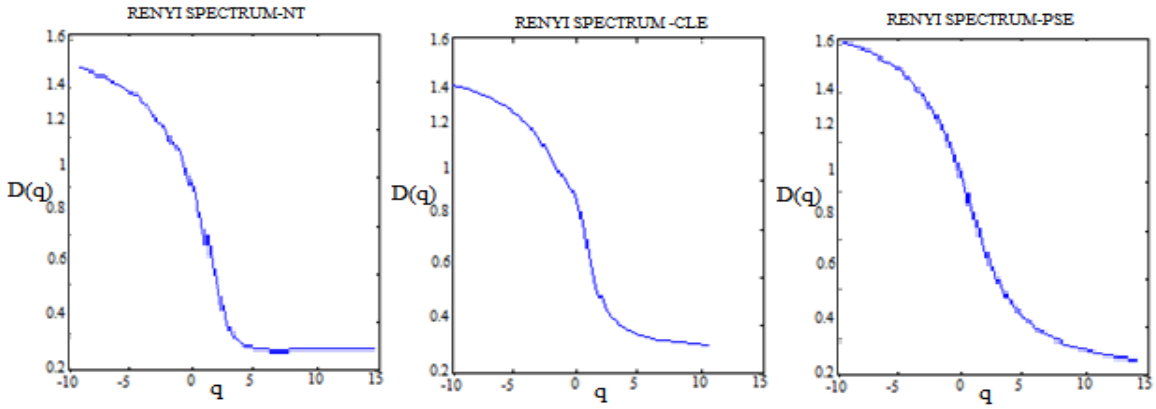

Figure 5-6:Renyi spectra for the three classes of emphysema images.

For the purpose of comparison, the average of the spectrum obtained from four different images within each of the three classes is plotted on the same graph in Figure 5-7.

The spectra presented in Figure 5-7can also be used to calculate the other relevant dimensions such as the information dimension, $D(q = 1)$, the correlation dimension $D(q = 2)$ and the capacity dimension$D(q = 0)$. The capacity dimension is independent of the quantity of mass in each box and provides global (or average) information of the system.

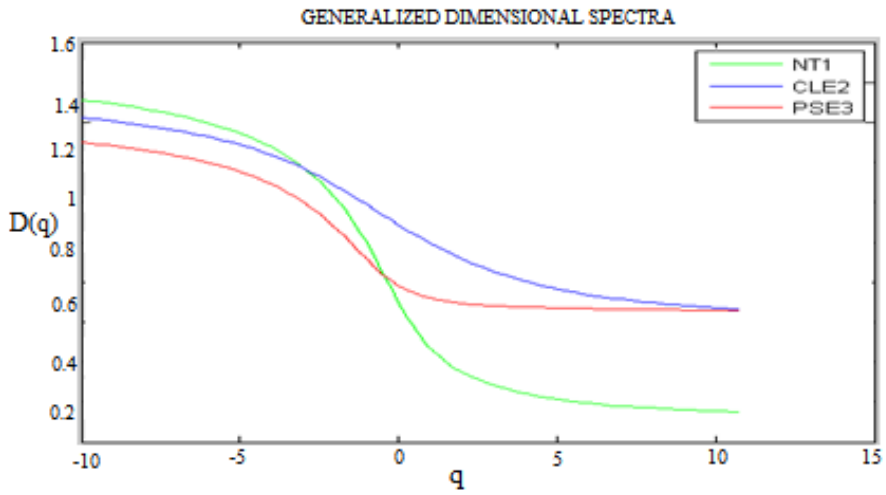

Figure 5-7:Inter-class comparison of Renyi spectra for emphysema image classes.

The graphs in Fig. 5-7 show some clear level of separations among the classes. This finding has motivated us to apply Renyi features for the identification and analysis of emphysema patterns in HRCT.

5.4 Feature Analysis Using ANOVA

This section describes the statistical analysis performed using analysis of variance (ANOVA)to confirm that the patches assigned to a class have features that closely match the features of ground truth patches belonging to the same class. ANOVA is a statistical measure for comparing the means of different samples in a dataset where each column represents an independent sample containing mutually independent observations. It is a very good measure to determine whether the samples are drawn from the populations with the same mean. This can be achieved by determining if a particular sample mean is statistically different from other samples using the p-value. The box plot of each column of the data would give a visual interpretation of the F-statistic and the p value. The larger the differences in the center lines of the box plot the higher the F-statistic values and the smaller the corresponding values of p.

As previously described in Section 5.3.2, 150 patches of size 64x64 pixels were extracted from the HRCT slices with the aim of using them as test data. It is necessary to first verify that the patches actually belong to the assigned classes by comparing their features with those computed for the ground truth patches provided in the database.

For a good performance of classification algorithms, it is also necessary to verify that intra-class variance of feature values is small.

The analysis of variance was calculated for each alpha image using the local characteristics of the alpha intensity values. The experimental results at this stage demonstrate that the images from the same patch class have minimum intra-class variance as the deviations in their group means are not statistically significant using the ANOVA. This process is repeated for the HRCT images of the same emphysema classes and the inter-class across the other classes. The results also show that the images from the same slice class have little or no variations in group means while the images across other classes have significant differences in their group means with about 95% confidence interval and a p-value < 0.0001.

In each group, it has been established that the values of the group mean between the emphysema class of the ground truth images, and the corresponding sub-images extracted from the slices overlap each other. The corresponding p-values in each test show that there are no significant differences between the images. The visual representation of the multi-comparison results demonstrating the graph of the estimates with comparison intervals between the group means of the normal tissues of the ground truth images and the image slice sub-regions are presented in Figure 5-8. As seen in the figure, the means overlap between 1.992 and 1.994, which is a clear indication that there is no statistical significant difference between the normal tissues of the ground truth and that of the corresponding HRCT slices. Additionally, the outputs also contain the results of the test in the form of a five-column matrix. For instance, the following entries in the row represent the estimates being compared above, the estimated difference in means of the alpha values, and a confidence interval for the difference.

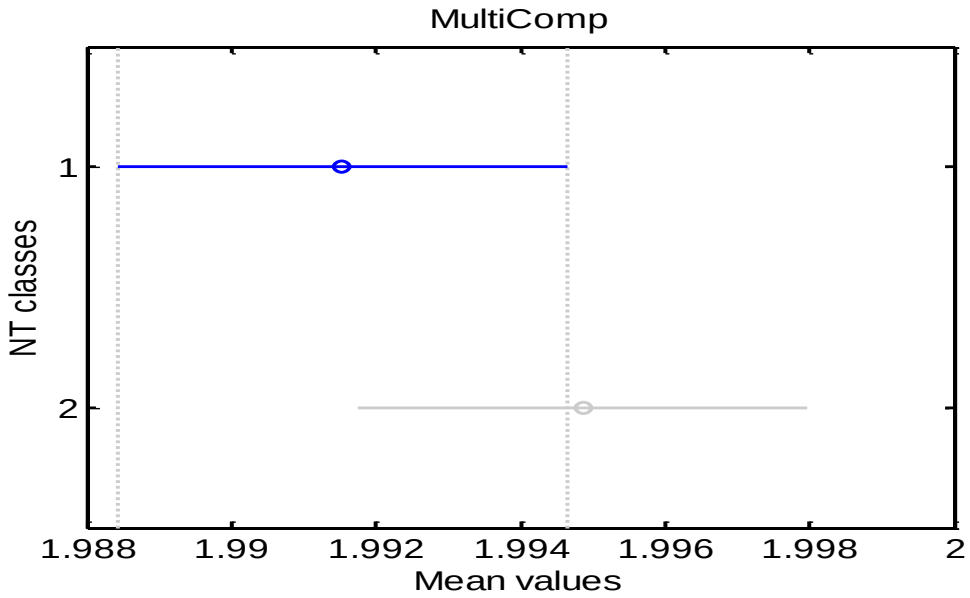

Figure 5-8: Group means between the normal tissues of the ground truth (blue) and sub-regions of slices (gray).

The absolute difference of means of the NT of the ground truth patches and the corresponding sub-image slices is estimated to be -0.0033 and a 95% confidence interval for the true difference of the means is [-.0096 0.0029]. In this test, since the confidence interval contains 0.0, it shows that the difference is not significant at the 0.05 level.

The same procedure is used for other emphysema classes between the ground truth patches and the HRCT sub-images of the three different lung tissue types; the top, middle and bottom, it was discovered that the differences between the patches and image slices are not significant.

The box plot of the sample results after resolving the local intensity distribution by the Holder exponent computation for the patch and the corresponding slice is presented in Figure 5-9.

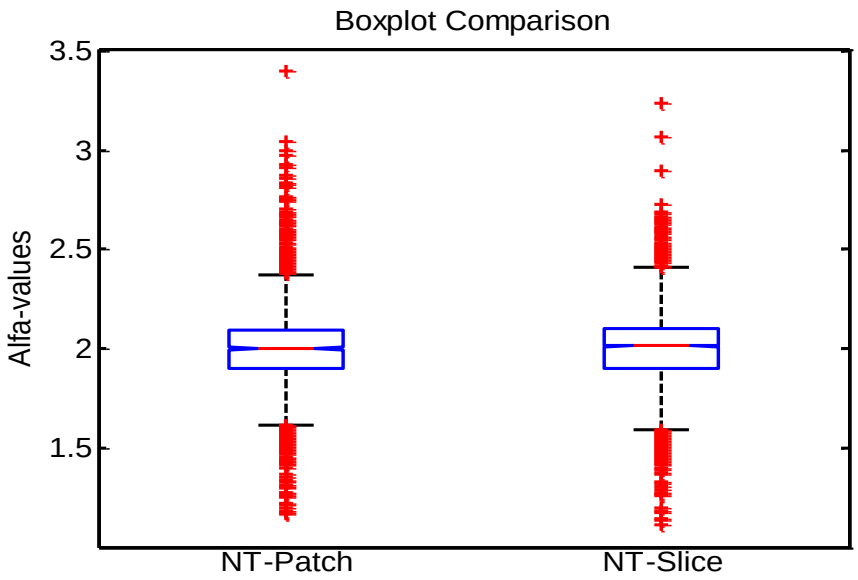

Figure 5-9: Box plots comparison between the ground truth patches and the slices of the normal tissue.

In Figure 5-8, the line at the middle of each notch represents the sample median, which can be used to display the variability between the samples. As can be seen in the figure, it has been clearly shown that the notches do overlap as there are no significant differences between them. In fact, the box-plot median lines are almost at the same level, this result is in line with the experimental results achieved in Figure 5-8 since there are no statistical significant differences (confidence interval of 95%).

5.4.1 Analysis Using Holder Exponents

The absolute mean differences of the calculated alpha-values generated using the Holder exponent approach between the normal tissues and the emphysema images, and the results of paired samples t-test were used to determine the locations of the emphysema patterns. For example, the mean alpha values for some of the sub-divided images in the three classes of emphysema are shown in Table 5-1 as an example. The mean alpha values in each class are also used to generate the linear regression models using the smoothing algorithms as this would help to determine the relationship between the classes, and also to visually display how the normal tissues are deviated from other classes. That is, the absolute mean differences between normal tissues and CLE pair classes and the NT-CLE pair classes are calculated for each sub-divided image

in order to determine the regions with the emphysema patterns. For instance, in Table 5-2, the absolute mean deviations between the normal tissues and the CLE and PSE classes revealed that few regions contain the emphysema patterns while others do not according to the paired samples t-test results.

The paired t-test results showed that there were statistically significant differences with a p-value <0.001 and the 95% confidence interval on the mean that does not contain 0 between the normal and emphysema images only in those regions with the emphysema patterns. The t-test results in those regions without emphysema patterns were not statistically significant as the p-values are higher than the significance level of 0.05 and the 95% confidence interval on the mean contains 0.

Sub-images	**NT_{MEAN}**	**CLE_{MEAN}**	**PSE_{MEAN}**	**|NT-CLE|**	**|NT-PSE|**
Image1	1.9953	1.9949	1.9949	0.0004	0.0004
Image2	2.0242	2.0491	2.0171	0.0249	0.0071
Image3	2.0818	2.0783	2.0596	0.0035	0.0222
Image4	2.0168	2.0117	2.0369	0.0051	0.0201
Image5	2.0738	2.1114	2.131	0.0376	0.0572
Image6	2.0789	2.1072	2.1265	0.0283	0.0476
Image7	2.0774	2.1153	2.1283	0.0379	0.0509
Image8	2.0622	2.1119	2.1202	0.0497	0.058

Table 5-1: Absolute mean deviations of CLE and PSE from the normal tissues

We observed that the p-values of the results from image1 to image4 are higher than the significance level and hence not statistically significant but the absolute mean deviations from emphysema images between image5 and image8 have lower p-values (p-value<0.0001) than the significant level of 0.05. These findings are also in line with the results in Figure 5-10 when the generalized regression models of the mean deviation values between the normal tissues and CLE classes are used.

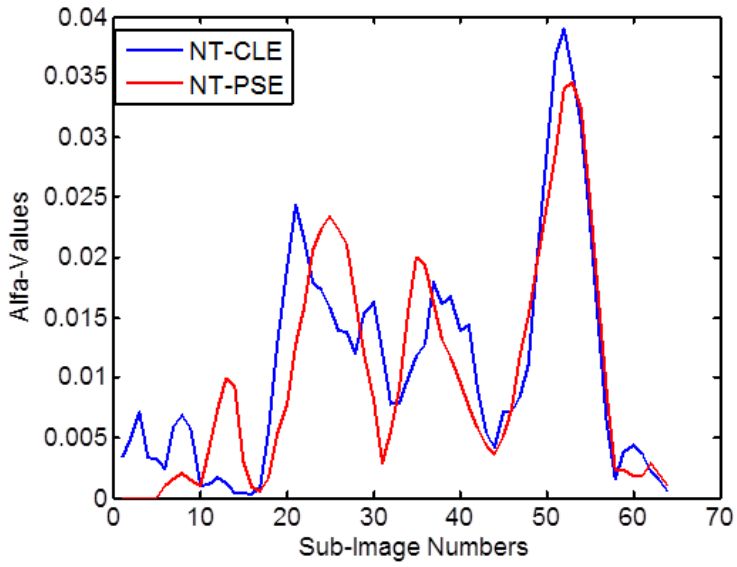

Figure 5-10: Absolute mean deviations between the normal tissues and other classes in 64x64 sub-images of the bottom slice.

The results of the absolute mean deviations of the normal tissues from other emphysema classes against sub-images are presented in Figure 5-10. In this case, sub-images in the range of 52 to 56 have higher deviation values compared to other regions even with a p-value < 0.0001 and 95% confidence interval for the mean. This indicates the presence of emphysema patterns since these particular regions have been verified by the paired sample t-test that the differences are statistically significant. These significant differences appear in almost the same regions for both CLE and PSE with just little differences. Other deviations across the regions in both graphs do not show significant differences when tested, which implies, these regions do not contain the presence of emphysema patterns.

5.4.2 Analysis Using Generalized Dimension

The results presented in Section 5.3.4 showed that parameters of the generalized dimensional spectra could be used as features for identifying and classifying emphysema patterns. The generalized dimension D_q is a decreasing function for all real q values within the interval $[\alpha_{-\infty}, \alpha_{\infty}]$. When q<0, the partition function emphasizes that regions in the distribution have less concentration of a measure, but the reverse is the case for q>0 (Mendoza et al., 2010).

The width of the $f(\alpha)$ spectrum, which can be defined as the difference between the most positive and negative moments of the singular spectra and the moment of order zero, i.e. $(\alpha_0 - \alpha_{q^+})$ and $\left(\alpha_{q_-} - \alpha_0\right)$ as used in the evaluation of singularity spectra of the emphysema patterns. The statistical analysis using the analysis of variance (ANOVA) showed that the multifractal attributes such as the width of the left side $(\alpha_0 - \alpha_{q^+})$ and the right side $\left(\alpha_{q_-} - \alpha_0\right)$ of the $f(\alpha)$ spectra, and the width of the $f(\alpha)$ spectra itself $(\alpha_{max} - \alpha_{\min})$ showed statistically significant differences only in the selected regions that contain emphysema with a p-value<0.05 and at the 95% confidence level. However, other regions without the presence of emphysema do not show significant differences with the aforementioned multifractal attributes. The corresponding Renyi spectra, D_q, for each sub-image of the HRCT slice in the range of moment order q between -10 and +10 are shown in Figure 5-11.

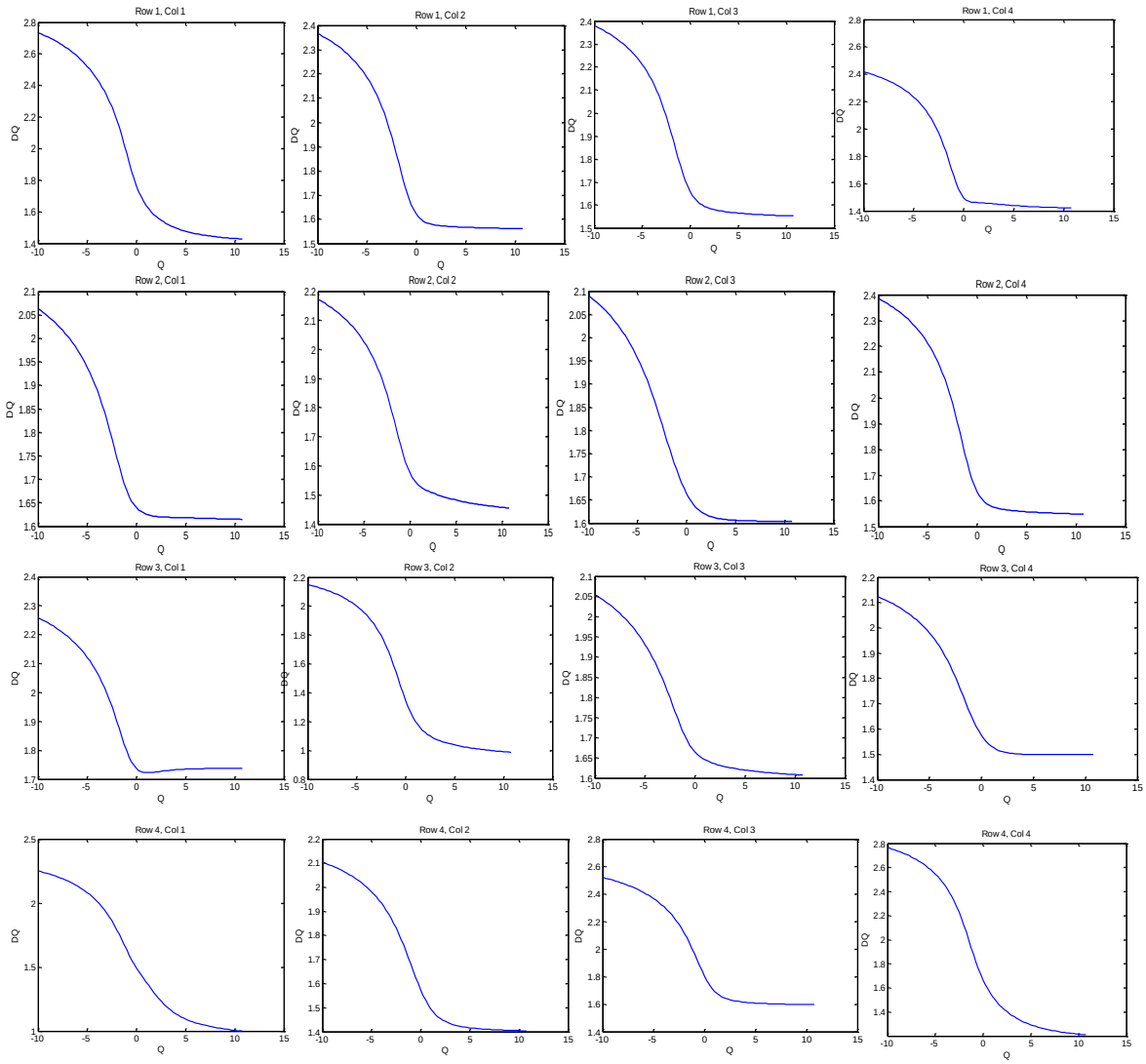

Figure 5-11: Renyi spectra of the HRCT slice for identifying ROI.

The generalized spectra exhibit pronounced decreasing D_q values with increasing q. When D_q are close together, it indicates a homogeneous structure, in a mono-fractal object, D_q estimations are always constant. The amplitude of D_q for each sub-image demonstrated that the few regions with the presence of emphysema patterns have higher values of D_q than the other regions without emphysema, which indicates that the heterogeneity of the emphysema patterns of the regions with the emphysema patterns are greater than other regions without. The higher deviations of the Renyi spectra in the two regions with the emphysema patterns compared to others without emphysema are due to the higher values of D_q in those regions. Further analysis of the results could be achieved as follows, by exploiting other multifractal parameters D_0, D_1 and D_2 as previously described. The Renyi parameters for a few sub-images using the capacity

dimension, information dimension and correlation dimension are presented in Table 5-2.

Sub-image	D0	D1	D2	D0-D2	D1/D0
1,1	1.7643	1.6397	1.5699	0.1944	0.9294
1,2	1.6222	1.5867	1.5756	0.0466	0.9781
1,3	1.6076	1.5862	1.5758	0.0318	0.9867
3,2	1.3472	1.2024	1.1239	0.2233	0.8925
4,3	1.8037	1.6937	1.6449	0.1588	0.9391
4,4	1.6667	1.5284	1.4365	0.2302	0.9170

Table 5-2: Generalized dimension parameters for selected regions on HRCT slice.

The results show that the sections with the emphysema patterns have statistical differences compared to the regions without emphysema patterns (P<0.0001). This can be seen in Table 5-2 as the regions presented have different characteristic dimensionD_q. Additionally, changes of $D_0, D_1 \, and \, D_2$ in the same spectra for different positions revealed statistical significant differences among them. The main criterial for discriminating between sub-images are the difference between D_0 andD_2, which help to statistically differentiate and characterize positions with or without emphysema patterns.

The values of $D_0 - D_2$ are larger for all regions with the emphysema patterns than all regions without emphysema patterns. The largest difference was found in the region with 4th row, 4th column, followed by the region with 3rd row, 2nd column. Significant statistical differences were found in those regions (P<0.0001), which contain emphysema patterns, but other regions without emphysema do not have significant statistical differences (P>0.05).

Additionally, the ratio of the two parameters D_1/D_0can be applied to describe the heterogeneity of the emphysema CT images. It provides proportional variation, but not the absolute variation (Martinez et al., 1999). Although, sub-images with dimensions

(1st row, 2nd column and 1st row, 3rd column) gave the largest ratio but no statistical significant differences were observed. The regions with 4th row, 3rd column and 4th row, 4th column, have the statistical significant differences ($p<0.0001$), which confirm the presence of emphysema patterns in those regions as this is in line with the results achieved with the differences in $D_0 - D_2$.

The variation of D_q with respect to q plus the shape of the multifractal generalized dimension spectrum showed that the emphysema CT image possesses self-similarity properties. The generalized dimensions were computed in the range of moment orders between -10 and +10. The singularity $f(\alpha)$ and the generalized dimensions D_0, D_1, D_2 and the quantities $D_0 - D_2$ and D_0/D_1 could be effectively used to discriminate the emphysema image classes, and identifying different regions on the HRCT images.

5.4.3 Analysis Using Higuchi Fractal Dimension

Most previous work and experimental analysis on the Higuchi fractal dimension were used for signal processing; no one has applied the Higuchi fractal dimension for the analysis of medical images. In this section, the Higuchi fractal dimension is implemented and applied for detecting the regions with or without emphysema patterns. The Higuchi dimension of each sub image is calculated for different classes of emphysema; that is, the NT, CLE and PSE. The calculated FD of an image patch alone could be used to detect the presence of emphysema. The computational aspects of Higuchi dimension were earlier presented in Chapter 2. The deviation in the FDs between the NT and other classes in both approaches is the key to measure the differences in the texture corresponding to the presence of emphysema patterns in a particular region. The calculated Higuchi fractal dimension for each sub-image across an HRCT slice and the corresponding absolute differences are presented in Table 5-3.

The differences in the FDs in the regions that are statistically significant using the analysis of variance (ANOVA) indicate the presence of emphysema, with a p-value < 0.0001. The NT-CLE range of FD differences detects more presence of emphysema than the NT-PSE. Although, very large FD differences in both CLE and PSE show the presence of emphysema in the images.

	FD of the emphysema images using the Higuchi dimension method				
Patch ID	NT-FD	CLE-FD	PSE-FD	| (NT-CLE)|	| (NT-PSE)|
E11	1.114	1.0734	1.145	0.0406	0.031
E12	1.3131	1.5	1.0299	0.1869	0.2832
E13	1.2569	1.3059	1.0661	0.049	0.1908
E14	1.0982	1.0724	1.2018	0.0258	0.1036
E21	1.0982	1.8064	1.4507	0.7082	0.3525
E22	1.4198	1.507	1.3635	0.0872	0.0563
E23	1.5987	1.3909	1.5404	0.2078	0.0583
E24	1.5478	1.4341	1.4494	0.1137	0.0984
E31	1.1505	1.1799	1.161	0.0294	0.0105

Table 5-3: Higuchi FDs of sample image patches

In Figure 5-12, the FD differences between normal image and the emphysema images are plotted against sub-images. The normal NT-CLE has higher FD differences than the NT-PSE in some sub-images while the NT-PSE also has higher FD differences in few sub images than NT-CLE.

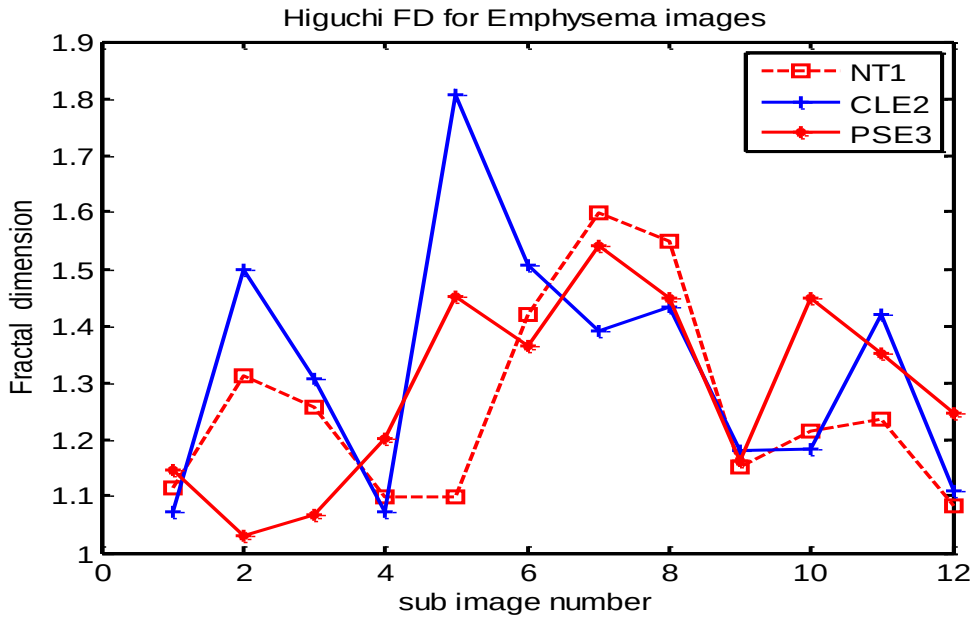

Figure 5-12: FD of CT emphysema images against the corresponding sub-image number.

This means there is a presence and detection of more emphysema patterns in the CLE than the PSE image slice since the FD differences in NT-CLE are generally higher in most sub-images than that of NT-PSE.

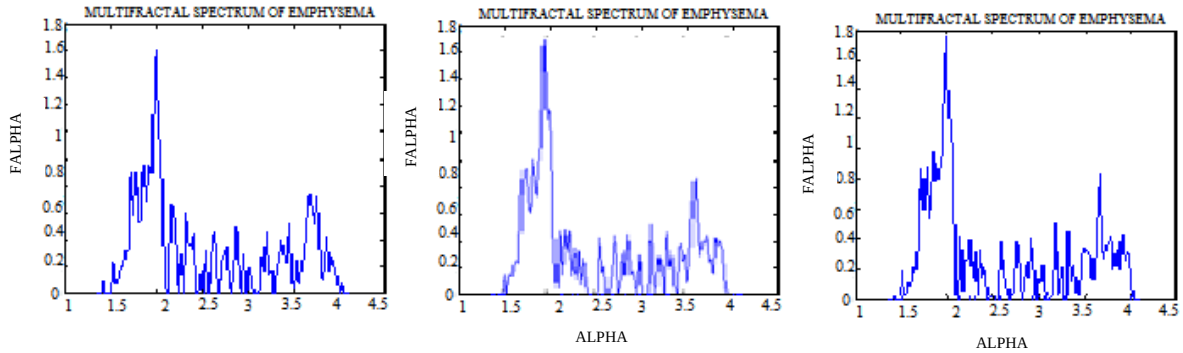

(a) Multi-fractal Spectra of the Normal regions

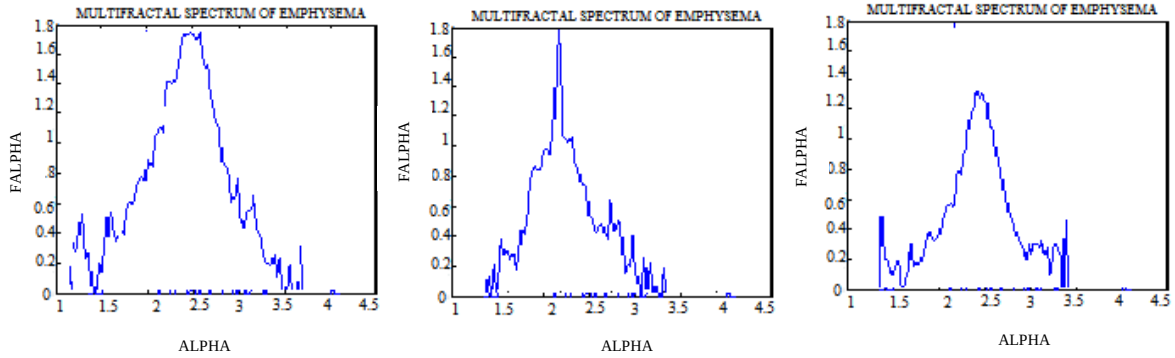

(b) Multi-fractal spectra of the emphysema regions.

Figure 5-13: Multifractal spectra of PSE sub-images.

The higher FD values or multi-spectra with larger height and width in some sub-images are due to the complexities of the tissue in that region due to the presence of emphysema pattern. We also note that the spectra of all sub-images without emphysema are exactly the same such that any deviation of a spectrum away from the normal spectrum would indicate the presence of emphysema pattern in that region. Distinct deviations are observed between the spectra of the normal image and those images with emphysema patterns in terms of the minimum and maximum values of local and global information ($\alpha, f(\alpha)$) as shown in Figure 5-13.

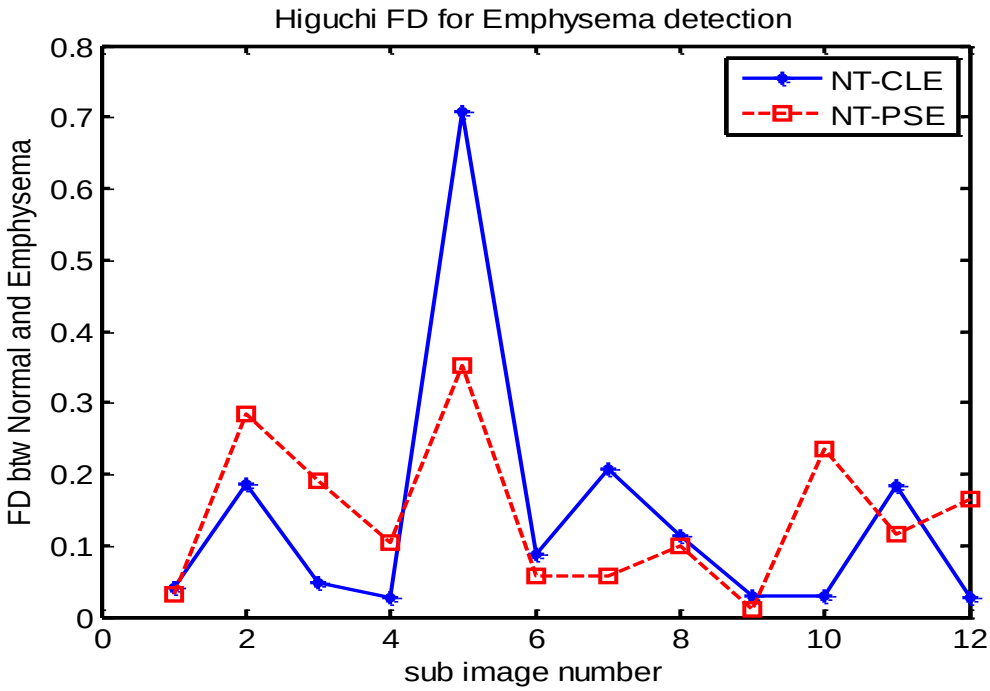

Figure 5-14: FDs differences between the NT and the pathological images.

In Figure 5-14, the spectra in the first row for the sub images are smaller than the spectra of the sub-images with the presence of emphysema. The Holder exponent alpha ranges from 1.5 to 2.1 ($\alpha_{max} - \alpha_{min}$) in the regions without emphysema while the alpha ranges from 1.4 to 2.7 ($\alpha_{max} - \alpha_{min}$) in the case of the regions with the detection of emphysema. It was observed that the values of the multi-spectra in the images with emphysema are generally larger than the values of the spectra with the images without emphysema; therefore, the Holder exponent alpha is an important parameter in the identification and detection of emphysema. This is in line with the results in Table 5-4 that uses Higuchi dimension for the computation of fractal dimension.

5.5 Classification Using Multifractal Descriptors

The implemented method according to the algorithm described in the previous section was applied to the CT images at the emphysema database (Sorensen et al., 2010) for classification and retrieving purposes. The classifier used the features derived from the averaged multifractal spectra of four randomly selected images belonging to each class. 30 images from each class are used as the training samples and the features of the calculated multifractal spectra of 18 images from each class as the test samples.

The results of the multifractal descriptors obtained for the three classes of the emphysema images using four multifractal intensity measures are shown in Figure 5-11. The three distance metrics used for the experiments include; the Manhattan, the Chi-square and the Bhattacharyya distance (Choi & Lee, 2003).

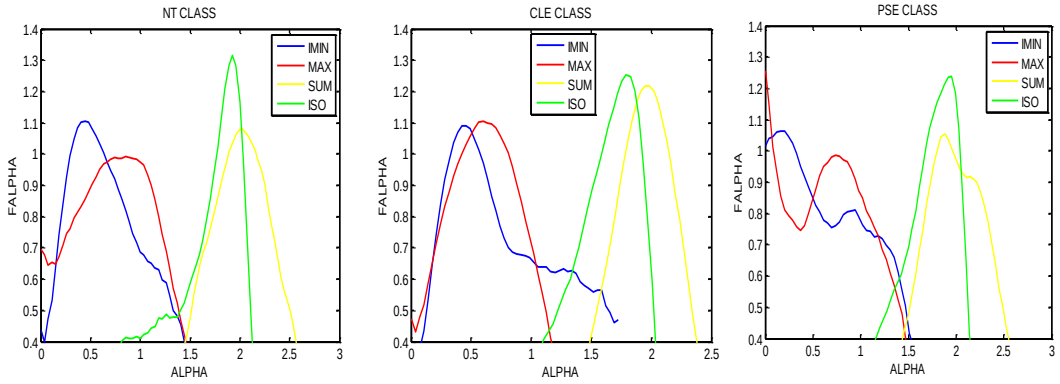

Figure 5-15: Multifractal descriptors for three classes of emphysema images using different intensity measures.

As can be seen in Figure 5-11, the physical appearance of the multifractal spectra can be used to differentiate the classes of emphysema images. Each class has different multifractal spectra represented by different intensity measures. The descriptors show how the multifractal spectrum of each emphysema class changes with the intensity measures. The geometrical characteristic properties of the spectra derived from the feature descriptors could be used for the classification of emphysema images. The experimental analyses are tested by comparing the extracted parameters from the multifractal spectra of the trained images with the features derived from the tested images in order to model the differences between the classes of emphysema images. The multifractal characteristic parameters of the spectra used for this experiment are: the minimum α values of the spectra, α_{min}, maximum α values of the spectra, α_{max}, maximum of the multifractal spectrum $f(\alpha)_{max}$ and the α which corresponds to $f(\alpha)_{max}$.

The performance of the classifiers is evaluated in the form of confusion matrix. A confusion matrix can be represented as a matrix $M \in R^{kxk}$, a square matrix whose diagonal elements represents the actual classification accuracy where k is the number of classes in the dataset. The classification error of the classifiers can be calculated as follows:

$$Error = 1 - \frac{trace(confusionMatrix)}{sum(confusionMatrix)} \quad (5.6)$$

where trace (.) is the sum of all the elements in the diagonal, and sum (.) is the sum of all the entries in the confusion matrix.

The *k*-NN is the first classification to be considered in this research work due to its simplicity and flexibility. The classification is done using the three distance metrics to measure the similarity between the images. The classification results in a form of confusion matrices using the selected measures are given in Table 5-5. The proposed approach performs well in terms of separating the normal lung CT tissues from other emphysema classes using the inverse-minimum intensity measure. However, the results generated for assessing the severity of emphysema in CT images using the multifractal approach are not good enough. Overall, the Bhattacharyya distance using all the intensity measures performs worse than other distance metrics while Manhattan distance gave the best overall classification results. Further improvement using the sum intensity measure and a cascaded set of classifiers is proposed later in Chapter 7.

		Predicted											
		Bhattacharya			Chi-Square			Manhattan			LBP		
Actual		NT	CL	PS	NT	CL	PS	NT	CL	PS	NT	CLE	PSE
	NT	18	0	0	18	0	0	18	0	0	16	0	2
	CL	10	8	0	9	9	0	7	11	0	1	17	0
	PS	3	8	7	3	5	10	3	5	10	1	1	16

Table 5-4: Comparison of classification results using different distance metrics and LBP.

The multifractal based classification results obtained (Table 5-4) are compared with the published LBP results. The LBP result used for comparison (Table 5-5) is taken from the joint LBP and the intensity histogram approach reported by Nava (2013). LBP is a powerful texture descriptor and is commonly used in medical image classification.

However, multifractal descriptors have not so far been used for emphysema classification, even though multifractal features also provide efficient texture descriptors (alpha-histogram and multifractal spectra) that are similar to the LBP histogram. The confusion matrices generated by the intensity measure clearly show that the LBP result slightly performs better than our results.

5.6 Implementation Aspects

There are several factors that must be taken into consideration in order to develop an efficient algorithm for the computation of a multifractal spectrum and to improve the classification accuracy. This section discusses some of those aspects as well as the selection of parameters used in the computation of the fractal dimension.

5.6.1 Processing of Edge Pixels

The processing of pixels very close to the edges (boundaries) of the emphysema CT image could pose problems as many of the windows used for computing the Holder exponent around the image edge may fall partially outside the image. This is a common problem in the area of image filtering where similar windows containing weights of convolution kernels are used. In image filtering, a set of standard solutions such as copying the boundary pixel values to cells outside the boundary (option 'replicate' in MATLAB), mirror reflecting the image across the border (option 'symmetric' in MATLAB), and assuming that the image is periodic along both *x* and *y* directions (option 'circular' in MATLAB) are used. However, these methods generate significant errors in the linear regression line and cause erroneous values of the Holder exponent. We therefore leave a margin of 5 pixels around each border of the image patches and process only those pixels where at least five surrounding windows are well within the image.

Another edge condition that needs to be taken care of is the boundary between the lung and thorax regions. Such boundaries may be present in an image patch. Here, we identify the pixels belonging to thorax using their high intensity values (see, Figure 5-2) and exclude window regions that contain such pixels, and process only those pixels with at least five surrounding windows that are well within the lung region.

5.6.2 Removal of Noise Regions from Spectrum

The regions of the multifractal spectrum where the fractal dimension (y-value) has a magnitude less than 0.2 essentially correspond to noise. The corresponding α values at both sides of the spectrum (Figure 5-16) need not be considered in the classification process. The resulting range of α-values [α_{mim},α_{max}] is divided into pre-specified α sub-intervals; selecting the appropriate number of α sub-interval may also determine the accuracy of the multifractal spectrum. Small size of α sub-interval will only allow a low frequency but produces a smooth spectrum with a small resolution, while too large a number of αsub-interval yields a spectrum with more details. Figure 5-16 illustrates the multifractal plots for the different numbers of α sub-interval.

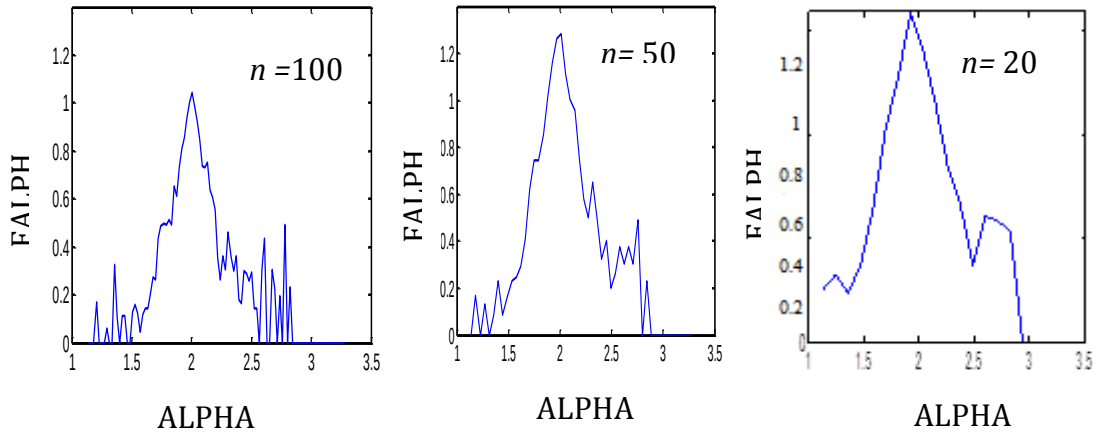

Figure 5-16: Illustrating multifractal spectra results for n = 100, n= 50 and n= 20.

In Figure 5-16, the spectrum with n = 100 gives more details of information that could be very useful for the classification process than the two other spectra. Though the multifractal spectrum with n = 50 is very smooth while the resolution of the spectrum with n = 20 is too small and this can lead to loss of useful information.

5.6.3 Selection of Box Size

The slope of the linear regression using the box counting method is used for the computation of the multifractal spectrum. A selection of small box sizes may lead to increase in the number of non-empty boxes while increasing the box sizes may reduce the number of non-empty boxes. According to (Vehel & Mignot, 1994b), using smaller boxes enabling high resolution of the estimated $f(\alpha)$ values but large box sizes may significantly reduce the resolution of the calculated $f(\alpha)$ values. As can be seen in

Figure 5-17, where the box size for the calculation of the Holder exponent α changed from *m* = 5 (11pixels) to *m* = 15 (31pixels). The multifractal spectra obtained differ in width and height.

The result presented in Figure 5-17 shows that the total number of boxes *m* used for the computation of the Holder exponent *α* may influence the accuracy of the multifractal spectrum. In this research work, 8 is used for the variable *m* and hence the size of the largest box is 17 pixels. The multifractal spectra generated in Figure 5-18 are centered around the same α value close to 2 but with different physical shapes.

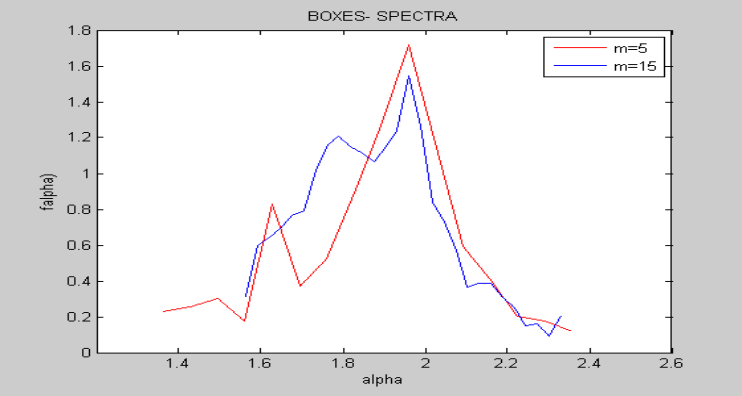

Figure 5-17: Illustrating the multifractal spectra plots for different box sizes.

Additionally, a certain threshold level can be set for *α*-values to adjust the limits of the alpha-histogram, such that any value below the threshold will be treated as noise and removed from the calculation. In this work, the threshold is set to 5, which is approximately 0.1% of the total number of pixels in a 61x61 size image.

5.6.4 Gamma Correction

The processing steps discussed in the previous section requires a mapping the range of *α*-values from the original range into a new range with a better contrast of α-images without affecting the multifractal spectrum. Alternatively, we could also map the intensity limits of the α-image automatically into a new range by using the contrast stretching. This process will automatically adjust the limits by trimming the extremes at both ends of the intensity range into a specified range limits. These limits can be specified as a fraction between 0 and 1 in the form of [low_in, high_in] vector. However,

the contrast adjustment may be non-linear, which may affect the accuracy of multifractal spectrum; we therefore introduced a gamma correction factor to map the α-image's intensity from low and high to values between bottom and top. The mapping is totally depending on the value of gamma since gamma can take any value between 0 and infinity. If gamma is 1, the mapping between the input and output images is linear, but if gamma is less than or greater than 1, the mapping is non-linear (Figure 5-18).

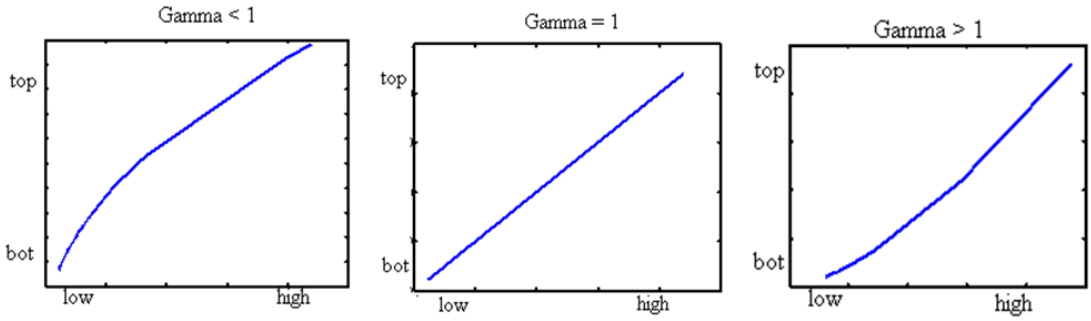

Figure 5-18: Three gamma correction settings for intensity transformation.

The alpha-histograms and the corresponding multifractal spectra of the normal emphysema image demonstrating the effect of gamma factor are presented in Figure 5-19.

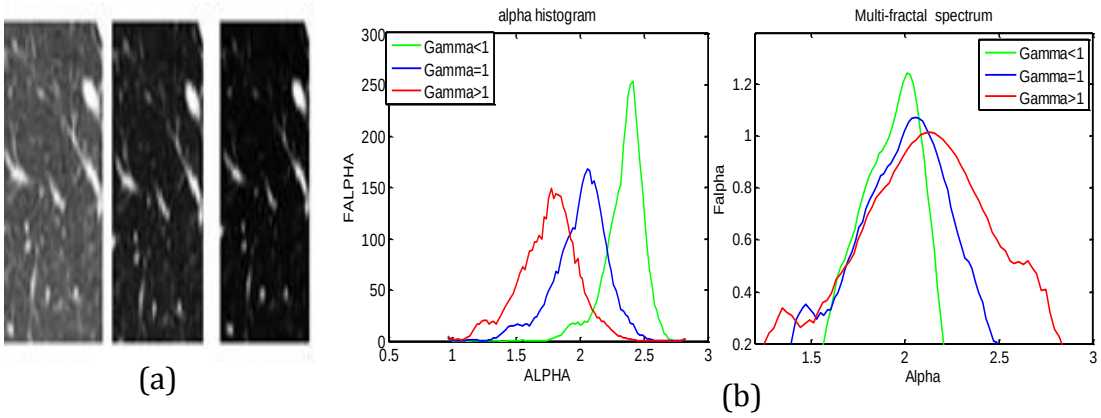

Figure 5-19: Effect of image intensity adjustment using gamma correction factor on α-histogram and multifractal spectra, and the corresponding output images. (a) Transformed images (b) Comparison of α-histogram and multifractal spectrum.

When Gamma is 1, the mapping is linear and does not affect the alpha-histogram and the multifractal spectra, but when Gamma is less than 1, the alpha-histogram shifted towards higher values of α, which slightly brightens the corresponding image. In addition, when Gamma is greater than 1, the alpha-histogram shifted towards the leftward position, causing the greater number of pixels to have low α values and hence darkens the output image.

5.7 Chapter Summary

This chapter has presented the details of multifractal analysis of HRCT emphysema images that form the basis of the research work reported in the thesis.

The multifractal spectrum of the emphysema images has been computed using four different intensity measures; the summation, Iso-surface, maximum and inverse minimum measures. The primary features extracted are the α-histogram and the multifractal spectrum. In addition to these features, we also considered the generalized Renyi spectrum and the Higuchi dimension. A detailed analysis of these features using ANOVA for ensuring that the selected features exhibit sufficient inter-class variance required for classification was presented. We then presented a multifractal based emphysema classification algorithm using a k-NN classifier, and compared the results with those obtained using the local binary pattern (LBP). Finally, a few important implementation aspects such as the processing of edge pixels, removal of noise regions from the α-histogram, selection of the box size for computing fractal dimension and gamma correction were discussed.

6 FEATURE SELECTION METHODS

This chapter aims at improving the classification accuracy of the emphysema patterns in CT images by combining the features from the multifractal descriptors and the alpha-histograms in the form of a hybrid set of features. Furthermore, the thesis also employs the feature selection (FS) technique for the extraction of the important features that would increase their discriminating capability, reduce the high dimensionality of datasets, and yield better classification accuracy. Related works on FS and a literature review of the Naïve Bayes (NB) and the bagged decision tree (BT) classifiers were previously given in Chapter 4. Section 6.2 discusses the process of the FS techniques in finding the optimal features. Sections 6.3and 6.4 present different experimental approaches, results and comparative analyses. Section 6.5 gives a summary of the work presented in this chapter and outlines some possible future extensions.

6.1 Introduction

Selecting the relevant subset features for developing a classification system is a challenging problem in the field of machine learning. In order to achieve the optimum performance from a particular classifier on a certain dataset, the chosen FS approach must establish the relationship between the classifier algorithm and the training set. In this section, a novel approach for improving the accuracy of emphysema image

classification is proposed. It uses the FS techniques to search for the relevant features that would have the greatest influence on the prediction accuracy.

Different experimental approaches are investigated on the datasets derived from the multifractal descriptors using the NB and BT algorithms. The performances of the classifiers are compared based on the feature variables selected by the proposed approach and the effects of some important parameters on the overall classification accuracy are analysed.

In machine learning, most classifier algorithms are presented with a set of training instances, where each instance, can be described as a feature vector or attribute values and a class label. The first task is the selection of the appropriate classification algorithm that could be useful in classifying the feature sets. The classifier maps the space of feature values to the set of class values to formulate a predictive model (Han, Park, & Lee, 2011; D. Wang, Nie, & Huang, 2015). The problem of the feature subset selection (FSS) in image classification is very challenging as there is need to select some important subset features upon which the algorithm can focus on. Selection of bad subsets features might eventually affect the performance accuracy of the classification system.

The datasets used for the experiments are obtained from the multifractal and the alpha-histograms descriptors using the summation intensity measures for the Holder exponent computation. The multifractal data sets are generated by dividing the range of Holder exponents $[\alpha_{min}, \alpha_{max}]$ of the emphysema image into 100 intervals and the corresponding fractal dimension $\{f(\alpha_i)/\ i = 0,1, \dots 99\}$of each alpha-image is calculated with the α values ranges $[\alpha_i\ \alpha_{i+1}]$. values for each emphysema class are used as the feature vectors for the multifractal datasets using the summation measure. Similarly, the corresponding pixels count with the alpha values within the range $[\alpha_i\ \alpha_{i+1}]$give the alpha-histogram (see Section 6.2.2 below).Removing the noisy outliers, only 50 feature values are used for the experiments. As previously mentioned in Section 5.3.2, 30 images were randomly selected from each emphysema class for the training of the classification system while 18 images from each class were used for testing the accuracy of the system. The data set generated from the images consists of 90 rows of observations and 50 columns of features, thus the dimensionality of the data is 90 x 50. The target variables/labels can have one of the three values 0:NT, 1:CLE, 2:PSE.

The presence of too many feature variables may sometimes reduce the accuracy of the classification system as some features may be redundant and non-informative. In addition, processing a high dimensional data requires large memory and may reduce the computational speed. In this section, we explore methods to select the most relevant features from the computed set of multifractal spectra and alpha histogram values.

6.2 Histogram Features

There are various types of features that can be extracted from the CT emphysema images for the multifractal analysis of emphysema patterns. In order to obtain feature descriptors with a very high discriminating power, this section considers the combinations of some of the important histogram features and the multifractal spectrum features for efficient classification of the emphysema patterns. The first histogram features are derived from the intensity histogram.

6.2.1 Intensity Histogram of Emphysema Image

An intensity histogram is a diagram in the form of a graph, plotting the number of pixels with a specific gray level versus the gray level value. The shape of the histogram broadly describes the intensity distributions in the image. In some cases, a histogram may be scaled for adjusting the intensity levels or the contrast (e.g. histogram equalization). An example illustrating the intensity histogram of an emphysema CT image is presented in Figure 6-1.

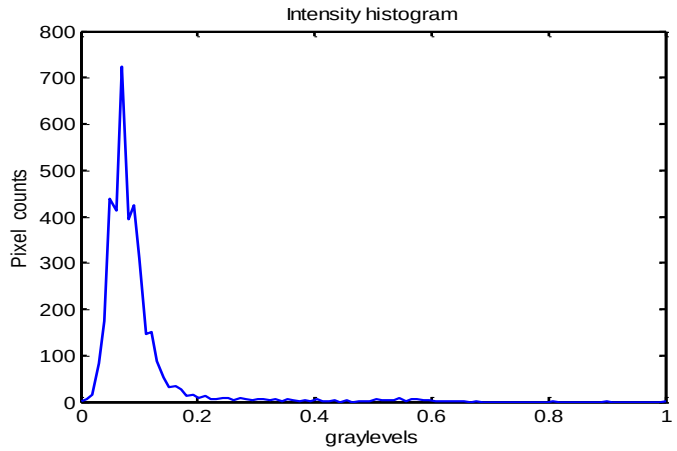

Figure 6-1: Example of intensity histogram of emphysema image.

The useful features that can be derived from the intensity histogram are the minimum and maximum values on the x-axis, and the maximum of the histogram on the y-axis.

6.2.2 Alpha-histogram of Emphysema Image

The detailed discussion of the alpha-histogram was given in chapter 4. An α image is a matrix of the same dimension *M x N* as the original image but filled with α-values, with one-one correspondence to image pixels. An alpha-histogram of an image is therefore constructed using the $\alpha(m, n)$ values (m=1..M, n=1..N) of the image. As an example, an alpha-histogram of an emphysema image class is presented in Figure 6-2. Alpha-histogram can also be used as a global descriptor of intensity variations, just like the intensity histogram.

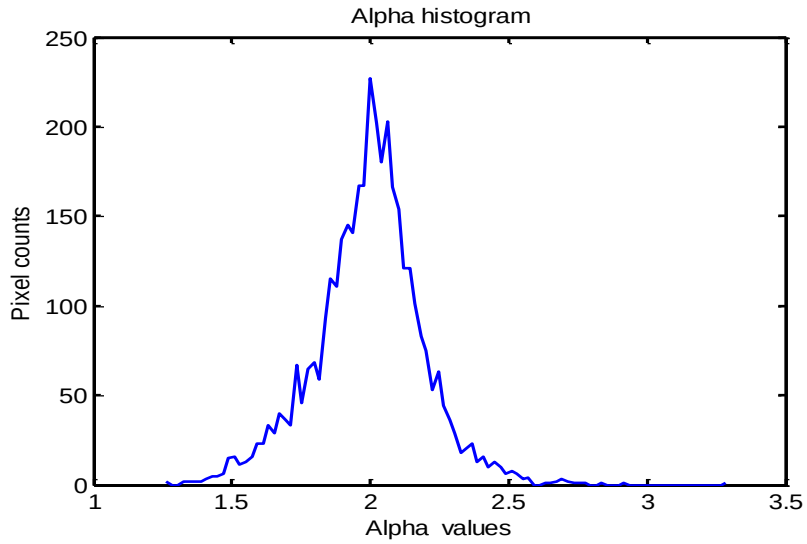

Figure 6-2: Illustrating an example of alpha-histogram of emphysema image.

The features derived from the alpha-histogram would also provide some local characteristics of the images. However, multifractal spectrum provides several shapes that could give more useful information to describe the texture characteristic properties of the images than the alpha-histogram.

Multifractal spectrum contains additional global information derived from the local intensity distributions of the image at various scales to provide a global descriptor of the images. It generally has a higher discriminating power compared to intensity and the alpha-histograms. Furthermore, it can also be observed from the analyses that the combination of the features extracted from the histograms and the multifractal

spectrum could generate a descriptor with a better discriminating power. The multifractal spectrum of the same emphysema image used in Figure 6-2 is presented in Figure 6-3.

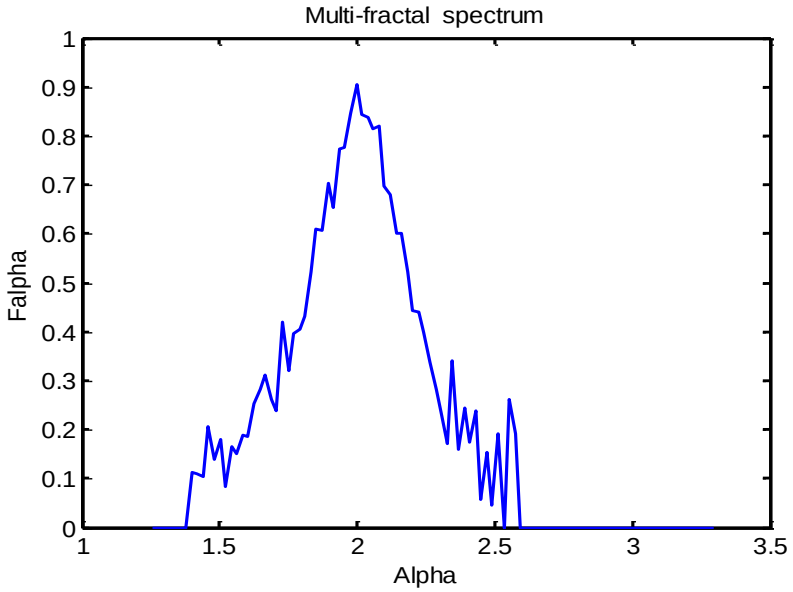

Figure 6-3: Multifractal spectrum of an emphysema image sample.

There is the possibility of improving the classification accuracy of the emphysema images by cascading the results obtained from the alpha-histogram with the multifractal spectrum since the new descriptor will definitely provide solutions to some of the limitations of the alpha-histograms and the multifractal spectrum. The newly constructed features would possess the characteristic features of the multifractal spectra and that of the histograms, which makes it more superior and discriminating for efficient and accurate classification. There are some features that are very useful in a multifractal spectrum but are lacking in the histograms and vice versa.

6.3 Feature Selection Methods

In order to improve the classification accuracy of the CT image, the Naïve Bayes and Bagged decision trees are considered at this stage since they are both known to perform well especially with high dimensional data sets like the multifractal and alpha-histogram.

The system overview for the classification approach involving several stages is presented in Figure 6-4. The features extracted from the descriptors are used as the input features for the FS algorithm. The details of the FS algorithm are discussed in

section 6-4. The two popular classifiers used in this study are trained on the outputs obtained from the FS as presented in Figure 6-4.

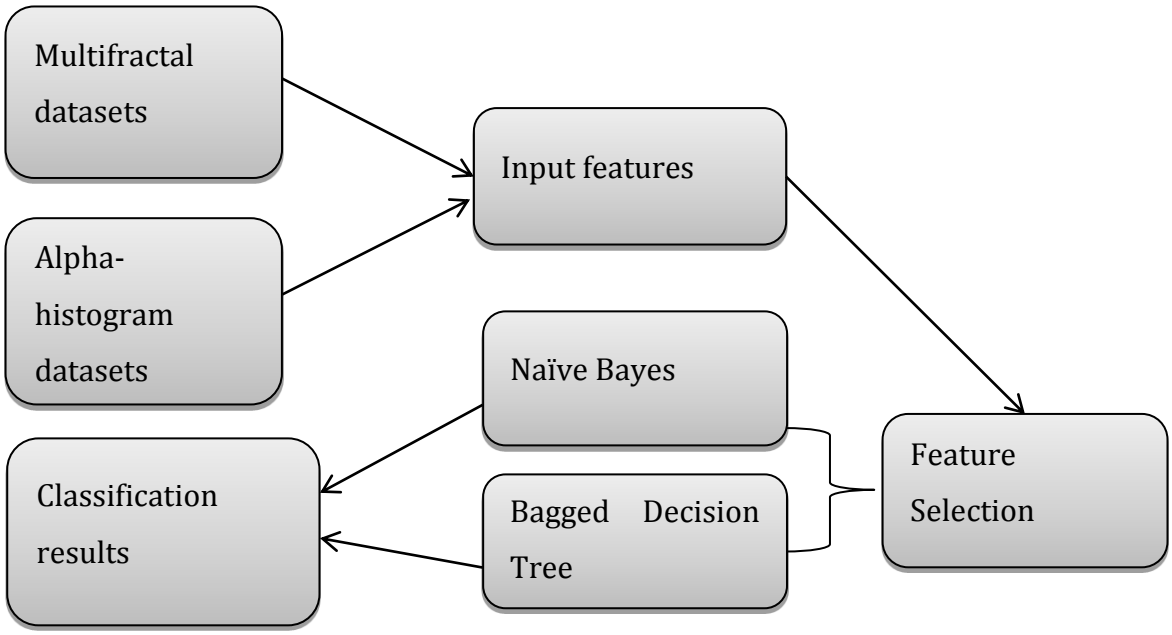

Figure 6-4: System overview of classification approach in emphysema images.

Feature selection is an important part of pre-processing data as irrelevant or redundant features in a data set can make the training phase more difficult and time consuming. This is done by reducing the dimensions of data and thereby making the classifier algorithms to operate faster (Randen & Husoy, 1999). Feature Subset Selection (FSS) is a mapping from a*m*-dimensional feature space (input space) to *n*-dimensional feature space (output), which can be represented as follows:

$$Fss: R^{rXm} \rightarrow R^{rXn}, \qquad (6\text{-}1)$$

where $m \geq n$, R^{rXm} is the matrix of the original data set with *r* instances or observations, R^{rXn} is the reduced feature set containing *r* observations in the subset selection. It is also a technique of selecting only the predictor variables, that provide the best predictive power by simplifying and improving the model interpretation.

The principal component analysis (PCA) is one of the methods that can be used for selecting features and reducing dimensionality (Domingos, 1997; Papadopoulos, 2005; D. Wang, 2015). In PCA, the data set is represented by a small number of uncorrelated features while retaining most of its information content. This can be done by removing correlated components that contribute only a small amount to the total variance in the data set. The methods of selecting relevant features using certain discriminating criteria could sometimes be achieved by the correlation coefficients like statistical tests such as t-test, F-test etc. (Kohavi & John, 2011). In (Ladha, 2011), the author proposed a minimum redundancy-maximum relevance criteria for FS and the results significantly improved the predictive power and generalization properties of the feature sets.

Sequential forward selection (SFS) is used in this study to search for the relevant features that could yield optimum classification accuracy and increase the computational efficiency. SFS is one of the methods of selecting a subset of features in a data set by sequentially selecting the features until there is no further improvement in prediction accuracy. The important stages of the SFS algorithm are shown in Figure 6-5.

Most selection search approaches iteratively evaluate a subset of features, then modifies the subset and evaluates if the new subset is an improvement over the previous. Evaluation of the subsets requires a scoring metric that grades a subset of features. In this study, a function handle is used to define a criterion to determine the relevant features to be selected. Dimensionality reduction is achieved by calculating an optimal subset of predictive features of the original data. The algorithm automatically stops when further selection of feature subset has no effect on the classification errors.

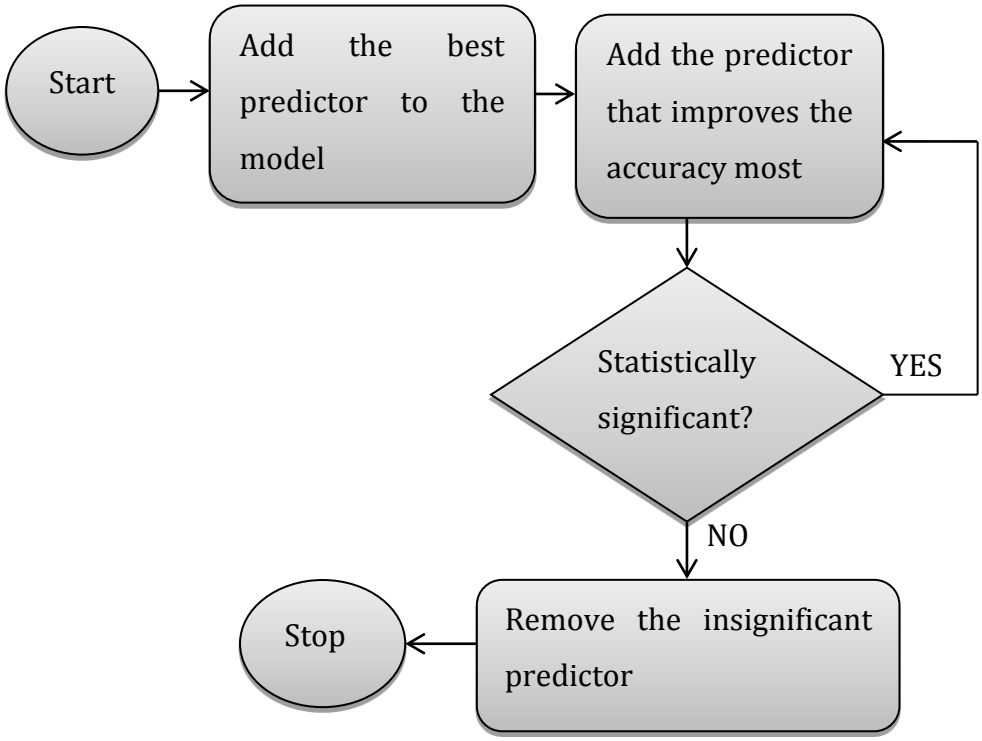

Figure 6-5: Sequential forward selection method.

6.4 Results and Discussion

In this section, we outline experimental results obtained using images from the emphysema database (Ruiz & Nasuto, 2005), based on the implementation of the methods discussed in the previous sections. The feature vectors extracted from the multifractal spectra and the alpha-histograms are used for classification and retrieving purposes. The histogram descriptors used for the classification experiment are constructed by dividing the range of α-values generated from the Holder exponent into 100 intervals as described in section 6.1. The alpha-histogram is calculated for each alpha bin as the number of pixel counts with the α values within the α-range $[\alpha_i\ \alpha_{i+1}]$. The average of the alpha-histogram for four randomly selected images is calculated and the feature vectors obtained from the descriptors are trained with the classifier algorithms. In the classification process of the NB classifier, we applied the holdout partition method to divide the observations into training sets and test sets.

There is a scalar specifying the proportion of the number of observations to be randomly selected for validation. In order to achieve promising results since the

accuracy of the classifiers depends on the training data, we consider 70 percent of the feature vectors for the training and 30 percent for cross-validation. The performance of the classifiers is evaluated in the form of confusion matrix. A confusion matrix can be represented as a matrix $M \in R^{kXk}$, a square matrix whose diagonal elements represents the actual classification accuracy where k is the number of classes in the data set. The classification error of the classifiers can be calculated as follows:

$$\text{Error} = 1 - \frac{\text{trace(ConfusionMatrix)}}{\text{sum(ConfusionMatrix)}}, \qquad (6\text{-}2)$$

where trace (.) is the sum of all the elements in the diagonal, and sum (.) is the sum of all the entries in the confusion matrix. The feature vectors from the data sets are also trained with the BT classifier and the performances of the classification algorithms are examined with different experimental settings. We consider a dimensionality reduction step due to the presence of large irrelevant features in the data sets. The classification results obtained before and after the feature reduction for the NB classifier are presented in Table 6-1 in the form of confusion matrices.

The feature techniques reduced the feature variables in each data set to a set of feature variables with the highest discriminating power, such that the classifiers are trained with the newly selected features by the SFS method. The performance of the classification system is measured by the classification accuracy generated by the confusion matrices.

The results obtained by the SFS achieve better dimensionality reductions and increase in learning accuracy by simplifying the model complexity. In Table 6-1, the classification accuracy of the multifractal datasets using the NB algorithm, increases from 74.3% before the FS to 77.6% after the FS and in alpha-histogram datasets, the accuracy increases from 74.6% before the FS to 80.3% after the FS. The reasons why the alpha histogram features give better results in this case could be associated with the eliminations of redundant features by the SFS in the alpha histogram data sets. The SFS algorithm performed better in the alpha histogram data set than that of multifractal data set. However, in most cases the multifractal features are more flexible than the alpha histogram features in terms of extracting the useful features that can be used to identify different locations within digital images.

The summary of the classification results produced by the BT algorithm before and after the FS is shown in Table 6-2. The performance of the BT algorithm after the FS in the multifractal data set is slightly better than the results obtained in the alpha-histograms dataset.

	Predicted												
Actual	Multifractal features							Alpha-histogram features					
	NB without SFS				NB with SFS			NB without SFS			NB with SFS		
		NT	CLE	PSE	NT	CLE	PSE	NT	CLE	PSE	NT	CLE	PSE
	NT	13	3	2	13	3	2	16	0	2	16	2	0
	CLE	4	14	0	3	13	2	5	10	3	2	13	3
	PSE	2	4	12	2	2	14	3	2	13	5	0	13

Table 6-1: Naïve Bayes (NB) classification results with and without feature reductions.

Furthermore, the BT classifier outperformed the NB in multifractal datasets before and after the FS techniques, but the overall classification remains the same after the FS in the alpha-histogram data set. However, the performance of the classifier is slightly higher than the NB before the FS in the alpha-histogram datasets.

	Predicted												
Actual	Multifractal datasets							Alpha-histograms datasets					
	BT without SFS				BT with SFS			BT without SFS			BT with SFS		
		NT	CLE	PSE	NT	CLE	PSE	NT	CLE	PSE	NT	CLE	PSE
	NT	14	2	2	16	0	2	15	3	0	16	2	0
	CLE	2	13	3	4	12	2	0	14	4	0	14	4
	PSE	0	3	15	2	0	16	0	4	14	3	2	13

Table 6-2: Bagged decision tree classification results with and without feature reductions.

The reason for the improvement in the performance of the algorithms after the FS in the data sets is the reduction in the complexity of the models, as complex models sometimes overfit the data and generate additional errors. Simplifying the complex models that would include the feature variables that are uncorrelated with one another would always reduce the computational complexity, which might increase the accuracy. The difference in classification accuracy between the NB classifier and the BT over the multifractal datasets is 5.7% after the FS, while in alpha-histogram datasets, the overall classification remains the same after the FS but slightly higher before the FS (Tables 6-1 and 6-2).

The second approach is the concatenation of the relevant features obtained from the multifractal datasets and the alpha-histograms descriptors to generate new feature vectors. This is very easy since they both have the same number of rows and columns in dimension. Only the features selected by the FS technique are used and the experimental results are presented in Table 6-3.The improvement between Table 6-2 and Table 6-3 is that the overall classification accuracy increased from 80.3% in Table 6-2 over the alpha-histograms datasets to 88.7% in Table 6-3 over the combined features with the BT classifier. However, the performance of the BT classifier in Table 6-2 over the multifractal datasets is slightly better than the NB classifier in Table 6-3 over the combined features with the difference in classification accuracy of 0.3% after FS.

	Predicted											
Actual	Naïve Bayes Algorithm							Bagged Decision Tree Algorithm				
	CF without SFS				CF with SFS			CF without SFS			CF with SFS	
		NT	CLE	PSE	NT	CLE	PSE	NT	CLE	PSE	NT	CLE	PSE
	NT	15	3	0	16	2	0	16	0	2	14	2	2
	CLE	3	12	3	0	15	3	0	16	2	2	16	0
	PSE	3	2	13	3	2	13	2	3	13	0	2	16

Table 6-3: Classification results with and without feature selections for combined features.

The results in Table 6-3 reveal that this approach outperformed the results obtained in Tables 6-1 and 6-2. Significant improvements over the combined features set for the

two classifier algorithms are achieved after the FS. Compared with the results in Tables 6-1 and 6-2, the difference in classification accuracy between the combined feature sets and the alpha-histograms datasets (Table 6-1) for the NB classifier is about 3%, while the accuracy over the multifractal datasets for the BT also increased by 5.3% after the FS. Also in Table 6-3, the classification results of the combined features using the NB algorithm completely classified the normal emphysema images from the other pathological cases (CLE and PSE).

The reasons for this improvement is due to the combination of the important feature variables with high discriminative power from both datasets since the irrelevant features have been filtered out by the FS methods. However, this approach consumes more processing time as the size of the dataset increases and thus reduces the computational speed. Furthermore, the pairwise t-test of the classification results before and after the feature selection were carried out in order to determine whether the differences in accuracy are statistically significant or not. The t-test results of the classification results of the combined features in Table 6-3 are shown in equation (6-3); $h = 0$ indicates a failure to reject the null hypothesis.

$$h = 0,\ \text{p-value} = 0.7165,\ \text{ci} = -27.0733 \quad 20.4067 \tag{6-3}$$

This means the improvement achieved in the classification results is not statistically significant even at the 5% significance level. The same procedures were repeated for the previous results in Tables 6-1 and 6-2 before and after the feature selection in the multifractal and alpha-histogram data sets; the statistical results showed that the increase in the classification accuracy is not statistically significant since it failed to reject the null hypothesis at the 5% significance level. Another evidence to prove the statistical results is that the probability of observing a value of the test statistic, as indicated by the p values, is far greater than the α (significance level). Additionally, the 95% confidence interval on the mean of the difference does contain zero in all the results as can be seen in equation (6-3). These are enough reasons to conclude that none of the classification results presented in this section is statistically significant at the $\alpha = 0.05$ significance level.

An important parameter that can be used to evaluate the performance of the BT algorithm is the number of grown trees used in constructing the classification model. For the multifractal datasets, it can be observed in Figure 6-6 that, the BT performed well when the number of grown trees ranges from 37 to 49.In addition, the classification errors are at the minimum level and constantly stable (Figure 6-6). The performances of the algorithm are not stable when the grown trees are less than 37 and hence generating more classification errors. However, for the alpha-histogram dataset (Figure 6-6b), the errors seem to be constant when the number of grown trees ranges from 20 to 40, and the performance of the algorithm is consistent. In order to fully optimize the performance of the classifier, the number of grown trees used for both datasets is therefore 40.

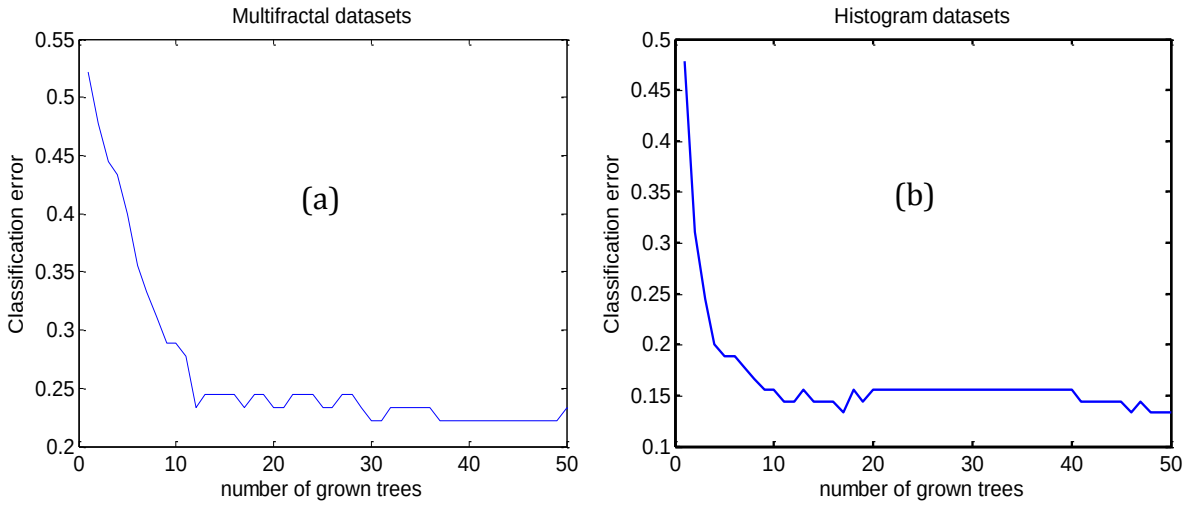

Figure 6-6: Illustrating the variations between the classification error and the grown trees for bagged decision. (a) Multifractal datasets (b) Alpha-histogram datasets.

Ensemble of decision trees, particularly the BT is a way of estimating the predictor importance. Measure of importance for each predictor variable can be achieved by evaluating the effect on the classification margin if the values of the variable are permuted across the out-of-bag observations. In other words, permuting a particular feature variable may either increase or decrease the classification accuracy. Figure 6-7 presents the results of the feature importance variables for the BT in each dataset.

In the experiments, a threshold was set to filter out those features whose ranking values are less than the required value; the features with the ranking values above this

threshold value are used for the classification process (Figure 6-7). In this case, the threshold is set to 0.42; the same principle used in section 5.5.2 is applied to set the threshold value and remove the unwanted features that could reduce the classification accuracy. The experimental results after removing the features below the threshold level as in Figure 6-7 reflect that the chosen features have greater predictive power than all features as the classification accuracy further increased.

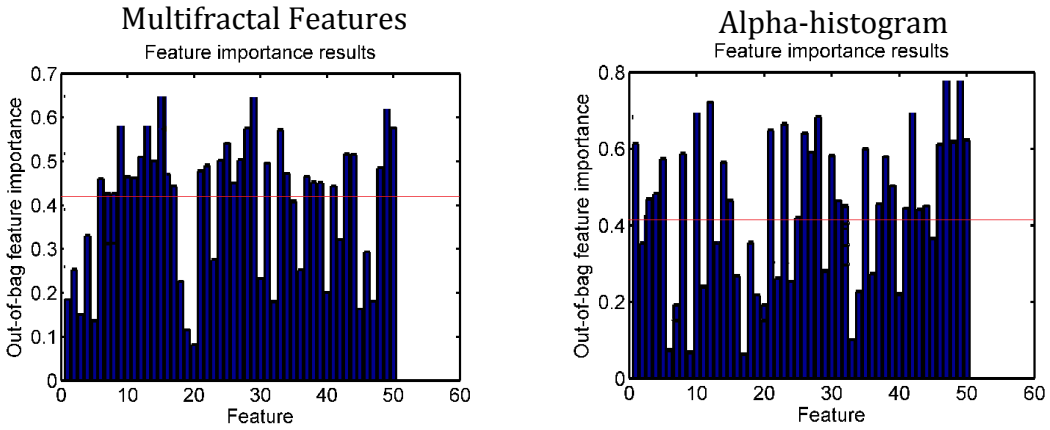

Figure 6-7: Showing the ranking values of each feature variable in the datasets.

This improvement in the classification accuracy indicates that many features in the datasets are highly correlated and many are not strongly relevant. The FS ignored this set of data and only trained with the important features that would have significant impact on the overall accuracy. The performances of different threshold levels are tested on the overall classification accuracies. It was verified experimentally that the larger the threshold value the more important the selected predictor variables. For instance, the threshold value of 0.42 over the combined feature sets gives the highest classification accuracy while the threshold value below this level reduces the classification accuracy. The reason is because, the smaller threshold values would allow more predictor variables that are not strongly relevant to be added to the selected variables trained with the classifier algorithms. This will eventually translate to a more complex model that could generate more classification errors and thus reduces the classification accuracy. However, further increase in the threshold values beyond 0.42 does not have any significant improvement in the accuracy. The plot of the test accuracy

demonstrating the effect of the threshold level on the overall classification accuracy is presented in Figure 6-8.

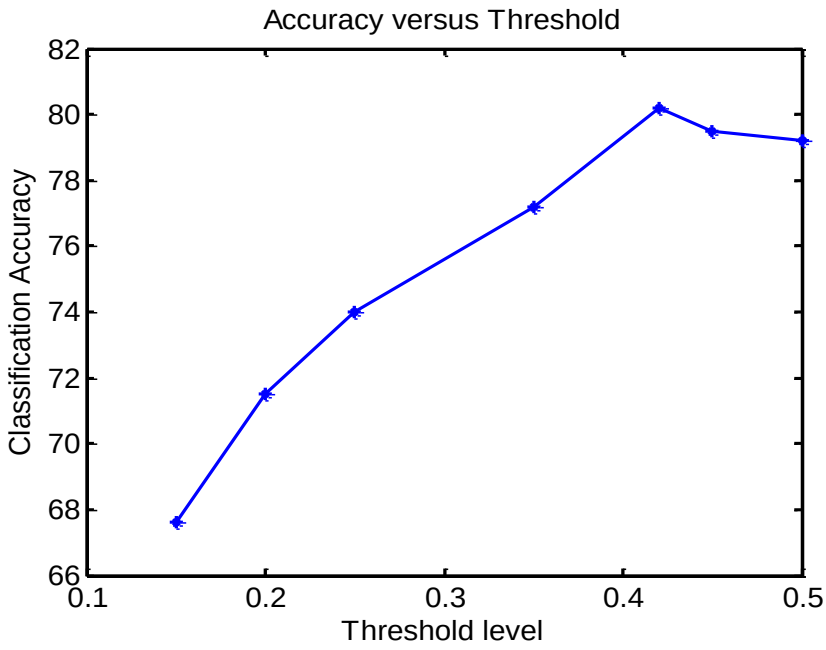

Figure 6-8: A graph of classification accuracy versus threshold level. Changes in the threshold level increase the accuracy until the peak value.

6.5 Conclusions

This chapter has presented a novel approach for improving the classification accuracy of emphysema images by employing the FS techniques. The FS approach has been implemented to remove irrelevant features. The two machine learning algorithms considered in this study; the NB and the BT performed well on the datasets used. The results achieved by the classifiers are compared, the performance of the BT is slightly better than the NB algorithms.

The experimental results also confirmed that multifractal descriptors could be used for the analysis and classification of emphysema in CT images. The information from the alpha-histogram descriptors is also very useful as the combination of the relevant features in the form of hybrid of both descriptors improved the classification accuracy. During the implementation of the BT, we presented some of the important parameters that could be used to evaluate the performance of the classification system.

The experimental results proved that the number of growing trees and the threshold values could affect the classification accuracy. Overall, the performance of the classifiers

after FS has been consistently higher than the results without FS. Further research work might be to cascade the two classifier algorithms together over the combined feature sets or other medical data sets. We would be looking at this cascading technique in details in chapter seven of this thesis. Other classification approaches such as the local binary patterns (LBP) would also be implemented for further analysis of the emphysema images, and the results will be evaluated against the multifractal methods.

7 CASCADED CLASSIFIERS

7.1 Introduction

This chapter proposes to improve the classification results previously presented in Chapter 5; by investigating further the features formed using a combination of the alpha-histograms and the multifractal descriptors in the classification of emphysema in CT images. It has been noted that the combined features obtained after the combination of the alpha-histograms and the multifractal descriptors in Chapter 5 separated the normal CT from the pathological cases, we therefore propose to apply the alpha-histogram for the classification of the CLE and PSE images, and cascaded the results with the results obtained from the multifractal descriptors.

The second approach uses the area under the ROC curves to identify the best features that could yield maximum classification accuracy and high computational efficiency. This is achieved in such a way that the performances of the classifiers are measured by using the classification accuracy (error matrix) and the area under the ROC curve (AUC). The work outlined in this section also aims at cover some of the important research goals. The AUC could be used to extract the important features that would increase the classification accuracy. Outline of several stages of algorithms for the development of alpha-histograms and multifractal spectrum, and how the combinations of the descriptors influence the overall accuracy of the images.

It has been observed in the literature (Chapter 4) that the accuracy and the AUC values of the best classifier could be further increased by cascading the classifiers for the

classification of malignant and benign lesions. Therefore, the main goal in this chapter is to cascade the classification methods using the alpha-histograms and the multifractal descriptors in order to obtain higher classification accuracy.

7.2 Cascaded Method for Emphysema Classification

The feature vectors extracted from the calculated multifractal spectra and the alpha-histograms are used for classification and retrieving purposes. The results of the multifractal descriptors obtained for the three classes of the emphysema images using four multifractal intensity measures were presented in chapter 5.

The histogram descriptors used for the classification experiments are constructed by dividing the range of α-values generated from the Holder exponent into 100 intervals. The alpha-histogram is calculated for each alpha bin as the number of pixel counts with the α-values within the α-range $[\alpha_i\ \alpha_{i+1}]$. The average of the alpha-histogram for four randomly selected images is calculated and the feature vectors obtained from the descriptors are trained with the classifier algorithm. The alpha-histograms for each emphysema class using the summation intensity measure for the computation of the Holder exponent are given in Figure 7-1.

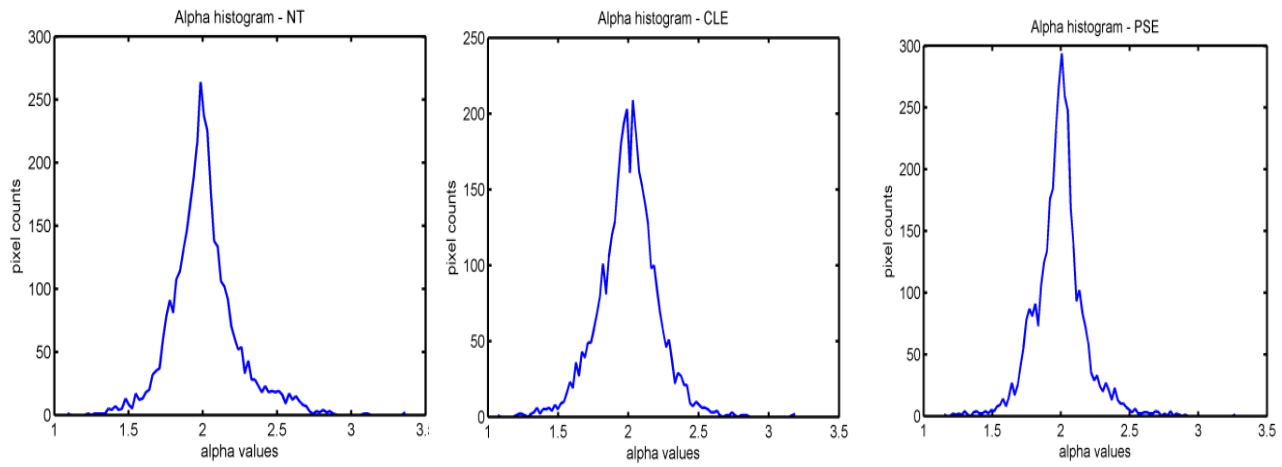

Figure 7-1: Alpha-histograms of each class of emphysema image using the summation measure

The summary of the cascaded procedures are presented in Figure 7-2, where the multifractal descriptors are used for the first classification and the alpha-histogram for the second classification stage. Both stages are combined together to produce the classification results as given in Figure 7-2.

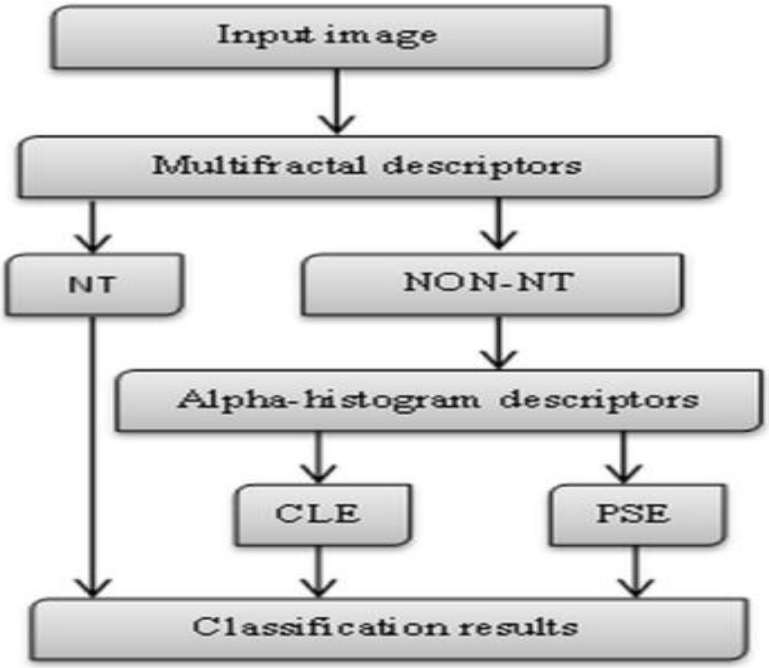

Figure 7-2: Outline of the cascaded algorithm used for classification.

7.3 Experimental Results and Discussion

In this section, we outline experimental results obtained using images from the emphysema database, Sorensen (2010) based on the implementation of the methods discussed in the previous section. The first stage of the classification uses the inverse minimum intensity measure for emphysema classification with Manhattan distance metric as previously discussed in Section 5.5. The inv-minimum measure was chosen since it was found to be very effective in tissue image classification (Mukundan & Hemsley, 2010). The summary of the classification results is shown in Table 7-1.

		Predicted		
Actual		NT	CLE	PSE
	NT	18	0	0
	CLE	7	11	0
	PSE	3	5	10

Table 7-1: Classification results using the inv-min measure.

As outlined in Section 5.5, the results show significant classification errors for the emphysema classes. The normal tissues were accurately classified, but some of the patches belonging to the CLE and PSE classes were also misclassified as normal tissues.
In the second stage of the classification, the normal emphysema class is removed, and the alpha-histogram descriptor is applied for further classification on the linear data sets with two pathological classes (CLE and PSE) as shown in Fig. 7.2. The classification results obtained using the BT classifier over the alpha-histograms datasets are presented in Table 7-2.

Predicted			
Actual	Alpha-histograms descriptors		
		CLE	PSE
	CLE	10	1
	PSE	1	14

Table 7-2: Classification results for the two pathological classes.

The results presented in Table 7-2 show good performance but with few errors. The next stage of the experiment would be to cascade this current result with the previous results obtained from the multifractal descriptors (Table 7-3).

Predicted				
	Final Classification outputs			
Actual		NT	CLE	PSE
	NT	18	0	0
	CLE	7	10	1
	PSE	3	1	14

Table 7-3: Classification results after combining the results from the two stages.

We did a detailed analysis of the results from the first stage to identify the source of the classification error. It was found that the features with inv-minimum distance measure did not have sufficient inter-class variance, particularly between the NT and CLE classes.

This can also be seen clearly in Fig. 5.15. Using the sum measure, the results showed significant improvement as given in Table 7-4.

First Stage					**Combined**		
	Predicted				Predicted		
Actual		NT	CLE	PSE	NT	CLE	PSE
	NT	18	0	0	18	0	0
	CLE	1	16	1	1	16	1
	PSE	0	2	16	0	1	17

Table 7-4: Improvement in classification results for the cascaded classifiers using the sum measure.

The final classification outputs are presented in Table 7-4 with an overall classification accuracy of 92.59%. The proposed approach where two classifiers are cascaded together gives a slightly better accuracy than a single classifier. The accuracy of the first stage is 90.7%, and with the addition of the second stage, a slight improvement in accuracy to 92.59% was observed.

The performances of the descriptors obtained from the alpha-histograms and the multifractal are also evaluated using the weighted area under the ROC curves. The area under the ROC curve is calculated for all possible combinations of the emphysema class labels over the data sets derived from the hybrid combination of the alpha-histogram and the multifractal descriptors by using the Wilcoxon rank sum test. Figure 7-3 presented the ROC curves for the selected features of the data sets and the corresponding class comparison of the AUC are given in Table 7-5.

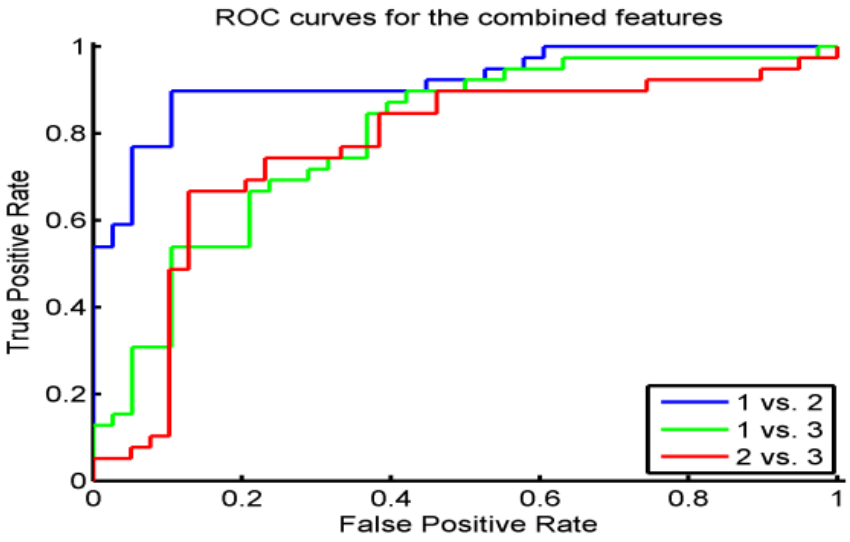

Figure 7-3: ROC curves of the combined features from the alpha-histograms and the Multifractal datasets using the best features.

The average of the AUC for the possible class pair is calculated for each column and the column with the maximum AUC's value is chosen as the best feature (Table 7-4).The Table 7-5 is generated from the pairwise class comparison results presented in Table 7-4 by adding the AUCs of the NT versus CLE and the NT versus PSE classes to produce NT versus other cases as indicated in Table 7-5. The closer the AUC's values to 1, the better the performance of the data sets. It can be noted from the outcomes in Table 7-5 that the performances of the NT class versus other classes (CLE &PSE) are better than the CLE class versus PSE class using the selected best features. This is also demonstrated in Figure 7-3; the ROC curves of the NT class versus the CLE class are more separated than the ROC curve for the CLE class versus PSE class. The mean AUC of 0.8251, obtained by averaging all of the pairwise values in Table 7-5 is used for the selection of the best features.

Class comparison	**NT vs. CLE**	**NT vs. PSE**	**CLE vs. PSE**	**Mean AUC**
Best Features	0.9204	0.7915	0.7633	0.8251

Table 7-5: Pairwise AUCs for emphysema classes.

The result in Table 7-5 is then compared with another paper by Sorensen and Nielson (Sorensen, Nielsen, & Lo, 2012). In Ref. (Vidakovic, 2013), the ROI classification for discriminating the emphysema with and without COPD is calculated using the *k* nearest neighbour approach and the AUC of 0.713 is achieved. In comparison with our results, the AUC value of 0.8559 obtained is by far better than the 0.713 achieved by Sorensen (Sorensen et al., 2012).

Class comparison	**NT vs. Others (ours)**	**CLE vs. PSE**	**NT vs. Others (KNN)**
AUCs	0.8559	0.7633	0.713

Table 7-6: AUCs for Normal class vs. other cases and CLE vs. PSE.

7.4 Conclusion

This chapter has presented a cascaded approach using the combined features of the multifractal and alpha-histograms descriptors for the classification of emphysema in CT pulmonary images. The multifractal based descriptors demonstrate good performance in discriminating the normal emphysema class from other pathological cases with the sum intensity measure. The introduction of the alpha-histogram further improves the classification results. The performances of the descriptors are measured by the overall classification accuracy and the area under the ROC curves. Our results compared favourably well with the state-of-the-art methods used for emphysema detection, with an AUC of 0.8559 compared to 0.713. The proposed ideas significantly increase the classification accuracy, and confirm the effectiveness and robustness of the multifractal techniques in the classification of emphysema images.

The problem with the combined features is that the model complexity increases, which might slow the computational time and also increase the memory usage. So far, this thesis has been discussing the multifractal analysis of images using the Holder exponent for the computation of the intensity measures. Further effort would be to combine the LBP-based features with the multifractal techniques in the next chapter since the local features from the CT image has been very useful, and the results of the combined descriptors would be examined on the classification of emphysema in CT images. The

performances of the descriptors may be evaluated against other classification approaches.

8 ANALYSIS OF SCALE VARIATIONS

8.1 Introduction

Several methods for texture image classification and retrieval using either local or global image features have been reported in literature. Each type of features has its own merits and limitations. For example, the features of the local binary pattern (LBP) usually lack global spatial information while global descriptors would provide very little local information. This chapter proposes two different descriptors to circumvent these shortcomings by providing more information to describe different textural structures of the emphysema CT images. The proposed LBP+Multifractal Image (LMI) features and the rotational invariant LBP+Multifractal Image (RLMI) features can provide more accurate classification results by using a hybrid concatenation of the local and global features.

The experimental approaches are validated for different scales of emphysema images during the classification process in order to determine the appropriate image size that could yield the maximum classification accuracy. The goals of the thesis in this section are to develop methods that could efficiently improve the accuracy of the classifiers and also to analyse the effects of the combined features of the emphysema patterns and their variations with scale changes.

It has been discovered in the previous chapters of this thesis that the local features extracted from the HRCT images could provide good classification results. This chapter therefore proposes to use the information from the local and global

features to classify different textural structures of the images. First and foremost, ordinary LBP would be calculated by comparing the centre pixels of each image with its neighbouring pixels to generate the LBP codes (Timo Ojala, 2000)(Zhao & Matti, 2007b). General comparative analyses could also be accomplished using some performance measures like the classification accuracy, time complexity, processor memory usage and so on between the multifractal features (α-image and $f(\alpha)$ image) and the LBP.

We also propose to combine the LBP histogram features derived from the efficient LBP features with the features generated from the multifractal approach to generate a new descriptor that could be used for the classification process. The performances of the new descriptors obtained after the normalization and FS would be compared with the results obtained in the published paper by (Sørensen, 2010), which uses the joint LBP for the classification of emphysema images. The experimental analysis would also be investigated using different image sizes in order to see the effects on the performances and how it relates to the associated parameters. The second approach would combine the feature vectors derived from both rotation invariant local binary pattern (RILBP) histogram and the $f(\alpha)$ image features to construct another descriptor for the classification and analysis of emphysema images. The reason for concatenating the LBP-based features with the multifractal features is that, this idea would provide a generalization of the local intensity distributions and eventually give the global characterizations of the images. This proposed idea tends to compensate the global features or characteristics that the LBP is lacking since the multifractal feature is known as a global descriptor of digital images as discussed in these articles (Hemsley & Mukundan, 2009; Ibrahim & Mukundan, 2014, 2015). The combined features approach would hopefully provide a powerful tool that could be used for efficient texture classification. The FS could be used to select the highly discriminating features that could yield better results and reduce the space and time complexities.

8.2 Local Binary Patterns

The primary motivation for considering the Local Binary Pattern (LBP) here is that it is widely used as a texture descriptor (Timo Ojala, 2000)that has many similarities in their computation with alpha-histograms and multifractal descriptors. LBP labels the pixels of an image by thresholding the neighbourhood

of each pixel and assigning each neighbouring pixel a bit value, thus forming a binary value. This is similar to the computation of the alpha values using an intensity measure in the neighbourhood of a pixel. Similar to the alpha-histogram, the LBP approach also generates a histogram of binary values at each pixel, which is then used as features for classifying images.

The LBP gray scale variance of the neighbourhood, is specified using P sampling points on a circle of radius R as in (8.1).

$$LBP_{P,R} = \sum_{p=0}^{P-1} s(g_p - g_c)2^p \qquad (8.1)$$

$$s(x) = \begin{cases} 1, & if x \geq 0; \\ 0, & otherwise \end{cases} \qquad (8.2)$$

where g_c is the gray value at the central pixel, g_p is the value of its neighbours, P is the total number of involved neighbours, and R is the radius of the neighbourhood. LBP is uniform if the binary pattern contains at most two bitwise transitions from 0 to 1 or vice versa when the bit pattern is traversed circularly. A uniform pattern can be applied to reduce the length of the feature vector and implement a simple rotation-invariant descriptor. The example showing in Figure 8-1 illustrates the normal calculation of the LBP from the intensity values of the emphysema image pixels where the threshold value is 38 and after comparison with the neighbourhood values, the corresponding LBP binary codes are generated.

24	30	30
45	38	29
136	51	22

Threshold = 38

Binary = 00001111

0	0	0
1		0
1	1	0

Figure 8-1: Illustrating the example of LBP code of an emphysema image.

Similarly, in Figure 8.2, we have shown how the structural patterns of the image change with the efficient LBP codes and the RILBP after applying the radial filter.

It is noted from the structure of the images that efficient LBP is darker than the corresponding rotation invariant; this is expected because the magnitude of the intensity values of the image pixels in the efficient LBP is higher than the

equivalent pixel values in the RILBP. Though, they both receive the same binary codes when converted using the LBP approach; that is, LBP: 11111111 and RILBP: 11111111. The magnitude of the centre pixels (Threshold) within the normal image is 38, which is higher than the corresponding pixels in efficient LBP and RILBP since the 2D radial filter has removed some unwanted information that may be present within the image. These changes in the center pixels also demonstrate that the LBP is sensitive to noise and it also illustrates how important the center pixel is in texture characterization. The centre pixels also describe the gray level of the local patch and contain additional discriminant information that might be very useful during the classification process. The corresponding histograms for the regular LBP and the RILBP are shown with the images as presented in Figure 8-2. There is an option to extract two different features from the RILBP, that is, the rotation invariance sparse histogram and the rotation invariance tight-histograms as presented in Figure 8-2.

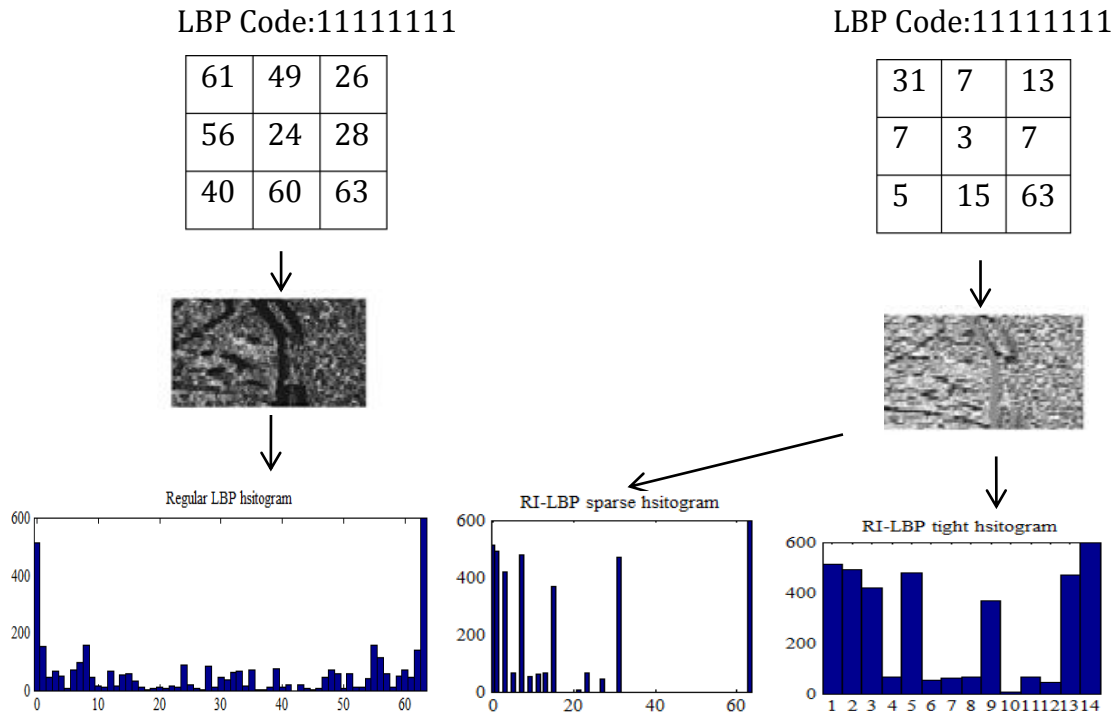

Figure 8-2: Illustrating different structural patterns of LBP and their corresponding codes.

8.3 Proposed Methods

The system overview of the construction of feature vectors that uses the LBP-based approach combined with the multifractal methods to generate a new descriptor combining LBP and multifractal image (LMI) is given in Figure 8-3. The input image from the emphysema database is filtered by using the radial filter function generated from the MATLAB. A round or radial filter is a 2D matrix generated using a specifying number of neighbours, which represents a different number of enabled filter elements and the radius of the filter. A circular filter is generated by subtracting the grey values of the centre pixel from the neighbouring pixels at different rotation angles as provided by (T Ojala, 2002).

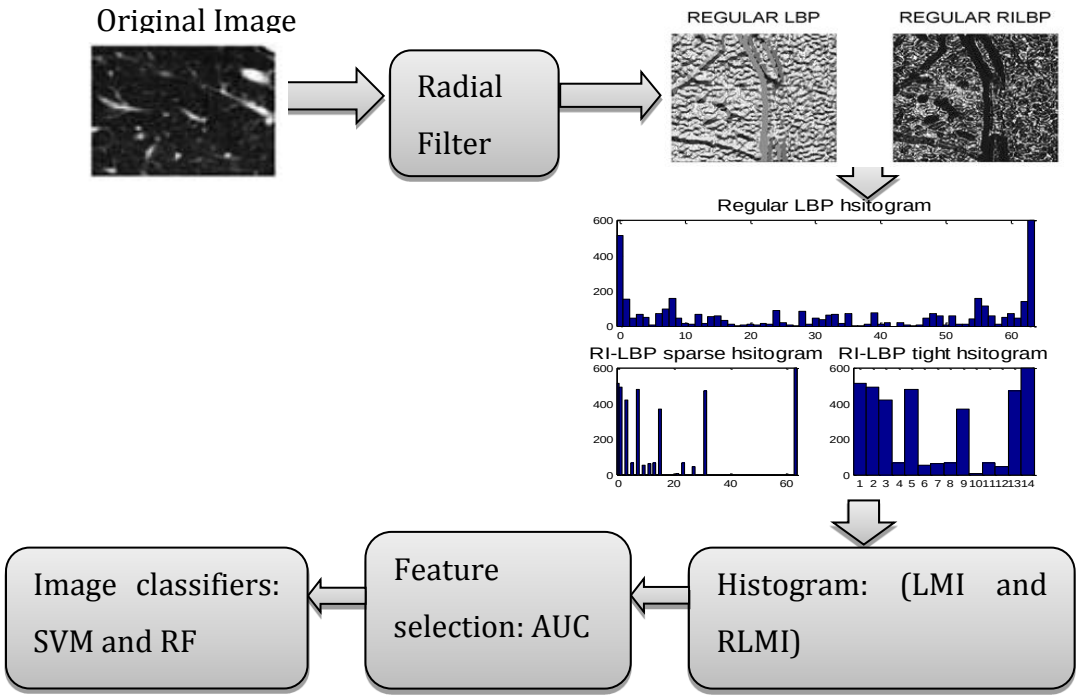

Figure 8-3: System overview of the emphysema classification using the LMI and RLMI descriptors.

The LBP is obtained by the general approach of comparing the centre pixel to the neighbouring ones. In this implementation, a general radial filter is introduced to get rid of the unwanted features such that only the useful information could be used for the computation of LBP. The rotation invariant descriptor is obtained using a search for the appropriate angle at which the LBP value of a given pixel is

minimal; the angle of rotation and the numbers of neighbours are other useful parameters that may influence the performances of the RILBP features. The RILBP histogram would always use less bins than the regular LBP since it induces an effective means of calculating the number of bins. In RILBP, the angle of rotation can be improved by the number of neighbouring points or the radius of the pixels. The RILBP would only concentrate on the relevant values by assigning a weight vector to the neighbouring pixels surrounding the unique pixels at the centre. Various invariants could also be obtained by shifting or rotating in such a way that the minimum possible values for a unique RILBP could be accomplished.

A tight histogram of the LBP is generated by changing the input matrix or image contrast, such that the bins are uniformly arranged or distributed and no empty bins exists within the histogram. This is accomplished by using a flag to determine if the histogram is tight (no empty bins) or if the minimum and maximum values of the input image are uniformly distributed.

8.4 Experimental Analysis

In this study, different experimental approaches are conducted on the features extracted from the emphysema patches using the LBP and f(α) image feature vectors computed. The details of the computation of the multifractal parameters like the alpha images, f(α) images have been described earlier in Section 6.2. The original size of the patches of the emphysema database is 61*61 pixels, but all the patches were rescaled into different window sizes in order to investigate the scale variation of the classification accuracies.

The classification system is tested with the patches of different sizes: 64*64, 128*128, 256*256, 320*320, 384*384 and 512*512 pixels. The features extracted from the LBP are the values obtained from the LBP histogram calculated after filtering with the radial filter and adjusted the bin size of the histogram into an appropriate size. The multifractal features are derived from the computation of fractal dimension of the corresponding pixels in the emphysema image patches. In this research, we considered three different types of emphysema patches, the Normal tissue (NT) emphysema, CLE and Paraseptal emphysema (PSE) using different window sizes of the corresponding patches. 50 images were selected from each emphysema class and the intensity values of the calculated LBP histogram and the $f(\alpha)$ image features for each patch are arranged in rows

towards the corresponding class labels to generate the data set, this is repeated for the 50 images in each group making up a total of 150 rows. Each row corresponds to an LBP; $f(\alpha)$image that has 64x64 pixels. Thus a total of 150 images would generate a high dimensional data set. After the pixel arrangements, in both LBP and $f(\alpha)$ image, we obtained a total of 9600*64, 19200*128, 38400*256, 48000*320, 57600*384 and 76800*512 pixels for 150 images in each NT, CLE and PSE emphysema images respectively. The corresponding pixels obtained from the two descriptors are concatenated as proposed to generate a new descriptor LMI, which is utilized in the classification procedures. The total data sets obtained after the concatenation are 9600*128, 19200*256, 38400*512, 48000*640, 57600*768 and 76800*1024 for the 64*64, 128*128, 256*256, 320*320, 384*384 and 512*512 patches respectively.

The same procedure is repeated for the construction of the second descriptor where the $f(\alpha)$ image features obtained from the multifractal based technique is also concatenated with the RILBP features as proposed. The dimensions of the images for both features remain the same as described and the newly constructed feature descriptor (RLMI) is also used in the classification process. During this process, the feature vector of each data set is clustered using 3 clusters in order to view how the three classes of emphysema data set are grouped; Figure 8-4 presents how the intensity distributions of a 64*64 pixel of the emphysema image after clustering are grouped.

Another exploratory test that could be useful would be to determine the correlation within the feature vectors in order to determine how correlated or uncorrelated the feature variables within the data sets are. As can be seen in Figure 8-4, the *k*-means clustering of the dataset was able to group together those features with similar attributes into the same category.

The second class CLE, has the highest number and it is indicated by the red colour, followed by the NT in black colour at the middle and lastly the PSE group with the green colour. This approach would help us to understand the general arrangement or an overview of the data sets before the classification process. As previously stated, these features are the combined features originally extracted from the efficient LBP histograms and the $f(\alpha)$ image feature vectors (joint histogram concatenation). After determining the correlation between the feature vectors, it was discovered that there are many irrelevant and redundant features that are not

useful, which could be eliminated. The column AUC is calculated to extract the feature variables with the important information that could be used to improve the classification accuracy. This is done for each data set and the four columns with the highest average AUC values are chosen for further classification process, while the observations or the matrix rows remain unchanged.

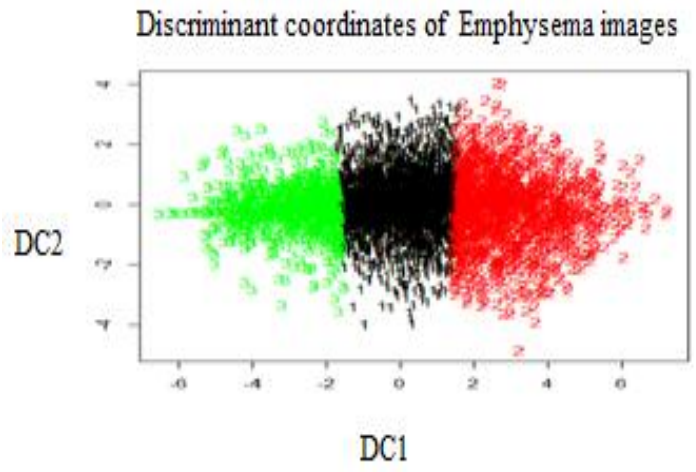

Figure 8-4: Illustrating the grouping of the emphysema classes after clustering, where the plots on the x-axis represent the discriminant coordinates 1(DC1) and the plots on the y-axis represent the discriminant coordinates 2 (DC2).

We could as well use the PCA for the FS or sequential feature selection techniques. For further understanding and the analysis of the data sets, Figure 8-5 presents the receiver operating characteristic (ROC) curves of the feature vector with the maximum AUC values (best features) for the patches with the window sizes of 64*64, 128*128 and 256*256.

The corresponding class pairwise AUC for each curve in the three data sets with different window sizes, is calculated and the results are shown in Figure 8-5. The results in Figure 8-5 indicate that the data sets with the highest window size (256*256) give the best total AUC value (**0.6668**), followed by the data sets with 128*128 pixel size, which also give a total AUC value of **0.6544.** Lastly, the features with the smallest patch size has the lowest AUC value as it can be seen from the corresponding ROC curves presented in Figure 8-5.

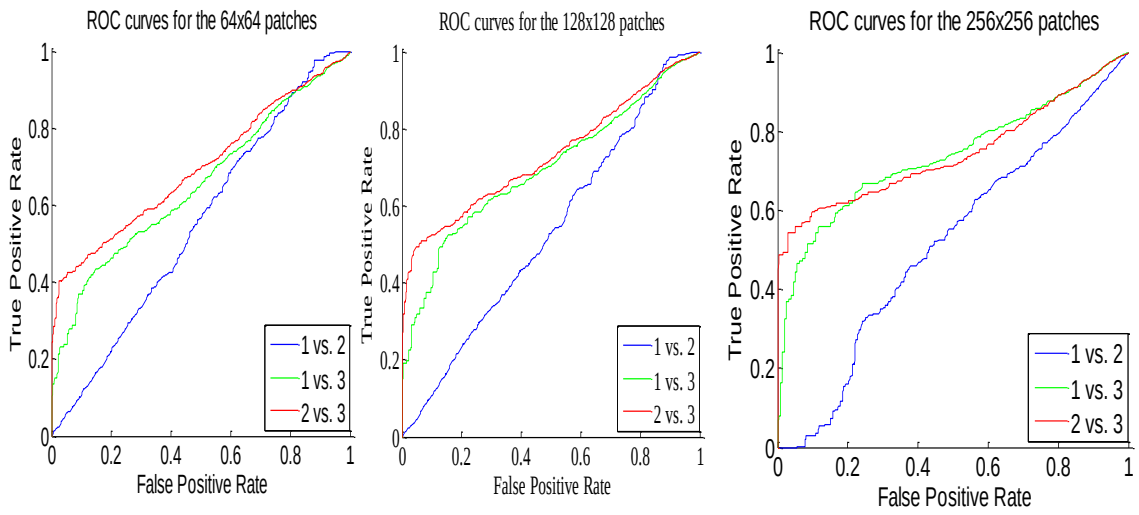

Figure 8-5: ROC curves for the best features selected from each data set of the three possible pairwise class combinations.

This process has helped to simplify the models in each data by reducing the matrix dimension from 128 dimensions for a 64*64 pixel image, 256 dimensions for a 128*128 pixel image and lastly 512 dimensions for a 256*256 pixel image into just four dimensions. This process of dimensionality reduction would definitely reduce the time and space complexities during the classification process and probably increase the classification accuracy as complex models sometimes over fit data sets and hence introduces errors. The simplified model would not only appropriately fit the data, but also save the memory utilization and the processor execution time.

According to the system overview shown in Figure 8-3, we propose to normalize the histogram data before applying the classifiers for the data classification. Another way to determine the differences within the data group is by using the multiple comparisons. The Tukey's test (Demšar & Demšar, 2006) is employed in this research to check further how significantly different are those groups within the data sets. Then a multiple comparison could be used to search for the specific differences between the possible pairwise groups in the data sets. After applying the Tukey Pairwise comparisons on the data sets for the grouping information, the results after the test show that the group means of the emphysema classes are significantly different. The information provided in the data sets could also be used to check which pair of means is significantly different, and which are not using the multiple comparisons.

Multiple comparisons could also be used to display a graph with each class mean represented by a symbol and an interval around the symbol. Two means are said to be significantly different if their means are disjointed, but insignificantly different if their intervals overlap.

Multiple comparisons of Emphysema class				
P. group	mean values	Std. error	t-values	P values
NT-CLE	0.025306	0.005119	4.944	P<0.0001
PSE-CLE	0.233890	0.005119	45.693	P<0.0001
PSE-NT	0.208585	0.005118	40.753	P<0.0001

Table 8-1: Multiple Comparisons of means using the Tukey's test.

In Table 8-1, it can be observed that the mean values of the pairwise class in the NT and CLE classes are significantly different from other classes, which is in line with the ROC curves generated in Figure 8-5. Figure 8-5 shows that it is easier to separate NT-CLE pairwise classes from others than the CLE-PSE and NT-PSE pairwise classes. The estimated values of the means for other class pairs are not significantly separated from each other as NT-CLE class does, which indicates that it is really difficult to separate these pairwise classes from each other and other classes. This is also demonstrated in Figure 8-5 using the ROC curves. The NT versus CLE indicated with blue colour in the ROC curves in Figure 8-5 is clearly separated from other classes while the CLE versus PSE and NT versus PSE pairwise classes are very close to each other and even the estimated values of the means in the Table 8-1 also confirm this with a p-value <0.0001 and about 95% confidence interval. This confirms that the data sets are grouped using the information provided.

8.5 Classification Results and Analysis

This section describes the classification experiments conducted to evaluate the discriminating capability of the combined features from the two descriptors, LBP and $f(\alpha)$. Based on the previous experiment, the BT performs better than the NB and random forests are improvement over bagged decision trees. We thought the RF could be used to further increase the classification accuracy of the CT images

since it is possible even with bagging that the decision trees can have many structural similarities and in turn have high correlation in their predictions.
We initially employ two different image classifiers due to the nature of the datasets used in this study; the support vector machine (SVM) (Marsland, 2014), and random forest (RF) (Breiman, 2001). The RF could be a perfect classifier for the multifractal datasets since it is relatively robust to outliers and noise, and always enhance better accuracy when random features are used. The RF randomly selects inputs or a combination of inputs to grow each tree. This can significantly improve the classification accuracy by combining trees grown using random features, and the generalization error of the forests reduces as the number of tree becomes large (Breiman, 2001). RF is a classification algorithm that is very suitable for microarray data sets; although RF is not widely used in the microarray, but it has characteristics that make it ideal for these data sets. It has excellent performance even with redundant predictive variables and can be used when the number of variable is much larger than the number of observation in a classification problem involving more than two classes. The details of the implementations of RF classifier can be found in (Breiman, 2001).

As shown in Figure 8-6, different features are extracted from the original emphysema images using the multifractal decomposition and the LBP-based approaches, the features are jointly combined in the form of hybrid to generate a histogram descriptor, which is used for the classification tasks using different image classifiers. That is, the $f(\alpha)$ and LBP features are mapped together to form a descriptor while the RILBP and the $f(\alpha)$-image features are mapped together to generate the second descriptor for the experimental analyses. We have decided to combine the features from the LBP and RILPB with the $f(\alpha)$-image features since the $f(\alpha)$ is dominant over the α-image features.

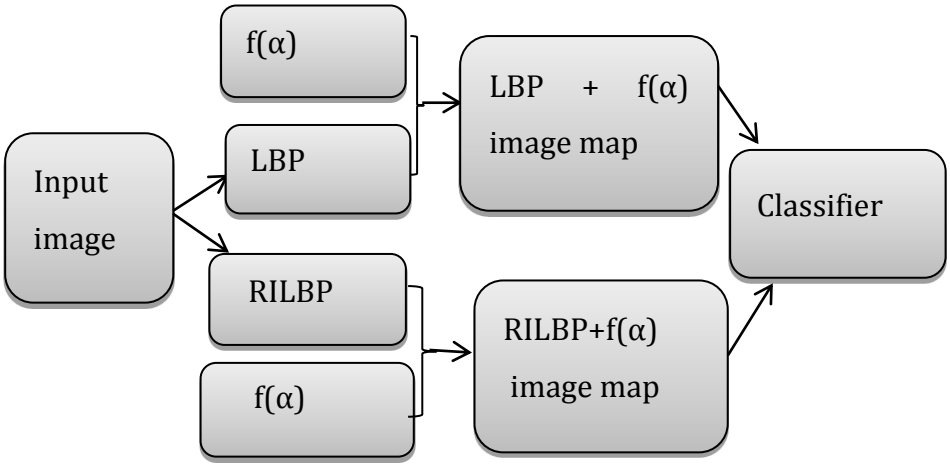

Figure 8-6: Overview of the joint concatenation methods for the development of the descriptors.

In this thesis, we initially used a "one-vs-all" classification approach using the SVM classifier. We used a software modules `svmTrain.m`, `svmPredict.m`developed in house for use with the MATLAB package. The module uses a linear kernel and a regularization parameter *C* that is varied from 1 (high bias, underfitting) to 100 (low bias, overfitting). The results obtained using the linear kernel were not satisfactory. Higher order Gaussian kernels can provide more accurate non-linear decision boundaries, but for our case since the dimensionality of the feature set is very large, we might require optimized versions of the SVM package such as the LIBSVM (Chang, 2016) .

In Table 8-2, we can see that, as the image resolution increases, the classification accuracy also increases. In other words, the data sets with the largest image sizes gave the best classification accuracy while the data sets with the smallest image pixel size gave the lowest performance. These results also show that as the image size is increasing the overall classification accuracy is also increasing, which indicates that the larger the window size, the higher the classification accuracy. This is simply because the images with the larger sizes have captured more useful information, which eventually increase the discriminating power of the features used in the classification process. The original size of the patches does not contain enough discriminative information, which led to the reduction in the performance accuracy of the classification system. Overall, the performance of the LMI

descriptor looks very good as the classification accuracy falls within the range of 75.18-97%. The scale invariance in the emphysema images has really influenced the performance of the classification system, though, 512*512 resolution size is the maximum that we have tested with this descriptor.

The performance of the classification system that uses 512*512 pixels has been impressive with an accuracy of 98%, even with big data sets, which are about 76800 rows and 1024 columns after the concatenation process as previously discussed. Probably, a further increase in the image window sizes might produce worse or better classification accuracy, but of course a classification accuracy of 98% is an excellent result. Generally, the RF classifier performed excellently well in all the cases and seem to be the most suitable classifier for our data sets.

The RF significantly improved the classification accuracy over the cascaded features using R programming language with an accuracy of 98%.

The results of the second descriptor that uses the combined features from the RILBP and the $f(\alpha)$ features would be experimentally analysed with the same procedures as the LMI. The classification results of the RILMI descriptor using different image sizes with the RF classifier are presented in Table 8.2.

Classification accuracy – LBP-$\boldsymbol{f(\alpha)}$		
Image Sizes	RILBP-$\boldsymbol{f(\alpha)}$	LBP-$\boldsymbol{f(\alpha)}$
64 * 64	52.08%	75.18%
128 * 128	59.06%	83.58%
256 * 256	70.73%	94.35%
320 * 320	75.1%	97.25%
384 * 384	82.1%	97.55
512 * 512	88.4%	98%

Table 8-2: Classification results of the LBP-f(α) descriptor.

Performances of the RILMI descriptor are slightly lower than the results we have obtained from the LMI. Overall, the results are not really bad, but the LMI outperforms the classification results obtained from the RILMI descriptor. The features derived from the LMI descriptor have higher discriminative power than the features obtained from the RLMI. The next stage of the experimental analysis

compares the results obtained from the LMI descriptor with the classification results given in Sorensen. The confusion matrix with the best classification accuracy, which uses the LMI descriptor with the image size of 512*512 pixels, is presented in Table 8.3 for comparison with the published paper, the state-of-art methods for the emphysema classification (Sorensen, 2010).

As can be seen in Table 8.3, our results compare favourably with the LBP results; the overall accuracy of 98% from the confusion matrix obtained from the emphysema image analysis compared to the accuracy of 95.2% that was achieved showed that the performance of the proposed descriptor is better in spite of a large volume of data sets. Additionally, our approach is simpler and faster in terms of time complexity.

It has been verified experimentally that the execution run time to generate the $f(\alpha)$ features is about 5 times faster than the time it would take to calculate LBP features using the same image size. Take for instance, for a 128*128 pixel size, the regular LBP run time was around 3.8s whereas it took just 0.7s to generate the $f(\alpha)$ image of the same image size. Similarly, for a 512 * 512, the execution run time for the regular LBP was around 53.14s while both α and $f(\alpha)$ features can be calculated in just 9.9s. The experimental tests for the time complexities were carried out for four different image sizes on a machine with Intel Pentium of 2.2GHz processor and 4GB of RAM. The four image pixels used for the experiments are as follows; 64*64, 128*128, 256*256 and 512*512 for comparison between the regular LBP and the $f(\alpha)$ image features. Generally, the LBP consumes more computational time than the $f(\alpha)$ image. This can be very important, especially when dealing with a very large volume of data sets like 512*512 during classifications, which are around 76800 rows with 1024 columns. The details of the computational time for both feature descriptors are presented in Table 8.4 using different image patches.

It has been demonstrated in this research work the effectiveness of the combined features derived from both LBP and the multifractal descriptors in the classification of the emphysema images. In the experimental analysis, we could see how powerful this descriptor is and how it behaves under different scale changes. The multifractal features extracted from the $f(\alpha)$ features have shown to be more powerful or more discriminating than the other features from the LBP and RILBP as this was verified during the experiments.

	LBP			LBP-$f(\alpha)$		
Actual		Predicted			Predicted		
		NT	CLE	PSE	NT	CLE	PSE
	NT	93	0	7	98	0	2
	CLE	2	98	0	2	98	0
	PSE	3	2	95	2	0	98

Table 8-3: Comparison of classification results (shown as percentages) using the new descriptor and the LBP approach.

Computational Time in seconds		
Image size	f(α) image	Regular LBP
64 *64	0.3217s	1.3431s
128 *128	0.7173s	3.804s
256 * 256	2.3865s	13.8164s
512 * 512	9.9017s	53.1436s

Table 8-4: Computational time comparisons between the multifractal f(α) image and the regular LBP.

This explains the importance of global features obtained from the multifractal descriptors $f(\alpha)$compared to the local features from the LBP and the combined features from both descriptors, which also behave well under different scale changes.

Some of the important parameters that are very useful during the experimental analysis for the RF classifier are the number of growing trees and the number of the predictor variables. Though, since most data sets used in the experiments are high dimensional data, the Column AUC is applied to reduce the dimension of the data sets into just four predictor variables. It was confirmed during the experimental analyses that as the number of growing trees increases for constructing the classification models, the classification accuracy also increases.

This process is used to determine the appropriate number of growing trees that could yield the best classification accuracy.

The general picture of the relationship between the classification accuracy and the corresponding classifier is presented with the plots in Figure 8-7.

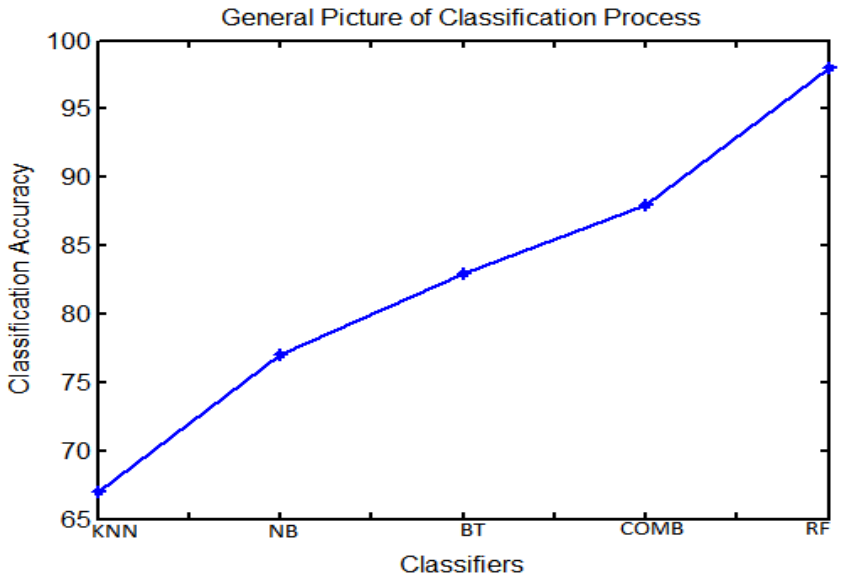

Figure 8-7: Showing the relationship between the classification accuracy and classifier

8.6 Conclusions and Future Work

In this study, we have analysed the effect of different scale invariants on the emphysema image classification using two different descriptors. We have shown that the proposed descriptors could perform well even with big data sets having about 76800 rows with 1024 columns, especially the LMI that has really shown excellent performances in all cases. This is a great achievement as the classification of large data sets involved in this experiment may sometimes pose some challenges that may affect the performances of the classification system. But, in this case, as the data sets increase, the classification accuracy increases until the algorithm converges. The two descriptors proposed; the LMI and the RILMI were defined to extract the textural characteristics of the images combined with the global properties for the classification of the images.

We have also demonstrated using the LMI that the window sizes of the image have great influence on the classification accuracy. The combined feature that uses the LMI is better than the other descriptor (RILMI). Likewise, the fusing of the LBP and

$f(\alpha)$ either in a joint or hybrid form produced a very good performance with overall classification accuracy of 98%. LMI also outperforms the results obtained from the published article by Sørensen (2010), which demonstrated the effectiveness and robustness of the proposed descriptor. The classification result that uses the original image scale (64*64) from the emphysema database indicate that, the LMI achieves 75.18% using the RF classifier while the RILMI reaches only 52.08%. This demonstrates that even before applying the scale invariances, LMI outperforms the RILMI descriptors, which shows that the features from LMI possess better discriminating power than the features from RILMI.

Additionally, the changes in scale invariance do have significant changes in the classification accuracy in both descriptors (Table 8.2), an increase in the image scale further increases the classification accuracy. This proves that the changes in the scale invariance of the emphysema images further increase the discriminating capability of the features in the descriptors.

Overall, the results also indicate that the LMI descriptor outperforms the earlier approaches and demonstrate the discriminating power and robustness of the combined features for accurate classification of emphysema CT images. One of the limitations in this research framework is that the RILMI features did not combine well with the alpha image features as this was experimentally verified during the classification process. Also in LMI, an increase in the data sets keeps increasing the classification accuracy, but also demanding more memory usage and the processor computational time. In order to improve the performances of the descriptors, changes in the parameters like the number of neighbours, radius of pixels and even the angle of rotating the LBP when calculating the RILBP might provide better results. The column AUC for feature dimensional reductions worked really well, but the PCA might yield better results.

9 CONCLUSIONS AND FUTURE WORK

9.1 Conclusions

Medical image analysis algorithms for automatic segmentation, extraction of regions of interest and classification based on features present in the image have found useful applications as diagnostic tools in pathological assessments. This thesis has presented several novel methods for emphysema classification and segmentation of regions of interest using multifractal descriptors. Chapters 2 provided the theoretical foundations of fractals that are important in image processing applications, and discussed the mathematical aspects of different forms of fractal dimensions. Chapter 3 introduced four key multifractal measures used in this thesis, and described the computation of important multifractal features such as the alpha histogram, the multifractal spectrum and the Renyi spectrum. Chapter 4 presented an extensive literature review of work in the fields of image analysis methods using fractal and multifractal descriptors. Experiments performed in later chapters are designed and implemented to tackle some of the classification problems outlined in the existing work. Gaps in existing research work such as the application of Higuchi dimension in medical image analysis have been identified and later used in the thesis to develop new algorithms. The main contributions of this thesis has been organised into four chapters (Chapters 5-8) and the important findings are summarized below.

Chapter 5 introduced the problem of automatic classification of emphysema patterns in HRCT images and provided the framework for analysing those images using multifractal descriptors. An online image database (Sorensen, Shaker, & de Bruijne, 2010) was used for detailed experimental analysis. Results showing inter-class variance and intra-class similarities in multifractal features demonstrated the effectiveness and discriminating power of the features in the analysis and classification of the lung CT images. The chapter also presented novel algorithms for the analysis of emphysema image patterns using the Renyi spectrum and the Higuchi dimension as features.

In image classification problems involving large number of features, it is important to incorporate feature selection methods to improve the classification accuracy. Features such as the multifractal spectra, Renyi spectra and alpha-histograms can all contain large numbers of values. A feature selection technique was designed specifically for improving the classification accuracy of the emphysema patterns in Chapter 6. The Naïve Bayes and the bagged decision tree classification algorithms were investigated with several experimental approaches for comparison purposes. The experiments concluded that the number of growing trees and the threshold values could affect the classification accuracy of the classifiers, and the performance of the classifiers after feature selection has been consistently higher than the results obtained without FS.

Cascaded techniques for further improvement of emphysema classification accuracy were proposed in Chapter 7. This chapter proposed a method that used alpha-histogram for the classification of the CLE and PSE images, and combined the results with the results obtained from Multifractal descriptors. We employed the AUC for best FS and the performance of the classifiers are measured by the error matrix and the AUC. Our results compared favourably well with the state-of-the-art measure for emphysema classification. The proposed ideas significantly increased the classification accuracy and confirm the effectiveness and robustness of the multifractal techniques. The pairwise AUC of the combined features for the three classes of the emphysema are analysed and represented with ROC curves. The mean AUC of 0.8251 was accomplished compared to the 0.713 achieved by the previous method. This is a significant result as the developed descriptors generated an estimated accuracy of 94%, and could be further improved even with much larger data sets.

Chapter 8 explored the possibility of combining multifractal descriptors with local texture feature descriptors such as the Local Binary Patterns. Two new descriptors were proposed: the first descriptor, LMI, was developed by combining the local information from the LBP with the global information from the multifractal data sets. The second descriptor, RLMI was developed by a hybrid concatenation of the local features from the rotational invariant LBP and the features obtained from the alpha image. We have shown that these original descriptors could perform well even with big data sets, especially the LMI descriptor that has demonstrated excellent performance in all experimental cases. The LMI descriptor recorded an overall classification accuracy of 98%, and outperformed the results obtained by the state-of-the-art methods for emphysema classification. This is a major contribution of this thesis; none of the previous approaches used in the emphysema database for the classification of emphysema patterns has attained this accuracy. Another significant contribution in this chapter is that the proposed algorithms could operate on large data sets at a very high speed without affecting the performances of the classification system.

Overall, this research work has provided a significant number of contributions in the field of multifractal analysis of medical images, specifically for emphysema pattern classification. The thesis also expands on the multifractal approaches to solving classification and segmentation problems by introducing new algorithm involving related feature descriptors such as Renyi and Higuchi dimensions, and local features such as LBP.

9.2 Limitations and Future Work

The successful applications of multifractal analysis of HRCT images have been encouraging. This suggests that solutions to similar classification problems could be attempted in other types of imaging modalities such as the MRI and US.

It is possible for the object with different surfaces to have the same fractal dimension. In some cases, images with similar FD values may not necessarily come from the same source. This is the point at which lacunarity becomes very useful. It can be used to describe further the fractal patterns of different images from different samples having the same fractal dimensions. Lacunarity is based on the pixel distribution for an image, which can be derived from scans at different box

sizes at different grid orientations. In order to solve this problem, lacunarity can be combined with the fractal dimension to generate a new set of features.

Higuchi's fractal dimension of the image at different regions can be calculated in the form of multifractal framework. This can be accomplished by generalization of Higuchi's dimension such that the Higuchi singularity spectrum is generated instead of a single FD value. The features extracted from this spectrum would definitely improve the recognition accuracy of the image patterns.

The performances of the NB and the BT classifiers used in Chapter 6 can be improved by cascading the two algorithms over the data sets during the classification process. After the cascading technique, parallelizing the algorithms using the GPU parallel computing might further improve the computational efficiency of the algorithms.

Although, we showed some multi-scale characteristic properties of the emphysema images in Chapter 5 by applying generalized dimensional spectra parameters for detection and identification of ROI analysis. However, the development of a wavelet-based multifractal formalism for multi-scale and multi-resolution characteristics of the image might provide better results. In this case, Wavelet based approach of multifractal analysis could be applied to decompose an image into a set of approximation coefficients (low frequency components) and detail coefficients (high frequency components). The orthogonal wavelet transformation of an image that results into three sets of generated detail coefficients; diagonal, horizontal and vertical can be calculated. The local singularity measure of a digital image would be defined using the scaling properties of its wavelet coefficients. The frequency of occurrence of a given singularity strength is measured by the multifractal spectrum and the descriptors of the multifractal spectrum produced might be used for the classification of medical images.

The features obtained from the Rotational Invariant LBP in Chapter 8 did not combine well with the alpha image features. This is understandable because the information from both data sets is locally constructed; we therefore decided to combine the RLMI descriptor with the $f(\alpha)$ image features**.** Global features of the image can be generated by developing a generalized rotation invariant operator for detecting certain image features; the features obtained can therefore be concatenated with the local features from the alpha images to generate a new descriptor that could be used in texture classifications.

10 REFERENCES

Abraham, R., Simha, J. B., & Iyengar, S. S. (2008). Effective Discretization and Hybrid feature selection using Naïve Bayesian classifier for Medical datamining, *4*(2), 1–13.

Accardo, A., Affinito, M., Carrozzi, M., & Bouquet, F. (1997). Use of the fractal dimension for the analysis of electroencephalographic time series. *Biological Cybernetics*, *350*, 339–350.

Agarwal, G., Mishra, S. P., Maurya, S., Chaudhary, S., & Murala, S. (2017). Local peak valley co-occurrence patterns: A new feature descriptor for image retrieval.*International Conference on Signal and Information Processing (IConSIP)*.

Ahammer, H. (2011). Higuchi Dimension of Digital Images. *PLoS One*, *6*(9), 1–8. doi:10.1371/journal.pone.0024796

Ahonen, T. (2009). Rotation Invariant Image Description with Local. *Scia*, 61–70. doi:10.1007/978-3-642-02230-2_7

Appleby, S. (1996). Pattern of the Human Population. *Geographical Anaysis*, *28*(2), 147–160.

Atupelage, C., Nagahashi, H., Yamaguchi, M., Abe, T., & Hashiguchi, A. (2013). Computerized Medical Imaging and Graphics Computational grading of hepatocellular carcinoma using multifractal feature description. *Computerized Medical Imaging and Graphics*, *37*(1), 61–71. doi:10.1016/j.compmedimag.2012.10.001

Azim, T., & Niranjan, M. (2014). Texture Classification with Fisher Kernel Extracted from the Continuous Models of RBM. *Proc. Intnl. Conf. on Computer Vision Theory and Applications*.

Bahreini, L., Homayoun, J., & Gity, M. (2010). Classification of Breast Lesions in Dynamic Contrast - Enhanced MR Images. *Proceedings of the 17th Conference of Biomedical Engineering*, 1–4.

Baravalle, G. B., Delrieux, C. A., & Gómez, J. C. (2015). Multifractal characterisation and classification of bread crumb digital images, *9*, 1–10.

Berwald, J. J. (2011). Computing Multifractal Spectra Via Simplicial Measures.

Bhuvaneswari, R., & Kalaiselvi, K. (2012). Naive Bayesian Classification Approach in Healthcare Applications. *International Journal of Computer Science*, *3*(1), 106–112.

Block, A., von Bloh, W., & Schellnhuber, H. (1990). Efficient box-counting determination of generalized fractal dimensions. *Physical Review A*, *42*(4), 1869–1874. doi:10.1103/PhysRevA.42.1869

Block Imaging web portal. (2011). Retrieved June 6, 2017, from https://info.blockimaging.com/bid/70751/ge-lightspeed-qx-i-vs-ge-lightspeed-plus-ct-scanners

Blum, A. L., & Langley, P. (1997). Selection of relevant features and examples in machine learning. *Artificial Intelligence*. doi:10.1016/S0004-3702(97)00063-5

Breiman, L. (2001). Random forests. *Machine Learning*, *45*, 5–32. doi:10.1023/A:1010933404324

Broniatowski, M., & Mignot, P. (2001). A self-adaptive technique for the estimation of the multifractal spectrum. *Statistics & Probability Letters*, *54*(2), 125–135. doi:10.1016/S0167-7152(00)00210-8

Castiglioni, P., Rienzo, M. Di, Parati, G., & Faini, A. (2011). Fractal dimension of mean arterial pressure and heart-rate time series from ambulatory blood pressure monitoring devices. *Computing in Cardiology (CinC)*, *38*, 593–596.

Chabat, F., Yang, G., & Hansell, D. (2003). Obstructive lung diseases: texture classification for differentiation at CT Radiology., *228*(3), 871–877.

Chan, K. L. (1992). Fractal Based Texture Analysis. *Singapore ICCS/ISITA*, 102–106.

Chang, C. C., & Lin, C. J. (2016). LIBSVM - A Library for Support Vector Machines. Retrieved from https://www.csie.ntu.edu.tw/~cjlin/libsvm/.

Chaudhuri, B. B., & Sarkar, N. (1995). Texture segmentation using fractal dimension. *IEEE Transactions on Pattern Analysis and Machine Intelligence*, *17*(1), 72–77. doi:10.1109/34.368149

Chen C.C., Daponte, J.S., & Fox, M.D. (1989), Fractal feature analysis and classification in medical imaging, *IEEE Trans. on Medical Imaging,* 8(2), 133-142.

Chen, H., Sun, X., Chen, H., Wu, Z., & Wang, B. (2004). Some problems in multifractal spectrum computation using a statistical method. *New Journal of Physics*, *84*, 1–17. doi:10.1088/1367-2630/6/1/084

Chhabra, A., & Jensen, R. V. (1989). Physical Review letters. *Direct Determination of the F(alpha) Singularity Spectrum*, *62*(March), 1327–1330.

Choi, E., & Lee, C. (2003). Feature extraction based on the Bhattacharyya distance. *The Journal of the Pattern Recognition Society*, *36*, 1703–1709. doi:http://10.1016/S0031-3203(03)00035-9

Clarke, K. C. (1986). Computation of the fractal dimension of topographic surfaces using the triangular prism surface area method. *Computers & Geosciences*, *12*(5), 713–722. doi:10.1016/0098-3004(86)90047-6

Cosatto, V. F., Liew, G., Rochtchina, E., Wainwright, A., Zhang, Y., Hsu, W., … Wang, J. J. (2010). Retinal vascular fractal dimension measurement and its influence from imaging variation: results of two segmentation methods. *Current Eye Research*, *35*(9), 850–856. doi:10.3109/02713683.2010.490628

Dan, Z., Chen, Y., Yang, Z., & Wu, G. (2014). An improved local binary pattern for texture classification. *Optik - International Journal for Light and Electron Optics*, *125*(20), 6320–6324. doi:10.1016/j.ijleo.2014.08.003

Demir, B., Bovolo, F., & Bruzzone, L. (2013). Sequential cascade classification of image time series by exploiting multiple pairwise change detection. *IGARSS*, 3946–3949.

Demšar, J., & Demšar, J. (2006). Statistical Comparisons of Classifiers over Multiple Data Sets. *The Journal of Machine Learning Research*, *7*, 1–30. doi:10.1016/j.jecp.2010.03.005

Demšar, J., Leban, G., & Zupan, B. (2005). Freeviz-an intelligent visualization approach for class-labeled multidimensional data sets. *Proceedings of IDAMAP*, *1*, 13–18.

Dharmagunawardhana, C., & Mahmoodi, S. (2014). Quantitative analysis of pulmonary emphysema using isotropic Gaussian Markov random fields, 44–53. Retrieved from http://eprints.soton.ac.uk/360198/

Ding, Y., Dai, H., & Zhang, H. (2014). Automatic detection of microcalcifications with multifractal spectrum. *Bio-Medical Materials and Engineering*, *24*, 3049–3054. doi:10.3233/BME-141126

Domingos, P. (1997). On the Optimality of the Simple Bayesian Classifier under Zero-One Loss. *Machine Learning*, *29*, 103–130.

Don, S., Chung, D., Revathy, K., Choi, E., Min, D. (2012). A new approach for mammogram image classification using fractal properties, *Cybernetics and Information Technologies,* 12(2), 69-83.

Doyle, S., Feldman, M., Tomaszewski, J., Shih, N., & Madabhushi, A. (2011). Cascaded Multi-class Pairwise Classifier (CASCAMPA) for Normal, Cancerous,and Cancer Confounder Classes in Prostrate Histology. *IEEE Intnl. Symposium on Biomedical Imaging*, 715–718.

Dubey, S.R., Singh, S.K., & Singh, R.K. (2016). Local bit-plane decoded pattern: A novel feature descriptor for biomedical image retrieval, *IEEE Jrnl. of Biomedical and Health Informatics,* 20(4), 1139-1147.

Dubuisson, M.-P., & Dubes, R. C. (1994). Efficacy of fractal features in segmenting images of natural textures. *Pattern Recognition Letters*, *15*(April), 419–431. doi:10.1016/0167-8655(94)90091-4

Duda, R., Hart, P., & Stork, D. (2011). Pattern classification and scene analysis. *IEEE Transactions on Image Processing*, *20*(10), 2837–2847.

Emphysema imaging web portal. (2006). Retrieved December 6, 2015, from http://emedicine.medscape.com/article/355688-overview

Emphysema imaging web portal. (2016). Retrieved March 11, 2017, from http://www.emedicinehealth.com/emphysema/article_em.htm

Esgiar, A.N., Naquib, R.N., Sharif, B.S., Bennett, M.K., & Murray, A. (2002). Fractal analysis in the detection of colonic cancer images, *IEEE Trans. on Info. Tech. in Biomedicine,* 6(1), 54-58.

Esteller, R., Vachtsevanos, G., Echauz, J., & Litt, B. (2001). A Comparison of waveform fractal dimension algorithms. *IEEE Transactions on Circuits and Systems I: Fundamental Theory and Applications*, *48*(2), 177–183. doi:10.1109/81.904882

Evertsz, C., & Mandelbrot, B. (1992). Multifractal measures. In Chaos and Fractals. New.

Falconer, K. (2003). Fractal Geometry- Mathematical Foundations and Applications. (2nd ed.). London: Wiley.

Fekkai, S., Al-Akaidi, M., & Blackledge, J. (2000). Fractal Dimension Segmentation: Isolated Speech Recognition. In *Speech coding for algorithms for Radio Channels (Ref. No. 2000/012), IEE Seminar.* (pp. 1–5).

Fu, X., & Wang, L. (2003). Data dimensionality reduction with application to simplifying RBF network structure and improving classification performance. *IEEE Transactions on Systems, Man, and Cybernetics, Part B: Cybernetics*, *33*(3), 399–409. doi:10.1109/TSMCB.2003.810911

Gavrovska, A., Zajić, G., Reljin, I., & Reljin, B. (2013). Classification of prolapsed mitral valve versus healthy heart from phonocardiograms by multifractal analysis. *Computational and Mathematical Methods in Medicine*, *2013*, 376152. doi:10.1155/2013/376152

Gómez, C., Mediavilla, Á., Hornero, R., Abásolo, D., & Fernández, A. (2009). Use of the Higuchi ' s fractal dimension for the analysis of MEG recordings from Alzheimer ' s disease patients. *Medical Engineering & Physics*, *31*(3), 306–313.

Gomez, W., Pereira, W. C. a, & Infantosi, a F. C. (2012). Analysis of co-occurrence texture statistics as a function of gray-level quantization for classifying breast ultrasound. *IEEE Transactions on Medical Imaging*, *31*(10), 1889–99. doi:10.1109/TMI.2012.2206398

Gouravaraju, S., & Ganguli, R. (2012). Estimating the Hausdorff–Besicovitch dimension of boundary of basin of attraction in helicopter trim. *Applied Mathematics and Computation*, *218*(21), 10435–10442. doi:10.1016/j.amc.2012.03.104

Guo, Y., Zhao, G., & Pietik, M. (2012). Discriminative features for texture description. *Pattern Recognition*, *45*, 3834–3843. doi:10.1016/j.patcog.2012.04.003

Guo, Z., Li, Q., You, J., Zhang, D., & Liu, W. (2012). Local directional derivative pattern for rotation invariant texture classification. *Neural Computing and Applications*, *21*(8), 1893–1904. doi:10.1007/s00521-011-0586-6

Guo, Z., Zhang, L., & Zhang, D. (2010). A Completed Modeling of Local Binary Pattern Operator for Texture Classification. *IEEE Transactions on Image Processing*, *16*(6), 1657–1663.

Ha, T. H., Yoon, U., Lee, K. J., Shin, Y. W., Lee, J.-M., Kim, I. Y., … Kwon, J. S. (2005). Fractal dimension of cerebral cortical surface in schizophrenia and obsessive-compulsive disorder. *Neuroscience Letters*, *384*(1-2), 172–176. doi:10.1016/j.neulet.2005.04.078

Han, Y., Park, K., & Lee, Y. K. (2011). Confident wrapper-type semi-supervised feature selection using an ensemble classifier. 2011 2nd International Conference on Artificial Intelligence, Management Science and Electronic Commerce, AIMSEC 2011 - Proceedings, 4581–4586. doi:10.1109/AIMSEC.2011.6010202

Hanen, A., Imen, B., Abdallah, B., Patrick, D., & Mohamed, B. (2009). Multifractal modelling and 3D lacunarity analysis. *Physics Letters A*, *373*(40), 3604–3609. doi:10.1016/j.physleta.2009.07.087

Hee, S., & Choi, J. Y. (1998). A Methods of Image Enhancement and Fractal Dimension for Detection of Microcalcifications in Mammogram. In *Proceedings of the 20th Annual International Conference of the IEEE Engoneering in Medicine and Biology Society* (Vol. 20, pp. 1009–1012).

Heikkilä, M., Pietikäinen, M., & Heikkilä, J. (2004). A texture-based method for detecting moving objects. *Bmvc*, *28*(4), 10–21. doi:10.5244/C.18.21

Hemsley, A., & Mukundan, R. (2009). Multifractal Measures for Tissue Image Classification and Retrieval. *11th IEEE International Symposium on Multimedia*, 618–623. doi:10.1109/ISM.2009.94

Hentschel, H. G. E., & Procaccia, I. (1983). The Infinite Number of Generalized Dimensions of Fractals and Strange Attrators. *North-Holland Publishing*, 435–444.

Higuchi, T. (1988). North-Holland Physics Publishing Division. *Physical D 31*, 277–283.

Hinrikus, H., Bachmann, M., Karai, D., Klonowski, W., Lass, J., Stepien, P., … Tuulik, V. (2011). Higuchi's fractal dimension for analysis of the effect of external periodic stressor on electrical oscillations in the brain. *Medical and Biological Engineering and Computing*, *49*(5), 585–591. doi:10.1007/s11517-011-0768-5

Huang, Q., Lorch, J. R., & Dubes, R. C. (1994). Can the fractal dimension of images be measured? *Pattern Recognition*, *27*(3), 339–349. doi:10.1016/0031-3203(94)90112-0

Ibrahim, M., & Mukundan, R. (2014). Multifractal Techniques for Emphysema Classification in Lung Tissue Images. *International Proceedings of Chemical,Biological & Environmental Engineering*, *78*, 115–119. Retrieved from http://www.etlibrary.org/?m=fbook&a=details&aid=15734

Ibrahim, M., & Mukundan, R. (2015). Cascaded techniques for improving emphysema classification in computed tomography images. *Artificial Intelligence Research*, *4*(2), 112–118. doi:10.5430/air.v4n2p112

Ida, T., & Sambonsugi, Y. (1998). Image segmentation and contour detection using fractal coding. *IEEE Transactions on Circuits and Systems for Video Technology*, *8*(8), 968–975. doi:10.1109/76.736726

Iftekharuddin, K. M., Jia, W., & Marsh, R. (2003). Fractal analysis of tumor in brain MR images. *Machine Vision and Applications, Springer-Verlag*, *13*, 352–362.

Im, K., Lee, J. M., Yoon, U., Shin, Y. W., Soon, B. H., In, Y. K., … Kim, S. I. (2006). Fractal dimension in human cortical surface: Multiple regression analysis with cortical thickness, sulcal depth, and folding area. *Human Brain Mapping*, *27*(12), 994–1003. doi:10.1002/hbm.20238

Irini, R., Reljin, B., Pavlovic, I., & Rakocevic, I. (2000). Multifractal analysis of gray-scale images. 2000 10th Mediterranean Electrotechnical Conference. Information Technology and Electrotechnology for the Mediterranean Countries. Proceedings. MeleCon 2000 (Cat. No.00CH37099), 2, 490–493. Retrieved from www.worldscientific.com/doi/pdf/10.1142/S0218348X11005403

Jayasuriya, S. a., Liew, a. W. C., & Law, N. F. (2013). Brain symmetry plane detection based on fractal analysis. *Computerized Medical Imaging and Graphics*, *37*(7-8), 568–580. doi:10.1016/j.compmedimag.2013.06.001

Jiménez, J. (2004). The Contributions of A. N. Kolmogorov to the theory of turbulence. *Arbor*, *CLXXVIII*(704), 589–606. doi:10.3989/arbor.2004.i704.550

Jin, X. C., & Ong, S. H. (1995). A practical method for estimating fractal dimension, *16*(May), 457–464.

Jing, Z. L., Zhang, L. D., & Yue, G. H. (2003). Fractal dimension in human cerebellum measured by magnetic resonance imaging. *Biophysical Journal*, *85*(6), 4041–4046. doi:10.1016/S0006-3495(03)74817-6

Kalauzi, A., Bojić, T., & Vuckovic, A. (2012). Modeling the relationship between Higuchi's fractal dimension and Fourier spectra of physiological signals. *Medical and Biological Engineering and Computing*, *50*(7), 689–699. doi:10.1007/s11517-012-0913-9

Kallergi, M. (2005). Evaluation strategies for medical-image analysis and processing methodologies. *International Journal of Image Analysis and Processing Methodologies*, *2*(5), 75–91.

Karabulut, E. M., & Ibrikci, T. (2015). Emphysema discrimination from raw HRCT images by convolutional neural networks. *IEEE Intnl. Conf. on Elec. and Electronics Engineering (ELECO)*, 705-7-8.

Kenkel, N. C., & Walker, D. J. (1996). Fractals in the Biological Sciences. *COENOSES 11*, *100*, 77–100.

Kenneth, F. (2013). Fractal Geometry Mathematical Foundations and Applications.

Khider, M., Haddad, B., Ahmed, A. T., Technologie, D., Boumedienne, H., & Ezzouar, B. P. B. (2013). Multifractal Analysis BY The Large Deviation Spectrum. *International Workshop on Systems, Signal Processing and Their Applications*, *8*, 112–115.

Kiselev, V. G., Hahn, K. R., & Auer, D. P. (2003). Is the brain cortex a fractal? *NeuroImage*, *20*(3), 1765–1774. doi:10.1016/S1053-8119(03)00380-X

Klonowski, W. (2000). Signal and image analysis using chaos theory and fractal geometry. *Machine Graphics and Vision*, 1–32.

Kohavi, R., & John, H. (2011). Artificial Intelligence Wrappers for feature subset selection. *Data Mining and Visualization Silicon Graphics*, *97*(97), 273–324.

Kuklinski, W.S. (1994). Utilization of fractal image models in medical image processing. *Fractals*, 2(3), 363.

Kwak, J. T., Xu, S., & Wood, B. J. (2015). Efficient data mining for local binary pattern in texture image analysis. *Expert Systems with Applications*, *42*(9), 4529–4539. doi:10.1016/j.eswa.2015.01.055

Ladha, T. D. (2011). Feature selection methods and algorithms. *International Journal of Computer Science and Engineering*, *3*(5), 1787–1797.

Lahiri, T., Mishra, H., Sarkar, S., & Misra, K. (2008). Bioinformation surface characterization of proteins using multi- fractal property of heat-denatured

aggregates Bioinformation. *Biomedical Informatics Publishing Group*, *9*(2), 379–383.

Lam, A., & Li, Q. (2010). Fractal Analysis and Multifractal Spectra for the Images. *International Symposium on Computer, Communication, Control and Automation*, 530–533.

Lee, W., Chen, Y., Chen, Y., & Hsieh, K. (2005). Unsupervised segmentation of ultrasonic liver images by multiresolution fractal feature vector. *Information Sciences*, *175*, 177–199. doi:10.1016/j.ins.2005.01.007

Liu, L., Zhao, L., Long, Y., Kuang, G., & Fieguth, P. (2012). Extended local binary patterns for texture classification. *Image and Vision Computing*, *30*(2), 86–99.doi:10.1016/j.imavis.2012.01.001

Liu, Q., Shi, S., Zhu, H., & Xiao, J. (2014). A Mutual Information-Based Hybrid Feature Selection Method for Software Cost Estimation Using Feature Clustering. *2014 IEEE 38th Annual Computer Software and Applications Conference*, 27–32. doi:10.1109/COMPSAC.2014.99

Liu, X., Tang, J., & Member, S. (2014). Mass Classification in Mammograms Using Selected Geometry and Texture Features , and a New SVM-Based Feature Selection Method. *Ieee Systems Journal*, *8*(3), 910–920. doi:10.1109/JSYST.2013.2286539

Liu, Y., Guo, J., & Lee, J. (2011). Halftone Image Classification Using LMS Algorithm and Naive Bayes. *IEEE Transactions on Image Processing*, *20*(10), 2837–2847. doi:10.1109/TIP.2011.2136354

Liu, Y., & Li, Y. (1997). New Approaches of Multifractal Image Analysis. In *International Conference on Information, Communication and Signal Processing* (pp. 9–12).

Lopes, R., & Betrouni, N. (2009). Fractal and multifractal analysis : A review. *Medical Image Analysis*, *13*(4), 634–649. doi:10.1016/j.media.2009.05.003

Lopes, R., Makni, N., Viard, R., Steinling, M., Maouche, S., & Betrouni, N. (2008). 3D multifractal analysis: Application for epilepsy detection in spect imaging. *2008 5th IEEE International Symposium on Biomedical Imaging: From Nano to Macro*, 1199–1202. doi:10.1109/ISBI.2008.4541217

Lyon, D. (2008). Contributions of Wavelet Leaders and Bootstrap to Multifractal Analysis : Images , Estimation Performance , Dependence Structure and Vanishing Moments . Confidence Intervals and Hypothesis Tests . University of Lyon.

MacGillivray, T. J., & Patton, N. (2006). A reliability study of fractal analysis of the skeletonised vascular network using the box-counting technique. *Annual International Conference of the IEEE Engineering in Medicine and Biology - Proceedings*, (c), 4445–4448. doi:10.1109/IEMBS.2006.260821

Mandelbrot, B. B. (1967). How Long Is the Coast of Britain? Statistical Self-Similarity and Fractal Dimension, *Science, 156*(3775), 636–638.

Mandelbrot, B. B. (1977). *The Fractal Geometry of Nature*. New York: W.H. Freeman.

Mandelbrot, B. B. (2006). Self-Affine Fractals and Fractal Dimension. *Physica Scripta*, *32*(4), 257–260. doi:10.1088/0031-8949/32/4/001

Mangai, J. A., Nayak, J., & Kumar, V. S. (2013). A Novel Approach for Classifying Medical Images Using Data Mining Techniques. *International Journal of Computer Science and Electronics Engineering(IJCSEE)*, *1*(2). doi:http://10.1109/TKDE.2008.234

Marsland, S. (2014). Machine Learning: An Algorithm Perspective. (2nded.). USA: CRC Press.

Martinez, F. S. J., Martin, M. A., Caniego, F. J., Tuller, M., Guber, A., & Pachepsky, Y. (1999). Multi fractal analysis of discretized X-ray CT images for the characterization of soil macropore structures.*Geoderma, 156*(2), 32-42.

Martín-Landrove, M., Pereira, D., Caldeira, M. E., Itriago, S., & Juliac, M. (2007). Fractal analysis of tumoral lesions in brain. *Conference Proceedings : ... Annual International Conference of the IEEE Engineering in Medicine and Biology Society. IEEE Engineering in Medicine and Biology Society. Conference*, *2007*(2), 1306–9. doi:10.1109/IEMBS.2007.4352537

Masashi, T., Fukuoka, J., Nitta, N., Takazakura, R., Nagatani, Y., Murakami, Y., … Murata, K. (2008). Imaging of pulmonary emphysema: a pictorial review. *International Journal of Chronic Obstructive Pulmonary Disease*, *3*(2), 193–204.

Matsubara, T., Fujita, H., Kasai, S., Goto, M., Yoshinobu T., Hara, T.,Endo, T.,(1997). Development of New Schemes for Detection and Analysis of Mammographic Masses. *IEEE Journal of Biomedical and Health Informatics*, 63–66.

Mendoza, C. S., Washko, G. R., Ross, J. C., Diaz, A. A., Lynch, D. A., & Crapo, J. D. (2012). Emphysema Quantification in A Multi-Scanner HRCT Cohort using Local Intensity Distributions. *IEEE International Symposium on Biomedical Imaging*, 474–477.

Mendoza, F., Verboven, P., Tri, Q., Kerckhofs, G., Wevers, M., & Nicolaï, B. (2010). Multifractal properties of pore-size distribution in apple tissue using X-ray imaging. *Journal of Food Engineering*, *99*(2), 206–215. doi:10.1016/j.jfoodeng.2010.02.021

Mikolajczyk, K., & Schmid, C. (2005). Performance evaluation of local descriptors. *IEEE Transactions on Pattern Analysis and Machine Intelligence*, *27*(10), 1615–30. doi:10.1109/TPAMI.2005.188

Miranda, J. G. V, Montero, E., Alves, M. C., González, A. P., & Vázquez, E. V. (2006). Multifractal characterization of saprolite particle-size distributions after topsoil removal. *Elsevier*, *134*, 373–385. doi:10.1016/j.geoderma.2006.03.014

Miranda, C. R., Soares, F., Sousa, I., F., J., & M., F. (2011). Multifractal Analysis of Blood Oxygen Level Dependent Functional Magnetic Resonance Imaging, 270–275.

Mitra, V., Wang, C. J., & Banerjee, S. (2006). Lidar detection of underwater objects using a neuro-SVM-based architecture. *IEEE Transactions on Neural Networks*, *17*(3), 717–731. doi:10.1109/TNN.2006.873279

Mukundan, R., & Hemsley, A. (2010). Tissue Image Classification Using Multifractal Spectra. *International Journal of Multimedia Data Engineering and Management*, *1*(2), 62–75. doi:10.4018/978-1-4666-1791-9.ch006

Nanni, L., Brahnam, S., & Lumini, A. (2011). Combining different local binary pattern variants to boost performance. *Expert Systems with Applications*, *38*(5), 6209–6216. doi:10.1016/j.eswa.2010.11.048

Nanni, L., Lumini, A., & Brahnam, S. (2012). Expert Systems with Applications Survey on LBP based texture descriptors for image classification. *Expert Systems With Applications*, *39*(3), 3634–3641. doi:10.1016/j.eswa.2011.09.054

Nava, R., Marcos, J. V., Escalante-ram, B., Crist, G., & Perrinet, L. U. (2013). Advances in Texture Analysis for Emphysema Classification. *Springer-Verlag Berlin Heidelberg*, 214–221.

Nava, R., Escalante-Ramírez, B., Cristóbal, G., & Estépar, R. S. J. (2014). Extended Gabor approach applied to classification of emphysematous patterns in computed tomography. Medical & Biological Engineering & Computing, 52(4), 393–403. http://doi.org/10.1007/s11517-014-1139-9

Nilsson, E. (2007). Multifractal-based Image Analysis with applications in Medical Imaging. Department of Computer Science, Umea University, Umea Sweden.

Oiwa, N., & Fiedler-Ferrara, N. (1998). Physical D. *Elsevier*, *124*, 210–224.

Ojala, T., Pietikäinen, M., & Mäenpää, T. (2000). Gray Scale and Rotation Invariant Texture Classification with Local Binary Patterns. *In Practice*, *1842*, 404–420.

Ojala, T., Pietikäinen, M., & Mäenpää, T. (2002). Multiresolution gray-scale and rotation invariant texture classification with local binary patterns. *PAMI*, *24*(7), 971–987.

Oudjemia, S., Girault, J., Derguini, N., & Haddab, S. (2013). Multifractal Analysis: Application to Medical Imaging., 244–249.

Oudjemia, S., Girault, J., Haddab, S., Ouahabi, A., & Ameur, Z. (2012). Multifractal analysis based on discrete wavelet for texture classification : application to medical magnetic resonance imaging. *Image Processing Theory, Tools and Applications*, 1–4.

Papadopoulos, A., Plissiti, M., & Fotiadis, D. (2005). Medical-image processing and analysis for CAD systems. *Journal of Applied Signal Processing*, *2*(5), 25–41.

Paramanathan, P., & Uthayakumar, R. (2008). An algorithm for computing the fractal dimension of waveforms. *Applied Mathematics and Computation*, *195*(2), 598–603. doi:10.1016/j.amc.2007.05.011

Paskaš, M. P., Reljin, I. S., & Reljin, B. D. (2014). Multifractal Framework Based on Blanket Method. *The Scientific World Journal*, 1–13.

Patton N., Aslam T., MacGillivray T. Pattie A., Deary I.J., & Dillon B. (2005). Retinal vascular as a potential screening tool for cerebrovascular disease: A rationale based on homology between cerebral and retinal. *Journal of Anatomy,* 206(4), 319-348.

Pei, X. (2015). Emphysema classification using convolutional neural networks. *Intnl. Conf. on Intell. Robotics and Applications (ICIRA)*, 455-461.

Pentland, A. P. (1984). Fractal-Based Description of Natural Scenes. *IEEE Transactions on Pattern Analysis and Machine Intelligence*, *PAMI-6*(6), 661–674. doi:10.1109/TPAMI.1984.4767591

Perrier, E., Tarquis, A. M., & Dathe, A. (2006). A program for fractal and multifractal analysis of two-dimensional binary images : Computer algorithms versus mathematical theory. *Elsevier*, *134*, 284–294. doi:10.1016/j.geoderma.2006.03.023

Polychronaki, G., Ktonas, P.Y., Gatzonis, S., Satouni, A., Asvestas, P.A., Tsekou, H., Sakas, D., Nikita, K.S. (2010). Comparison of fractal dimension estimation algorithms for epileptic seizure onset detection. *Journal of neural engineering,* 4(7), 1-18, *10.1088/1741-2560/7/4/046007*

Portilla, J., & Simoncelli, E. P. (2000). Parametric texture model based on joint statistics of complex wavelet coefficients. *International Journal of Computer Vision*, *40*(1), 49–71. doi:10.1023/A:1026553619983

Porto, M.A., & d'Ornellas, M. (2015). Automated Image Retrieval of Chest CT Images Based on Local Grey Scale Invariant Features. *Studies in Helath Technology and Informatics*.

Posadas, A. N. D., Giménez, D., Quiroz, R., & Protz, R. (2003). Multifractal Characterization Of Soil Pore Systems. *Journal of Food Engineering*, *67*, 1–14.

Premebida, C., Ludwig, O., Silva, M., & Nunes, U. (2010). A Cascade Classifier applied in Pedestrian Detection using Laser and Image-based Features. *Annual Conference on Intelligent Transportation System*, 1153–1159.

Priya, E., Srinivasan, S., & Ramakrishnan, S. (2011). Differentiation of digital tb images using multifractal analysis. *IEEE CCECE*, 1431–1434.

Pu, Y., Jin, W., Zhu, M., & Hu, L. (2006). Classification of Radar Emitter Signals Using Cascade Feature Extractions and Hierarchical Decision Technique. *International Journal of Signal Processing*, (2), 1–4.

Radiopaedia (2016): A Wiki-based Collaborative Radiology Resource, https://radiopaedia.org, accessed 30/10/2016.

Ramalhoa, G.L.B., Ferreiraa, D. S., Filhoa, P. R., & de Medeiros, F.N.S. (2016). Rotation invariant feature extraction using a structural co-occurrence matrix. *Measurement*, 94, 406-415.

Ramírez-cobo, P., & Vidakovic, B. (2013). A 2D wavelet-based multiscale approach with applications to the analysis of digital mammograms. *Computational Statistics and Data Analysis*, *58*, 71–81. doi:10.1016/j.csda.2011.09.009

Randen, T., & Husoy, J. H. (1999). Filtering for texture classification: a comparative study. *IEEE Transactions on Pattern Analysis and Machine Intelligence*, *21*(4), 291–310.

Rangayyan, R. M., & Nguyen, T. M. (2005). Pattern classification of breast masses via fractal analysis of their contours. *International Congress Series*, *1281*, 1041–1046. doi:10.1016/j.ics.2005.03.329

Reishofer, G., Koschutnig, K., Enzinger, C., Ebner, F., & Ahammer, H. (2012). Fractal Dimension and Vessel Complexity in Patients with Cerebral Arteriovenous Malformations. *PLOS ONE*, *7*(7). doi:10.1371/journal.pone.0041148

Reljin, I. S., & Reljin, B. D. (2002). Fractal geometry and multifractals in analyzing and processing medical data and images. *Archive of Oncology*, *10*(4), 283–293. doi:10.2298/AOO0204283R

Ruiz, V., & Nasuto, S. (2005). Biomedical-image classification methods and techniques. FL.

Sheluhin, O. I., Smolskiy, S. M., & Osin, A. V. (2007). *Self-Similar Processes*. USA: John Wiley & Sons Ltd.

Shrivastava, N., & Tyagi, V. (2013). An effective scheme for image texture classification based on binary local structure pattern. *Springer-Verlag Berlin Heidelberg*, *30*, 1223–1232.

Soares, F., Janela, F., Pereira, M., Seabra, J., & Freire, M. M. (2014). Classification of Breast Masses on Contrast-Enhanced Magnetic Resonance Images Through Log Detrended Fluctuation Cumulant-Based Multifractal Analysis. *IEEE Systems Journal*, *8*(3), 929–938.

Sørensen, L., Shaker, S. & de Bruijne, M. (2008). Dissimilarity representations in lung parenchyma classification. In N. Karssemeijer & M. L. Giger (Eds.), *In Proceeding of the Spie digital library Conference, Medical imaging; Computer-Aided Diagnosis.* (Vol. 7260(27), pp. 1–12). doi:10.1117/12.812505

Sørensen, L., & de Bruijne, M. (2008). Texture classification in lung CT using local binary patterns, *In Proceeding of Medical imae computingg and computer assistedintervention.*

Sorensen, L., Nielsen, M., & Lo, P. (2012). Texture-based analysis of COPD: a data-driven approach. *IEEE Transactions on Medical Imaging*, *31*(1), 70–78.

Sørensen, L., Shaker, S. B., & Bruijne, M. De. (2010). Quantitative Analysis of Pulmonary Emphysema using Local Binary Patterns. *IEEE Transactions on Medical Imaging*, *29*(2), 559–569. doi:10.1109/TMI.2009.2038575

Sorensen, L., Shaker, S. B., & de Bruijne, M. (2010). Computed Tomography Emphysema Database. Retrieved February 9, 2015, from http://image.diku.dk/emphysema_database/

Stern, E., Swensen, S.J., Kanne, J.P. (2010). High Resolution CT of the Chest, Wolters Kluwer.

Stojić, T., Reljin, I., & Reljin, B. (2006). Adaptation of multifractal analysis to segmentation of microcalcifications in digital mammograms. *Physica A: Statistical Mechanics and Its Applications*, *367*, 494–508. doi:S0378437105012331

Stosić, T., & Stosić, B. D. (2006). Multifractal Analysis of Human Retinal Vessels. *IEEE Transactions on Medical Imaging*, *25*(8), 1101–1107.

Strauss, D. J., Teuber, T., Steidl, G., & Corona-strauss, F. I. (2013). Exploiting the Self-Similarity in ERP Images by Nonlocal Means for Single-Trial Denoising. *IEEE Transactions on Neural Systems and Rehabilitation Engineering*, *21*(4), 576–583. doi:10.1109/TNSRE.2012.2220568

Supriyanto, C., Yusof, N., & Nurhadiono, B. (2013). Two-Level Feature Selection for Naive B ayes with Kernel Density Estimation in Que stion Classification based on B loom ' s Cognitive Levels, 1–5.

Tabar, L., Duffy, S. W., & Burhenne, L. W. (1993). New swedish breast cancer detection results for women aged 40–49. *Cancer*, *72*(S4), 1437–1448.

Takahashi, T., Kosaka, H., Murata, T., & Omori, M. (2009). Application of a multifractal analysis to study brain white matter abnormalities of schizophrenia on T2-weighted magnetic resonance imaging. *Psychiatry Research: Neuroimaging*, *171*(3), 177–188. doi:10.1016/j.pscychresns.2008.03.009

Takahashi, T., Murata, T., Omori, M., Kosaka, H., & Takahashi, K. (2004). Quantitative evaluation of age-related white matter microstructural changes on MRI by multifractal analysis. *ELSEVIER*, *225*, 33–37. doi:10.1016/j.jns.2004.06.016

Tankasala, S. P., & Doynov, P. (2015). Multi Scale Multi Directional Shear Operator for Personal Recognition Using Conjunctival Vasculature. Department of Computer Science and Enginnering.

Tay, C. (2012). *Algorithms for Tissue Image Analysis using Multifractal Techniques*. University of Canterbury, Christchurch ,New Zealand.

Tay, C., Mukundan, R., & Racoceanu, D. (2011). Multifractal Analysis of Histopathological Tissue Images. In *IVCNZ* (pp. 80–85). Retrieved from http://hdl.handle.net/10092/6247

Thomazini, D., Gelfuso, M. V, & Altafim, R. A. C. (2008). Analysis of entropy and fractal dimension to classify the hydrophobicity in polymeric insulators. *Electrical Insulating Materials, 2008. (ISEIM 2008). International Symposium on*, (2), 279–282. doi:10.1109/ISEIM.2008.4664551

Tricot, C. (1995). *Curves and Fractal Dimension*. *Springer-Verlag*. New York. doi:10.1007/978-1-4612-4170-6

Varma, M., & Zisserman, A. (2009). A statistical approach to material classification using image patch exemplars. *IEEE Transactions on Pattern Analysis and Machine Intelligence*, *31*(11), 2032–2047. doi:10.1109/TPAMI.2008.182

Vasiljevic, J., Reljin, B., Sopta, J., Mijucic, V., Tulic, G., & Reljin, I. (2012). Application of multifractal analysis on microscopic images in the classification of metastatic bone disease. *Biomedical Microdevices*, *14*, 541–548. doi:22327812

Vehel, J. L. (1996). Fractal Geometry and Analysis. *Fractal World Scientific Publishing*, 1–21.

Vehel, J. L., & Mignot, P. (1994). Multifractal Segmentation of Images, Fractals. *Fractal World Scientific Publishing*, *2*, 371–378. doi:https://hal.inria.fr/inria-00592260

Wang, D., Nie, F., & Huang, H. (2015). Feature Selection via Global Redundancy Minimization, *4347*(c), 1–14. doi:10.1109/TKDE.2015.2426703

Wang, L. (2005). Support Vector Machines : Theory and Applications. Berlin: Springer-Verlag.

Wang, L.-M., Li, X.-L., Cao, C.-H., & Yuan, S.-M. (2006). Combining decision tree and Naive Bayes for classification. *Knowledge-Based Systems*, *19*(7), 511–515.

Webmd emphysema imaging web portal. (2016). Retrieved March 11, 2017, from http://www.webmd.com/lung/copd/emphysema-diagnosis-and-treatments

Wei, J., & Cong, W. (2012). One Statistics-Based Fault Classification Technique F or Cascaded Inverter. *International Power Electronics and Motion Control Conference*, 494–498.

Wlodzimierz, K., Pierzchalski, M., Stepien, P., Stepien, R., Sedivy, R., & Ahammer, H. (2013). Application of Higuchi's fractal dimension in analysis of images of Anal Intraepithelial Neoplasia. *Chaos, Solitons and Fractals*, *48*(1), 54–60. doi:10.1016/j.chaos.2013.01.004

Xu, J. W., & Suzuki, K. (2014). Max-AUC feature selection in computer-aided detection of polyps in CT colonography. *IEEE Journal of Biomedical and Health Informatics*, *18*(2), 585–593. doi:10.1109/JBHI.2013.2278023

Xu, Y., Yang, X., Ling, H., & Ji, H. (2010). A new texture descriptor using multifractal analysis in multi-orientation wavelet pyramid. *Proceedings of the IEEE Computer Society Conference on Computer Vision and Pattern Recognition*, (60603022), 161–168. doi:10.1109/CVPR.2010.5540217

Yang, S., Yin, Z. & Luo, B. (1999). Multiscale image segmentation using fractal and neural network, *Jnl. of Electronics*, 16(4), 299-304.

Yaşar, F., & Akgünlü, F. (2005). Fractal dimension and lacunarity analysis of dental radiographs. *Dentomaxillofacial Radiology*, *34*(5), 261–267. doi:10.1259/dmfr/85149245

Yong Xia, Feng, D. D., & Rongchun Zhao. (2006). Morphology-based multifractal estimation for texture segmentation. *IEEE Transactions on Image Processing*, *15*(3), 614–623. doi:10.1109/TIP.2005.863029

Yu-Kun, H., & Yu, S. N. (2007). Recognition of microcalcifications in digital mammograms based on Markov random field and deterministic fractal modeling. *Annual International Conference of the IEEE Engineering in Medicine and Biology - Proceedings*, *2007*, 3922–3925. doi:10.1109/IEMBS.2007.4353191

Zaia, A., Eleonori, R., Maponi, P., Rossi, R., & Murri, R. (2006). MR imaging and osteoporosis: Fractal lacunarity analysis of trabecular bone. *IEEE Transactions on Information Technology in Biomedicine*, *10*(3), 484–489. doi:10.1109/TITB.2006.872078

Zhang, H. (2009). A Novel Bayes Model: Hidden Naive Bayes. *IEEE Transactions on Knowledge and Data Engineering*, *21*(10), 1361–1371.

Zhang, H., & Su, J. (2008). Naive Bayes for optimal ranking. *Journal of Experimental & Theoretical Artificial Intelligence*, *20*(2), 79–93.

Zhang, L., Member, S., Wang, L., Member, S., & Lin, W. (2012). Information for Collaborative Image Retrieval. *IEEE Transactions on Image Processing*, *21*(8), 3707–3720.

Zhang, L., Wang, L., & Lin, W. (2011). Biased subspace learning for SVM Relevance Feedback in Content-Based Image Retrieval. *ICICS 2011 - 8th International Conference on Information, Communications and Signal Processing*. doi:10.1109/ICICS.2011.6174236

Zhao, G., & Ahonen, T. (2010). Rotation Invariant Image and Video Description with Local Binary Pattern Features. *IEEE Transactions on Image Processing*, *21*(4), 1–13.

Zhao, G., & Matti, P. (2007). Local Binary Patterns with an Application to Facial Expressions. *Pattern Analysis and Machine Intelligence,IEEE Transactions on*, *29*(6), 915–928.

Zhu, X., & Shao, Z. (2011). Using no-parameter statistic features for texture image retrieval. *Sensor Review*, *31*(2), 144–153. doi:10.1108/02602281111110004.

Zhuang, X., & Meng, Q. (2004). Local fuzzy fractal dimension and its application in medical image processing. *Artificial Intelligence in Medicine*, *32*, 29–36. doi:10.1016/j.artmed.2004.01.016

Zook, J. M., & Iftekharuddin, K. M. (2005). Statistical analysis of fractal-based brain tumor detection algorithms. *Magnetic Resonance Imaging*, *23*, 671–678. doi:10.1016/j.mri.2005.04.002

11 APPENDICES

11.1 Computed Tomography Emphysema Database

The images obtained from this database were downloaded from the website at (Sorensen et al., 2010): http://image.diku.dk/emphysema_database/. This website hosts CT Emphysema database that has been previously used for texture-based CT biomarkers of chronic obstructive pulmonary disease (COPD).

11.2 Description of Data

The CT scanning was prepared by the general electric equipment with four detector rows and the following parameters:

In-plane resolution 0.78 x0.78mm
Slice thickness 1.25mm
Tube voltage 140kv
Tube current 200mAs

The slices were reconstructed by using a high-spatial-resolution (bone) algorithm and the information provided below also indicate, which subject each patch and each HRCT slice in the file name comes from in order to allow cross-validation at the subject level.

The figure presented in Figure 11.1 represents the components of the HRCT lung tissue image, which comprises of the lower, middle and bottom parts of the image.

The degree or the quantity of the emphysema patterns can also be represented diagrammatically as presented in Figure 11.2.

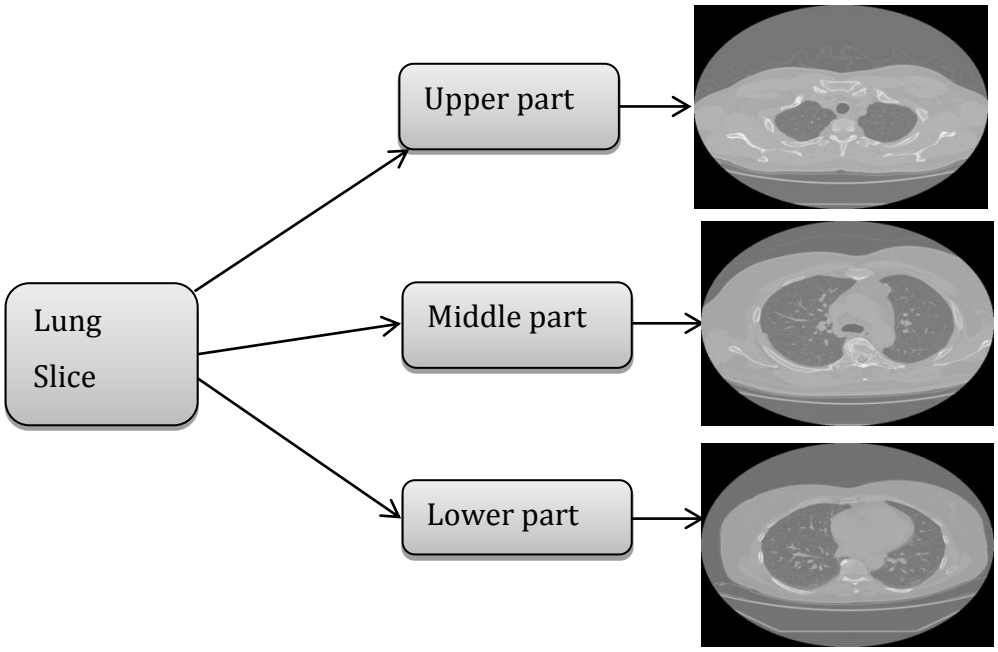

Figure 11-1: Description of lung emphysema slice image

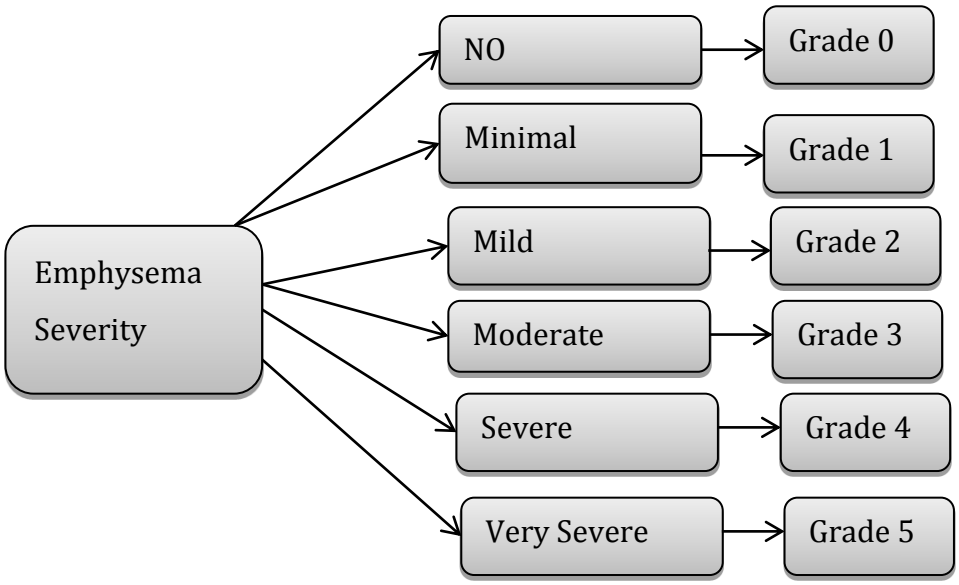

Figure 11-2: Emphysema severity in HRCT slices.

Patch Subject Identifier	Patch Labels	Patch Name -16bits
A0001	1	Patch1.tiff
A0002	1	Patch3.tiff
A0003	1	Patch5.tiff
A0001	1	Patch6.tiff
A0005	1	Patch7.tiff
A0001	1	Patch10.tiff
A0013	2	Patch62.tiff
A0014	2	Patch63.tiff
A0015	2	Patch65.tiff
A0016	2	Patch66.tiff
A0017	2	Patch67.tiff
A0018	2	Patch68.tiff
A0019	2	Patch69.tiff
A0031	3	Patch161.tiff

Table 11-1: Examples illustrating patches data descriptions.

The severity of emphysema is encoded as 0: no Emphysema, 1: minimal, 2: mild, 3: moderate, 4: severe and 5: very severe as pre-labelled by an experienced chest radiologist and a CT experienced pulmonologist through the assessment of the leading patterns. The leading pattern in each HRCT slice image was later used for constructing the patch labels. The details of the patches obtained from the image slice are shown in Table 11.1 and the example of the patches from the database is presented in Figure 11.3.

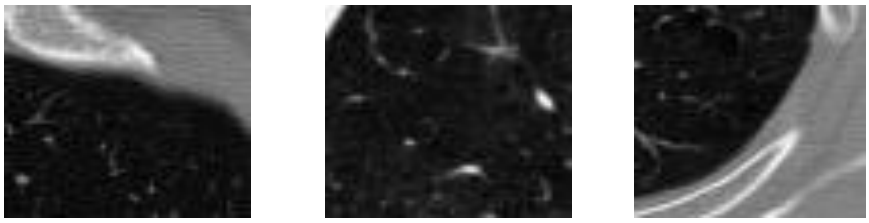

Normal Tissue: 1 Centrilobular: 2 Paraseptal: 3

Figure 11-3: Example of 61x61 pixel patches from the database.

11.3 General Electric Equipment

Figure 11-4: Equipment for CT scanning (Crawford, 2011).

The equipment shown in Figure 11.4 is an example of the general medical system for preparing the CT images using probably some of the parameters listed above and reconstructing the slices by using a high-spatial-resolution (bone) algorithm.